N° d'ordre : 15/22

Thèse de doctorat

Pour obtenir le grade de Docteur de l'Université de

VALENCIENNES ET DU HAINAUT-CAMBRESIS

Et du SHANGHAI INSTITUTE OF CERAMICS

Discipline, spécialité selon la liste des spécialités pour lesquelles l'Ecole Doctorale est accréditée :
Electronique/Microélectronique/Microsystèmes

Présentée et soutenue par Jun GE

Le 15/06/2015, à Villeneuve d'Ascq

Ecole doctorale :
ED 072 Sciences Pour l'Ingénieur (SPI)

Equipe de recherche, Laboratoire :
Institut d'Electronique, de Micro-Electronique et de Nanotechnologie/Département d'Opto-Acousto-Electronique (IEMN/DOAE)

PbZrO3-based antiferroelectric films for energy storage applications

Films anti ferroélectrique à base de PbZrO3 pour le stockage de l'énergie

JURY

Président du jury
- M. T. Lasri, Professeur Université Lille 1, IEMN/MITEC

Rapporteurs
- M. D. Guyomar, Professeur INSA Lyon – LGEF

- M. B. Guiffard, Professeur Université de Nantes, IETR

Examinateurs
- Mme Y. Chen, Professeur SICCAS.

- M. T. Lasri, Professeur Université Lille 1, IEMN/MITEC

Co-directeurs de thèse

- M. G. Wang, Professeur SICCAS

- M. D. Rémiens, Professeur, Université de Valenciennes, IEMN/DOAE.

Membres invités
- M. J. Assaad, Professeur Université de Valenciennes, IEMN/DOAE.

Acknowledgements

First and foremost I want to thank my advisors Prof. Genshui Wang and Prof. Denis Remiens. I have enjoyed the opportunity to study as a joint Ph.D. student between Shanghai Institute of Ceramics and Institute of Electronics, Microelectronic and Nanotechnology (IEMN). I appreciate all their contributions of time, ideas and funding to make my Ph.D. experience productive and stimulating. Thanks very much for Prof. Genshui Wang's frequent insights and patience with me. The joy and enthusiasm Prof. Denis Remiens has for the research was contagious and motivational for me.

I am also thankful for the wise counsel of Prof. Xianlin Dong, who has been steady hands to steer me through my postgraduate career and has provided me an excellent example as a successful group leader.

I want to thank Professor D. Guyomar and Professor Guiffard who have accepted to examine my work. It's a real pleasure to exchange with these specialists.

Particular thanks to Miss Y. Chen for her help during my work. She has always followed my experiments and given to me many ideas. Without her presence the scientific level of my work would have been overshadowed.

I want also to thank Prof. T. Lasri for all the discussions that we had regularly, his participation in the jury of thesis is for me an honor.

I want finally thank Prof. J. Assaad for his participation in the jury. His presence is the testimony of its investment in the quality of the French - China relations.

The members of MIMM team in France have contributed immensely to my personal and professional time at University of Lille 1. The group has been a source of friendships as well as good advice and collaboration. I am especially pleased and grateful for them to work with me: Freddy Ponchel, Jean Costecalde, Yves Sama, Abou Dargham Sara, Areski Ghalem, Sebastien Quignon etc.

I also would like to thank previous and current members in Prof. Xianlin Dong's Group: Xiuyun Lei, Gang Du, Shiguang Yan, Libing Chen, Lingjuan Fei, Kui Li, Junxia Wang, Feng Gao, Tao Li, Zeyong Cai, Jing Zhang, Junwei Wu, Lirong Song, etc for their fruitful supports and friendship.

Financial supports from Chinese Academy of Sciences and Eiffel scholarship are gratefully acknowledged.

Finally, but definitely not the least, great thanks to my family, my father, mother, for their unwavering encouragement and care.

ABSTRACT

With the development of new energy resources, the advanced energy storage technologies are also becoming more and more important. Perovskite lead zirconate $PbZrO_3$ is of great interest for future high-energy and fast-speed storage capacitors, due to the field-forced phase transition into the ferroelectric state accompanied by large charge storage.

The material is deposited on $SrTiO_3$ by RF magnetron sputtering from cold pressed target made in laboratory. The study focuses on the effect of interface between films and electrodes, preferred orientations, epitaxial strain and measuring conditions on the energy storage properties of $PbZrO_3$-based antiferroelectric films. The improvement of interface properties and strain engineering enhance the energy storage density of antiferroelectric film, which may open a route to advance studies on $PbZrO_3$-based antiferroelectric functional devices.

Keywords: $PbZrO_3$, magnetron sputtering, chemical solution depositiion, energy storage, scaling behavior

RESUME

Avec le développement de nouvelles sources d'énergie, les technologies dédiées à son stockage ont un rôle capital. Le zirconate de Plomb (PZ de structure Pérovskite) présente un grand intérêt pour les futures capacités rapides permettant le stockage de forte densité d'énergie. Cette propriété est associée à la transition de phase ferroélectrique – anti ferroélectrique induite par le champ électrique et qui s'accompagne d'une grande capacité de stockage.

Le PZ a été déposé par pulvérisation cathodique RF sur différents types de substrats et notamment le $SrTiO_3$, les cibles sont obtenues par mélange des poudres et pressage à froid. L'étude s'est focalisée sur les effets d'interfaces entre le film et l'électrode inférieure ($LaNiO_3$ dans notre cas), l'orientation préférentielle des films et la réalisation de films épitaxiés de PZ. La structure, la micro structure des films ainsi que leurs épaisseurs ont un impact sur les contraintes existantes dans le film et nous avons évalué ces effets sur la capacité de stockage du PZ dans la phase anti ferroélectrique. L'optimisation des propriétés des interfaces et de l'ingénierie des contraintes permettent d'améliorer la densité d'énergie stockée dans un film anti ferroélectrique. C'est une voie sérieuse pour les supers condensateurs à base de matériaux fonctionnels de type PZ.

Mots clés: $PbZrO_3$, pulverization cathodique, dépôt en solution chimique, stockage de l'énergie, effet d'échelle.

Introduction

CHAPTER 1

Chapter 1 Introduction

With the development and expanded applications of various new energy generation technologies, the devices for effectively storing, absorbing, and supplying electricity are in high demand. Not only high energy storage density, but high-power electric output is also essential for many applications. Although batteries possess high energy storage density, their output power is limited by the slow movement of charge carriers. Electrochemical capacitors have larger power density than batteries, but still not enough to meet demands in some special industrial areas. Dielectric capacitors possess an intrinsic high power density due to their very fast energy uptake and delivery, and thus hold great promise for the generation of high performance power electronics used in hybrid electric vehicles, medical devices, and electrical weapon systems. However, conventional dielectric capacitors only have very small energy density (~10^{-2} to 10^{-1} W·h/kg). If the energy density can be improved to be competitive with electrochemical supercapacitors, the applications of dielectric capacitors in the area of energy management will be greatly extended.

Recently, antiferroelectric (AFE) films are drawing more and more attention for their potential for energy storage applications. For example, the critical field to induce antiferroelectric to ferroelectric phase transition has been enlarged in films compared with the bulk material. Moreover, the dielectric breakdown strength is also enhanced in thin films state. All these can benefit to enhancement of energy storage density of materials. Among all kinds of antiferroelectric films,

$PbZrO_3$-based perovskite compounds are one of the most valuable materials that show great application potential and have drawn great interests around the world. Researchers have investigated the preparation methods, electrodes and multilayers of antiferroelectric films. It is found that the deposition methods have huge influence on the films and they includes chemical solution deposition (CSD), pulsed laser deposition (PLD) and sputtering etc. On the other hand, most of the antiferroelectric films have remnant polarization, which is due to the retained ferroelectric phases in the films. Moreover, with the decreasing of the thickness of films, dielectric constant, maximum polarization and phase transition field tend to decrease, which is not desirable for energy storage applications.

According to the background, this thesis investigated the phase transition and energy storage properties of $PbZrO_3$ based antiferroelectric films. We investigated the influence of strain state on epitaxial and highly-oriented $PbZrO_3$ films and explored new methods to increase the energy storage density of films. We also investigated the effect of different top electrodes on energy storage properties of antiferroelectric films and obtained good top electrode material for energy storage applications. Last, we investigated the scaling behavior of antiferroelectric films with frequency and electric field, which contribute to integrate antiferroelectric films in practical applications.

This thesis is mainly composited by several parts of content as follow:

The effect of residual stress on energy storage property was investigated for a series of $PbZrO_3$ thin films on $SrTiO_3$ and Si substrates. Compressive or tensile

residual stress influences the critical electric field E_A for the ferroelectric-to-antiferroelectric phase transition, thus for films with (110)/(101) orientation, energy density W of films on $SrTiO_3$ is 38% larger than films on Si; in contrast, (001)-oriented $PbZrO_3$ films on $SrTiO_3$ show slightly smaller W compared to films on Si. We conclude that the different responses of W to stress are related to the different constrain states in films with different orientations.

It would be desirable for energy storage applications to have larger phase transition field meanwhile higher saturated polarization value. Using the conclusion we made above, we deposited three kinds of epitaxial films on $SrTiO_3$ substrate with different orientations. We demonstrate an approach to enhance the energy storage density W of antiferroelectric films through simple altering a crystallographic orientation of the substrate. We reveal that the antiferroelectric phase stability of $PbZrO_3$ can be enhanced for the (110) or (111) $SrTiO_3$ substrate orientation, thus suppresses the antiferroelectric-ferroelectric phase transition to higher electric field with ~120 kV/cm increment. In addition, the polarization values of these films are also favorably increased hence increase W by 5.3 J/cm^3 at 700 kV/cm. The observed enhancement is found to originate from a high sensitivity of phase transition to mechanical confinements due to the volume expansion at the transition.

It has been shown experimentally that the reduction of film thickness would result in size effect, which may degrade the energy storage density and the energy efficiency of AFE films severely. Hence polarization switching and energy

storage properties of highly (100) oriented antiferroelectric (Pb,La)(Zr,Ti)O_3 thin films (< 250 nm) deposited via a sol-gel process with both $LaNiO_3$ and Pt top electrodes were investigated. By using $LaNiO_3$ top electrodes, the energy density can be enhanced by 4.6 J/cm^3 and energy efficiency by 11%, respectively，reaches 19.0 J/cm^3 @ 900 kV/cm. Furthermore, the films with $LaNiO_3$ top electrodes are more capable of providing high energy density over a wide temperature regime above room temperature compared to Pt. This work clearly highlights that oxide top electrodes can greatly improve the energy storage performance of antiferroelectric thin film capacitors.

The material devices are often required to operate under conditions of varying frequencies and electric field in practical applications. Therefore, a prior knowledge of how the material properties change under different operating conditions and establishment of their scaling relation is considerably crucial for the selection of a suitable working condition and the design of a proper energy-storage device. Antiferroelectric Pb(Zr, Nb, Ti)O_3 (PZNT) films were deposited via a sol-gel process on Pt(111)/Ti/SiO_2/Si, $LaNiO_3$- and $La_{0.5}Sr_{0.5}CoO_3$-buffered Si substrate. The scaling behavior of the energy density W of antiferroelectric films was investigated. The scaling behavior of W against frequency f of PZNT on $LaNiO_3$-buffered Si takes the form of $W \propto f^{0.08}$, which differs significantly from that form of $W \propto f^{-0.14}$ of PZNT on $La_{0.5}Sr_{0.5}CoO_3$-buffered Si. This indicates that the scaling relations of W vary substantially as bottom electrodes change and

might be closely related to the variation of non-uniform strain field and depolarization field within the AFE films.

Furthermore, we investigated the scaling behavior of dynamic hysteresis with frequency f and electric field E_0 in epitaxial $PbZrO_3$ antiferroelectric film on (111)-oriented $SrTiO_3$ substrate. The scaling relation for the saturated hysteresis loops takes the form of hysteresis area $\langle A \rangle \propto f^{0.03}(E_0-E_{AF})^{0.20}$ at relatively low testing f. However, when the frequency exceeds 30 Hz, the $\langle A \rangle$ shows stronger dependence on f while remains basically unchanged relation with E_0, leading to a form of $\langle A \rangle \propto f^{0.10}(E_0-E_{AF})^{0.20}$. The scaling behavior is modeled as occurring in a viscous medium where several forces, such as viscous and restoring forces, act on the phase transition process.

CHAPTER 2

Backgrounds and Literature Review

Chapter 2 Backgrounds and Literature Review

2.1 Applications of Electroceramic Capacitor

2.1.1 Electric Vehicle Application

An electric vehicle (EV), also referred to as an electric drive vehicle, uses one or more electric motors or traction motors for propulsion. An electric vehicle may be powered through a collector system by electricity from off-vehicle sources, or may be self-contained with a battery or generator to convert fuel to electricity. Because they are more environmental friendly than traditional vehicles, hence are widely accepted as a future vehicle to replace current automobile. The speed and acceleration of cars depend on the power density of the energy storage system and the maximum distance depends on energy density of the system. So the energy storage system is one of the most important component in EV and major parameter to evaluate the quality of EV.

Current commercial EV use batteries to store energy. Although battery has relatively high energy storage density, the power density is quite low, hence the speed of EV has been restricted. To enhance the performance of EV, modification of its energy storage system is necessary. Under such circumstance, researchers propose to replace battery with capacitor. Compared with battery, capacitor have several advantages: 1. Fast charging; 2. Large discharging current; 3. Long life time; 4. Large power density; 5. Environment friendly; 6. Easy to integrate in electric circuit. Moreover, recently the energy density of capacitor increase

dramatically, which make capacitor possible to replace battery as energy storage system in EV.

2.1.2 Various Kinds of Capacitors and their Comparison

Capacitors may be divided into two main parts. One is electrochemical capacitors, which are also named as "supercapacitors or ultracapacitors",[1] have drawn much attention. These capacitors is in a form between traditional capacitors and batteries, they use electrostatic double-layer capacitance or electrochemical pseudocapacitance to store energy without any chemical reactions occur inside the capacitor, which leads to hundreds of thousands of charging-discharging cycles.[2,3] As schematically illustrated in Fig. 2.1,[4] the supercapacitor comprises several basic elements, including a porous separator, a pair of porous electrodes, electrolyte in the porous separator and electrodes, and a pair of current collectors. With an external bias applied between the two electrodes, the electrical charges supplied at the electrodes attract the ions with opposite charges in the electrolyte at the respective electrode interfaces. Because the porous electrodes have very high exposed surface area (up to ~10^3 m^2/g), and thus an extremely high capacitance value, the amounts of the charge and energy stored are dramatically enhanced.[5-8]

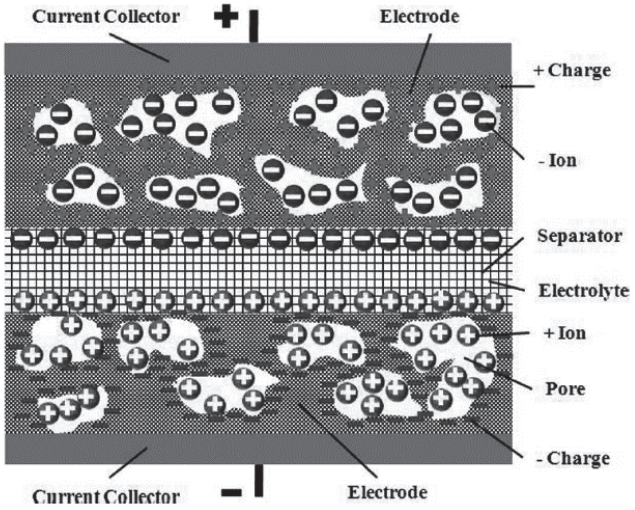

Figure 2.1 A schematic illustration of an electrically charged electrochemical supercapacitor

For a capacitor made of a dielectric material, the electric polarization mechanisms allow more charges to be stored because the dipoles created in the dielectric material under the external bias can bind more charges on the electrodes of the capacitor.[9-11] There are different types of electric polarization mechanisms, including electronic polarization, ionic polarization, dipolar orientation polarization, and space charge polarization.[12] Fig. 2.2 shows that the charges in the orientated electric dipoles under external bias contribute to bind the opposite charges at the respective electrode interfaces. Because the polarization increases with the electric field, a large amount of polarization and thus the charges bound at the electrode can be realized at large voltage. For many nonlinear dielectric materials in which the polarization does not just linearly increase with the electric field, such as ferroelectrics and antiferroelectrics, the polarization and charges can be significantly enhanced with a large electric field. Because dielectric materials

have a large breakdown electric field, dielectric capacitors can work at a high voltage, which can be up to several hundred volts or even higher.[13-16]

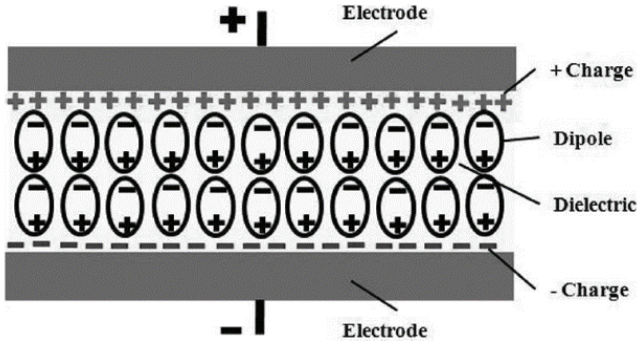

Figure 2.2 A schematic illustration of an electrically charged dielectric capacitor in which the charges of the orientated electric dipoles under bias contribute to bind the opposite charges at the respective electrode interfaces

We can know from above that electrochemical capacitors and dielectric capacitors have different working principles and hence it leads to different characteristics. For better understanding the difference between these two kinds of capacitors, table 2.1 gives the detailed parameter comparison.

Table 2.1 Comparison between electrochemical supercapacitors and dielectric capacitors

electrochemical supercapacitor	dielectric capacitor
liquid state	solid state
big capacitance (~ 1000 F)	small capacitance (< 0.01 F)
low output voltage (< 3 V)	high output voltage (> 300 V)
long discharge time (~ s)	short discharge time (~ μs to ms)
medium power density (10^1 to 10^6 W/Kg)	ultrahigh power density (~10^8 W/Kg)
cycling life (~ 1000 000)	almost unlimited
high leakage current (~ mA)	low leakage current (~ 0.1 mA)
medium energy density (0.04 to 30 W*h/Kg)	energy density (highest ~8 W*h/Kg)

2.1.3 Pulse Power Techniques and Pulse eletroceramic capacitor

Pulse Power Techniques are techniques that discharge stored energy (normally hundreds or thousands of joule) in very short time (~μs to ms), hence allowing a very high power density (~MW). The most important issue is to investigate an energy storage system with high energy density and power density. This technique can be applied to many areas including eletron or ion acceleration, laser, nuclear fusion, electromagnetic pulse etc.

There are many ways to store the energy, for example by capacitor, inductance, machinery and chemical energy etc. Among them, dielectric capacitor has very fast discharging speed (high power density), flexibility, mature technology and low price, hence are becoming one of the most widely spreading technology for energy storage. W. N. Lawless[17] et al. investigated MLCC which shows a theoretical energy density of 6 kJ/L. Moreover, After 105 times of charging and discharging cycles, the capacitor was not broken and the generated heat was also very low.

2.1.4 Antiferroelectric materials and their principle for energy storage

ABO_3 pervoskite oxides have many peculiar properties, such as high temperature superconductor, colossal magnetoresistance and high piezoelectric coefficients, therefore have draw much attention of material researchers. Among those materials, ferroelectric has been investigated for many years.

Ferroelectricity is a property of certain materials that have a spontaneous electric polarization that can be reversed by the application of an external electric

field. In contrast, in antiferroelectric materials, the adjacent dipoles oriented in opposite directions leading to a zero spontaneous polarization. However, the antiparallel dipoles of these compounds can be forced to be parallel by electric fields, corresponding to an electric field-induced AFE-to-ferroelectric (FE) phase transition. These significant changes at the phase transition present opportunities for potential applications such as in energy storage capacitors and displacement transducers.

The potential of antiferroelectric material for energy storage applications can be shown from Fig. 2.3. The energy density of dielectric capacitors can be calculated by following formula:

$$W=\int_{P_r}^{P_{max}} EdD \text{ (upon discharging)} \qquad (2\text{-}1)$$

P_{max} is the maximum polarization, P_r is the remanent polarization.

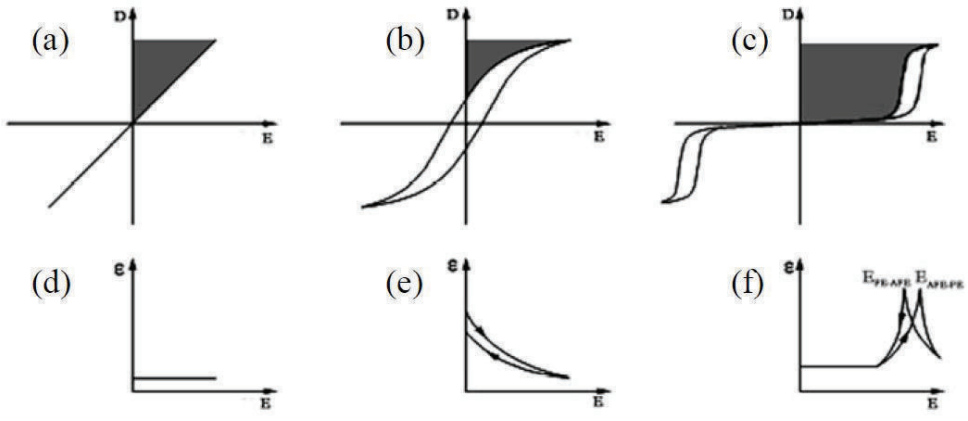

Figure 2.3 Schematic showing electric displacement (~ polarization)-electric field (D-E) (a-c) and dielectric constant-electric field (ε-E) (d-f) curves for three classes of dielectric. The shaded areas are proportional to the theoretic energy density (W). (a), (d) linear dielectric, (b), (e) ferroelectric (FE), (c), (f) antiferroelectric (AFE)

We can see that, the linear dielectric has relatively low energy density (~0.01 J/cm^3) because of the low dielectric constant. The ferroelectric material has much higher permittivity, hence owns relatively high polarization. However, when electric fields excess the coercive field of the material, the permittivity decreases very rapidly with the electric fields. Moreover, because of the hysteresis character of ferroelectric materials, the energy stored in ferroelectric during the charging process can not be fully released. Instead, some of the energy are converted into heat. Fig. 2.3(c) shows a typical antiferroelectric double-hysteresis loop. The shape of the loop can benefit to the energy storage density in two aspects: Firstly, because of the AFE-FE phase transition, AFE film can sustain a high dielectric constant in relatively high electric field and hence absorbing a large amount of energy. On the other hand, film structures can turn back to AFE phase at low electric field and release nearly all the energy (Fig. 2.3(f)).

2.1.5 Antiferroelectric films

Recently, with the development of electronics, information technology and miniaturization of devices, there is a growing interest in film materials.[20,21] Ferroelectric films have various properties including piezoelectric, pyroelectric, ferroelectric and dielectric properties, hence draw extensive attention all over the world. One major kind of ferroelectric film is $Pb(Zr_{0.52}Ti_{0.48})O_3$ (PZT) ferroelectric films.[23,29] Because of the potential applications, investigators also make many work on antiferroelectric films.[30-33] Among them, the fabrication method is an important factor that influences the properties of the film. The

deposition methods include chemical solution deposition (CSD), Pulsed Laser Deposition (PLD), etc. [31,34-36] Fig. 2.4 gives us a modified CSD deposition process. It is worth noting that the pyrolysis temperature and annealing time have large influence on the film properties.

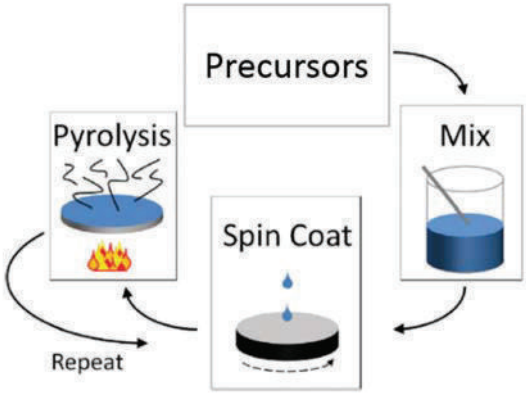

Figure 2.4 A schematic illustration of preparation of antiferro/ferroelectric films by so-gel method

The loss of Pb^{2+} and O^{2-} in ferroelectric material, especially films, is a severe problem that needs to be solve. Hence many researchers investigate the different deposition methods and adjust the parameters to control the property of film. It is shown that PZT95/5 AFE film with a thickness of 2.4 μm can be deposited on RuO_2 coated Fe electrodes by CSD method.[37] Meanwhile, PLD method is also widely used for its accurate control of the composition of the films. Yao et al[38] investigated the influence of O_2 pressure on film properties. They sputtered about 420 nm-thick PLZST film on Pt-coated Si substrates. The pressure of O_2 can determine the orientation of films. At the beginning, the permittivity and maximum polarization increase with the increasing of O_2 pressure, as shown in Fig. 2.5. It is considered to be due to the decreasing of pyrochlore phase with the

increasing of O_2 pressure. However, if the pressure of O_2 excesses a certain value, the roughness of film increases and finally leads to cracks in the films.

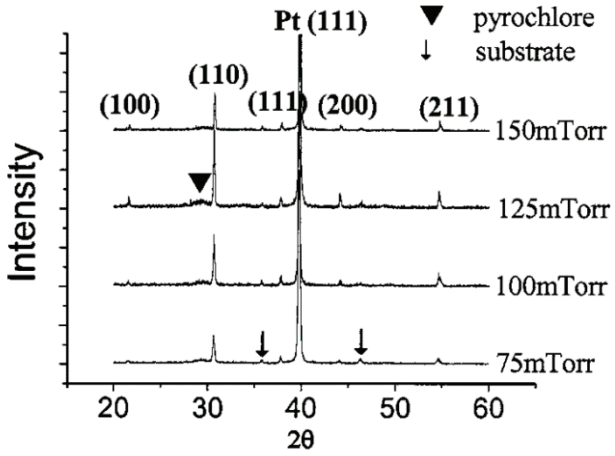

Figure 2.5 XRD patterns of the films deposited under different oxygen pressure from 75 to 150 mTorr

For the choice of materials for electrodes, generally we use Pt, Au and Ag. The main reason is that they are stable in high temperature with low resistance and compatible with integrated circuit. For example, Ill Won Kim et al.[39] deposited La^{3+} doped PZT antiferroelectric films $Pb_{1.075}La_{0.025}(Zr_{0.95}Ti_{0.05})O_3$ on $Pt/Ti/SiO_2/Si$ substrate by PLD method. At Room temperature and 100 kHz, the relatively permittivity is 642 and dielectric loss is 0.021. The Curie temperature is 196 ^oC and it has a typical antiferroelectric double hysteresis loop. The main problem of using metal electrodes is that their structure is very different from the pervoskite structure of many ferroelectrics, hence the ferroelectric film is difficult to grow epitaxially on these electrodes. Moreover, the metal electrode will also bring the problem of fatigue in ferroelectric films. Hence, R.Seveno et al.[40] deposited PZT98/2 antiferroelectric films on LSMO-coated Fe substrate using

CSD method. LSMO has a pervoskite structure like PZT hence on this substrate the deposited film can be as thick as 3.4 μm and saturated polarization is 35 μC/cm^2. Meanwhile, the AFE-FE phase transition behavior can be confirmed by measurement of hysteresis loops, as shown in Fig. 2.6.

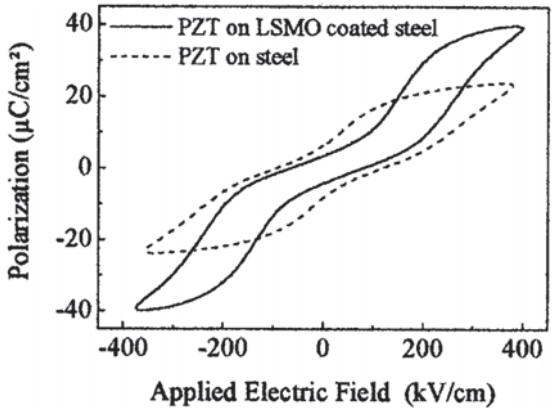

Figure 2.6 Hysteresis loops of PZT 98/2 films of 3 μm on bare and on LSMO-coated steel substrates

For the investigation of energy storage properties, many of AFE films have a remanent polarization because of some retained ferroelectric phase. Xu[41] et al. investigated the PLZST antiferroelectric films and found that, with the decreasing of thickness of film, the dielectric constant, maximum polarization and AFE-FE phase transition field decrease, and a small remanent polarization can be observed in hysteresis loops.

2.1.6 Antiferroelectric films for energy storage application

As mentioned above, compared with other technologies dielectric capacitors have advantages on many aspects such as power density, service life and working temperature. The major drawback is that the energy storage density is still quite

low. Compared with bulk ceramics, dielectric films have much larger energy density.[42,43] There are two main reasons: firstly, the breakdown field of films is much higher than the counterpart of bulk ceramics. In general, the breakdown field of FE/AFE ceramic is several kilovolt per millimeter. In contrast, the breakdown field of films can reach hundreds of kilovolt per millimeter. If we assume the dielectric constant is not changed with the applying electric field, then the formula to calculate the energy density can be rewritten as

$$W=\frac{1}{2}\varepsilon_0\varepsilon_r E^2 \qquad (2\text{-}2)$$

From above we can see that, a square relation is found beween the energy density and electric field applied. Hence increasing of applied electric field can dramatically increase the energy density of the films.

Secondly, the hysteresis loops of films are always “larger” than their counterpart of bulk ceramics. For comparison, the hysteresis loop for a bulk PLZST ceramic as published in the literature is also provided in Fig. 2.7, showing that the switching electric field and the energy density are significantly higher in our thin film sample than in the bulk ceramic.[4,44] It is estimated that the energy density in our PLZST thin film is about 30 times higher than that of the bulk material.

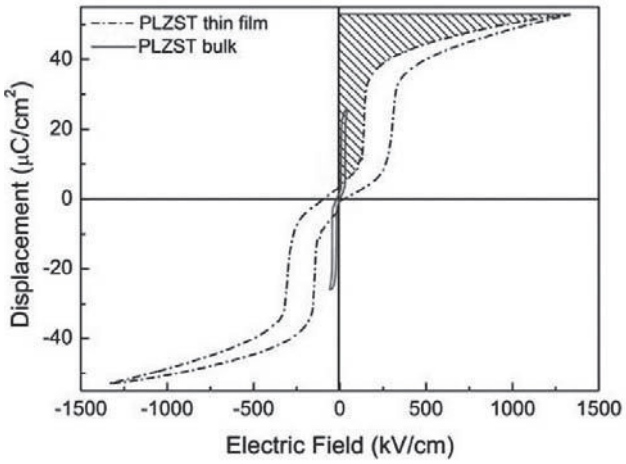

Figure 2.7 The double hysteresis loop of electric displacement-field for a PLZST thin film in comparison with a bulk ceramic. The shaded area represents the energy storage density

Meanwhile, nanostructured devices have the potential to serve as the basis for next-generation energy systems that make use of densely packed interfaces and thin films.[45] Fig. 2.8 points out a kind of nanocapacitor structures that with anodic aluminium oxide (AAO) formation together with multilayer atomic layer deposition (ALD) to form highly controlled, self-aligned nanocapacitors. The nanostructure significantly enhances capacitance density. The nanocapacitors demonstrate the high power (up to 10^6 W/kg) typical of electrostatic capacitors while achieving the much higher energy density (~0.7 Wh/kg) characteristic of electrochemical supercapacitors. As a result, electrostatic nanocapacitors are attractive for high-burst-power applications requiring the energy density of supercapacitors. At this moment, the nanostructure normally choose linear dielectric Al_2O_3. There is still a large space to elevate the energy density by applying FE/AFE material.

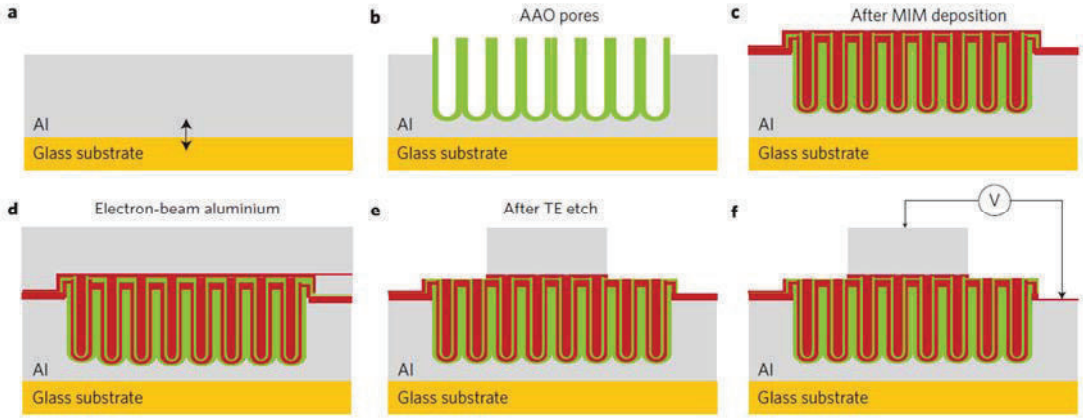

Figure 2.8 Process sequence to prepare MIM capacitors

Another key problem is to obtain ultra-thin, high-quallity dielectric film. The demand for small thickness is to obtain array of capacitors with enough quantity. To further enhance the energy density of the array of nanocapacitors, Park et al deposited about 9 nm-thick $Hf_xZr_{1-x}O_2$ antiferroelectric film on Si substrate with ALD method. The hysteresis loops and energy density with electric field are shown in Fig. 2.9. By adjusting the composition of the film, the energy density can reach to 45 J/cm^3.

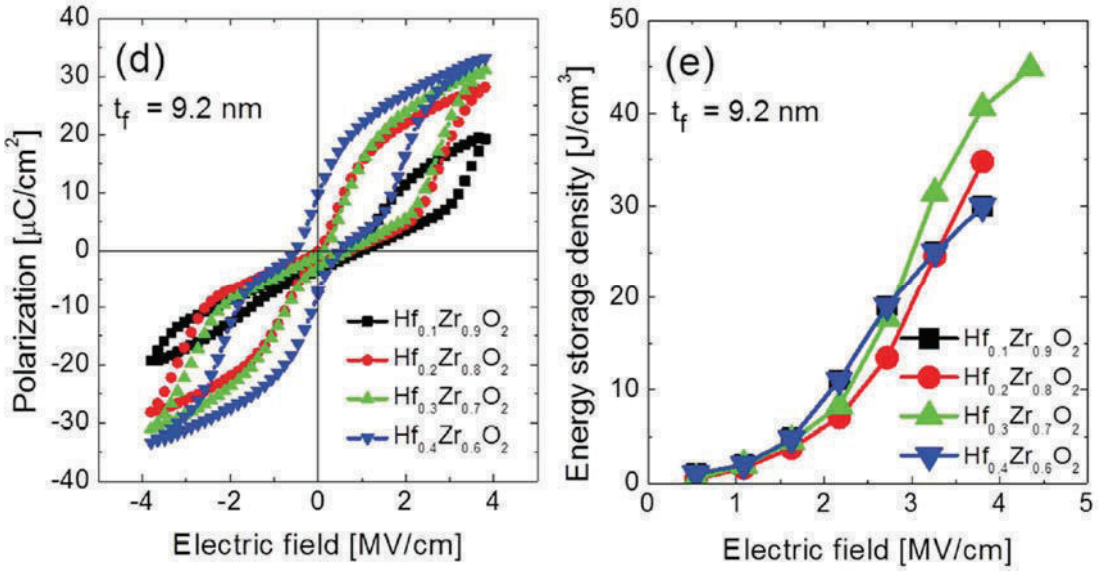

Figure 2.9 *P*-E loops and energy density with electric field of $Hf_xZr_{1-x}O_2$ films

2.2 $PbZrO_3$-based antiferroelectric ceramics and films

Lead zirconate $PbZrO_3$ (PZ) was the first compound identified as an antiferroelectric. In its low-temperature phase ($T<T_c$ ~505 K) $PbZrO_3$ crystallizes in an orthorhombic symmetry allowing 60°, 90° and 180° domains to satisfy the AFE character and the head-to-tail arrangement of the polarization. The unit cell contains eight formula units (Fig. 2.10(a)) and is derived from the single-perovskite cubic structure (a_c =4.16 Å), as the unit-cell parameters (Fig. 2.10(c)) are $a=\sqrt{2}a_c$=5.89 Å, $b=2\sqrt{2}a_c$=11.76 Å，$c=2a_c$=8.22 Å.[47] The orthorhombic phase of $PbZrO_3$ is strongly antiferroelectric in the plane perpendicular to the c-axis.

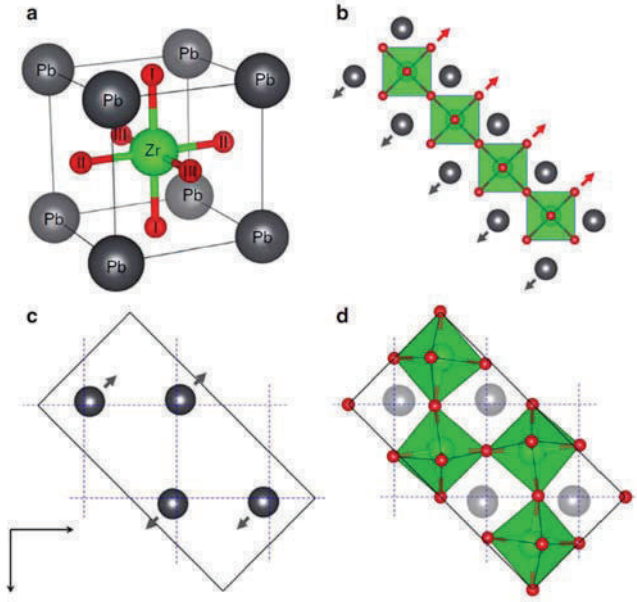

Figure 2.9 (a) Unit cell of lead zirconate in the cubic phase, (b) The Γ-point polar mode, (c) Lead displacements mode, (d) Oxygen-octahedron rotations in the R mode

2.2.1 Investigation of composition of PbZrO3-based antiferroelectric material

To fulfill the demand properties of practical application, dielectric capacitors should have relatively high energy storage density, long service life and good

performance with temperature and frequency.[20,43] In details, we can give some aspects that should attract attention by the analysis the hysteresis loops of AFE: firstly, the material should be in AFE phase in a broad temperature range and can be turn into FE phase by electric field. Secondly, with the decreasing of electric field, the induced FE phase can turn back to AFE phase. Thirdly, the threshold field to induce FE phase E_{AFE-FE} is better to be higher to increase the energy density. Fourthly, the difference between AFE-FE and FE-AFE phase transition field should be small to decrease the energy loss.

Derived from such consideration above, investigators modified the composition of AFE compounds on the base of $PbZrO_3$, including PZ, PLZT, PZST ceramics and films.[53-57] It is reported that the MLCC, made of $Pb_{0.91}La_{0.06}ZrO_3$ ceramics, has a energy density of nearly 12 J/cm^3 at 50 kV/mm. J. Parui et al. deposited La^{3+} modified PZ antiferroelectric film using CSD method, as shown in Fig. 2.10. From the map we can see that, when the concentration of dopant of La^{3+} reaches 5%, the intensity of peak of $(202)_O$ is the highest and the energy density of the film is also the largest of 14.9 J/cm^3.

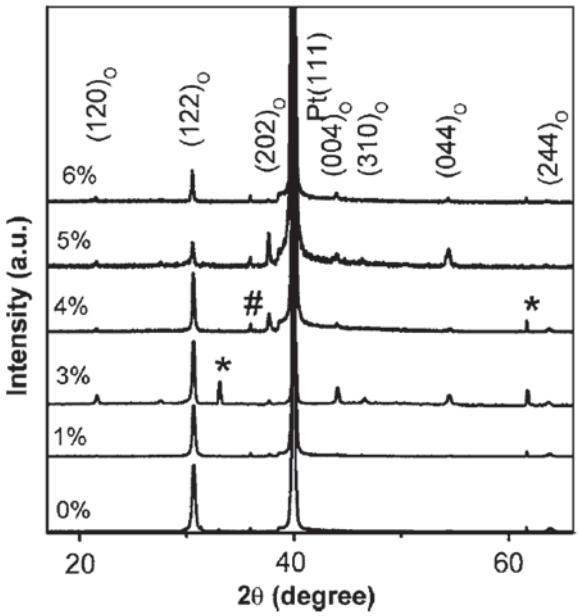

Figure 2.10 XRD pattern of sol-gel derived La-modified PZ thin films with La contents between 0 and 6 at.%

B. H. Ma et al. prepared $(Pb_{0.97}La_{0.08})(Zr_{0.95}Ti_{0.05)}O_3$ antiferroelectric film with a buffer layer by CSD method. The energy density of the film can reach 53 J/cm^3 at 350 kV/mm. The hysteresis loop is shown in Fig. 2.11.

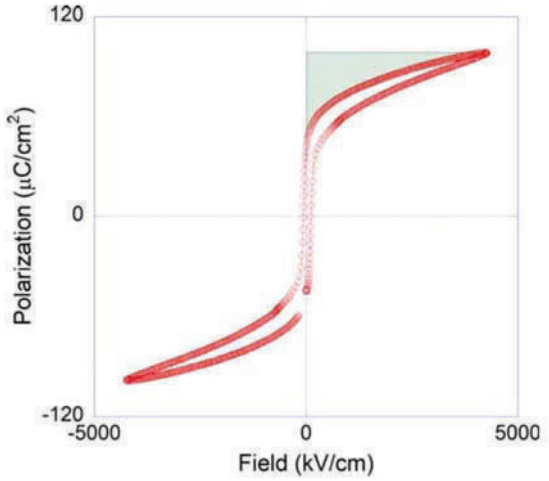

Figure 2.11 *P-E* hysteresis loops of PLZT/LNO/HC measured with high applied field

It is known that $PbZrO_3$ are easier to lose Pb than PZT with higher Ti content, hence one should be more careful to the Pb void in AFE films. M. S. Mirshekarloo et al. deposited $(Pb_{0.97}La_{0.02})(Zr_{0.90}Ti_{0.05}Sn_{0.05})O_3$ on Si substrate using CSD method. With the assistance of PEG stabilizer and PbO coating layer, the film is much more compact, as shown in Fig. 2.12. Therefore, at 150 kV/mm, the energy density of film can be as high as 13.7 J/cm^3.

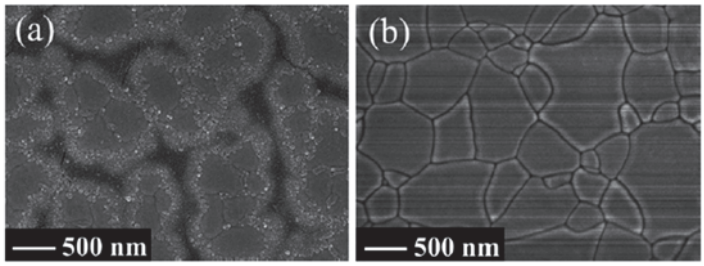

Figure 2.12 FESEM micrographs of PLZST 90/05/05 film annealed at 700 °C without (a) and with (b) PbO capping layer

2.2.2 Effect of strain on $PbZrO_3$-based antiferroelectric material

The energy storage properties of AFE have close relations with the phase transition behavior of AFE material. In another word, the higher of phase transition field we apply, the higher of energy density we can obtain. Hence, investigation in phase transition properties of antiferroelectric have an important meaning. At present, there are quite a lot of works on effect of strain on $PbZrO_3$-based AFE ceramics.[60] Tan et al. studied the effect under mechanical confinements in bulk samples of an antiferroelectric perovskite oxide at room temperature.[61] Profound impacts of mechanical confinements on the phase transition are observed due to the interplay of ferroelasticity and the volume

expansion at the transition. The uniaxial compressive prestress delays while the radial compressive prestress suppresses it.

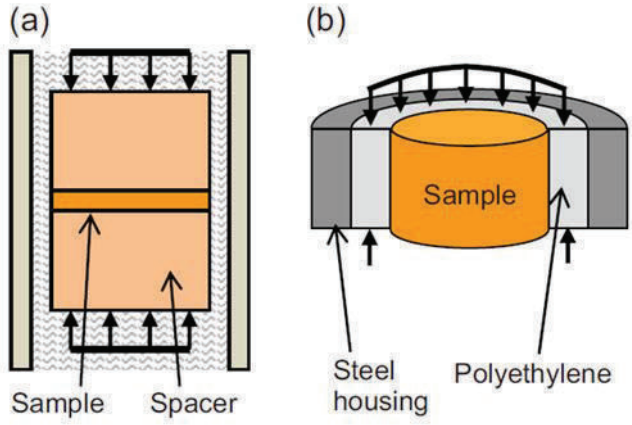

Figure 2.13 Schematic of the loading fixtures for compressive prestresses

On the bases of the work above, Tan et al. continue to study the state of strain in AFE ceramics without any prestress on them.[62] It has been widely accepted that electric fields favor the ferroelectric phase with parallel electric dipoles over the antiferroelectric phase. With detailed measurements in polycrystalline ceramics of PZST, it is demonstrated that electric fields can induce an antiferroelectric phase out of a ferroelectric phase, i.e., trigger an apparently unlikely ferroelectric-to-antiferroelectric phase transition.

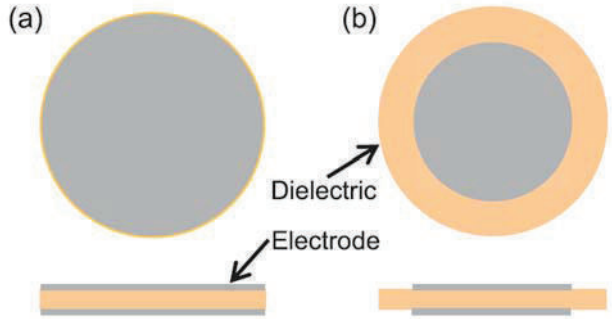

Figure 2.14 Schematic diagram of an antiferroelectric dielectric (a) with full electrodes and (b) with half-area electrode

Young et al. invent a method to increase the energy storage of AFE ceramics by strain engineering.[63] The mechanical self-confinement is realized through partially electroding the antiferroelectric dielectric in the parallel plate capacitor, as schematically shown in Fig. 2.14. During the charging of the capacitor, only the central portion of the dielectric beneath the electrode undergoes the antiferroelectric-to-ferroelectric phase transition. The volume expansion accompanying the transition triggers the unelectroded ring to apply compressive stresses to the central portion of the disk; hence, the antiferroelectric ceramic is mechanically self-confined. Under the applied electric field of 70 kV/cm, a maximum energy density of 1.3 J/cm^3 is achieved. The mechanical self-confinement was introduced by partially electroding the central portion of the dielectric ceramic disk. A phase-field model was developed and it confirms the presence of compressive stresses ~30MPa in the electroded portion of the dielectric disk and the contribution to the increased energy density from the mechanical confinement.

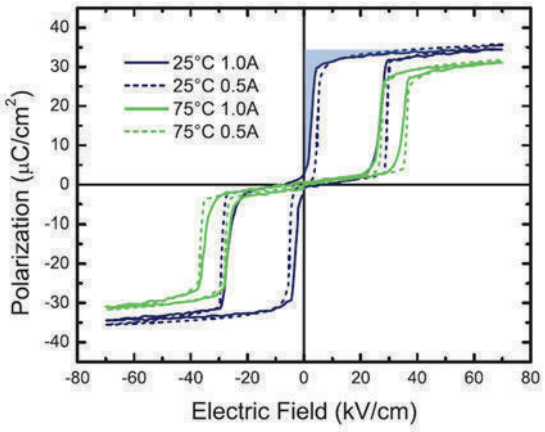

Figure 2.15 Comparison of hysteresis loops of samples with full electrodes and half-area electrodes at different temperatures

There are also many studies on effect of strain on AFE films.[64-69] The pioneered work are made by Xu et al. They deposited PLZST and PNZST AFE films on Si substrates and studied the effect of thermal stress on the shape of hysteresis loops. They found films with high tin content are shown to undergo a diffuse antiferroelectric–paraelectric phase transition with temperature, probably because of compositional inhomogeneity associated with the high tin content. This type of films also demonstrates a diffuse field-induced antiferroelectric–ferroelectric phase switching under high electric field with the appearance of "slim loop" double hysteresis, which can be attributed to the compositional heterogeneity and the high level of tensile stress in the film because of the thermal mismatch between the film and substrate.

Recently, Chaudhuri et al. studied epitaxial $PbZrO_3$ films on $SrTiO_3$ substrates.[72] $PbZrO_3/SrRuO_3/SrTiO_3$ (100) epitaxial heterostructures with different thickness of the $PbZrO_3$ (d_{PZ} ~5–160 nm) were fabricated by pulsed laser deposition. The ultrathin PZ films (d_{PZ} <10 nm) were found to possess a rhombohedral structure. On increasing the PZ film thickness, a bulk like orthorhombic phase started forming in the film with d_{PZ} ~22 nm and became abundant in the thicker films. Nano beam electron diffraction and room-temperature micro-Raman measurements revealed that the stabilization of the rhombohedral phase of PZ could be attributed to the epitaxial strain accommodated by the heterostructures. The change of stress with thickness of film is depicted in Fig. 2.16.

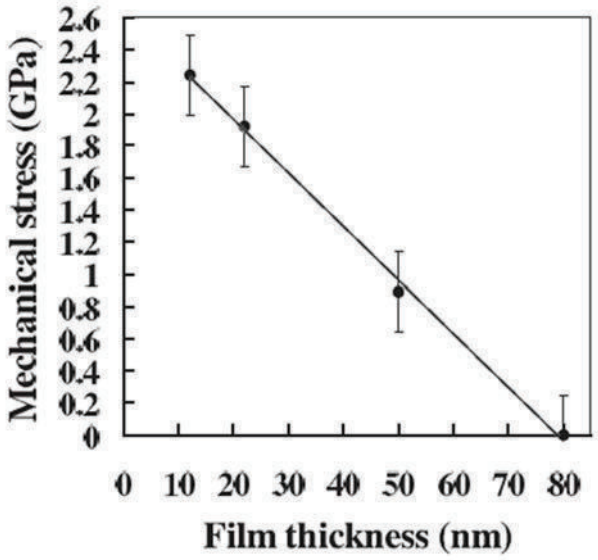

Figure 2.16 Plot of the mechanical stress values vs $PbZrO_3$ film thickness

The polarization versus electric field measurements performed on different samples showed characteristic double hysteresis loops of antiferroelectric materials accompanied by a small remanent polarization for the thick PZ films (d_{PZ} >50 nm). The remanent polarization increased by reducing the PZ layer thickness, and a ferroelectric like hysteresis loop was observed for the sample with d_{PZ} ~22 nm, as shown in Fig. 2.17.

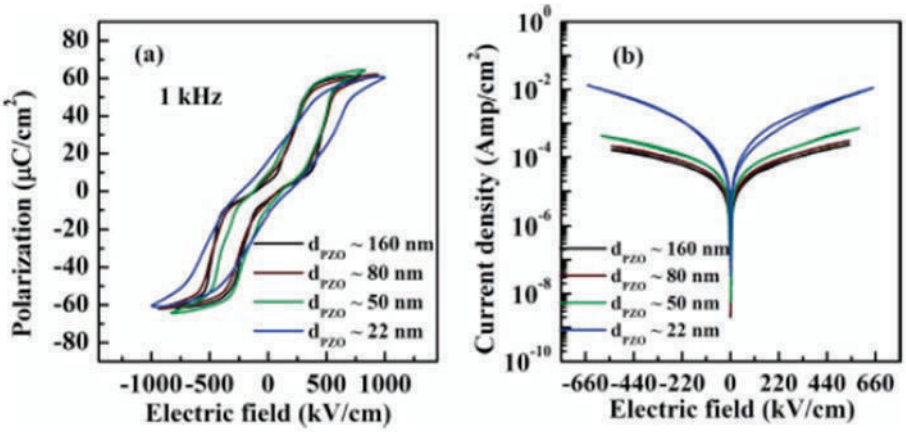

Figure 2.17 P-E hysteresis response and leakage current density of the $PbZrO_3$ thin films as a function of thickness

Besides the strain that comes from the substrate beneath the film, Mirshekarloo et al also studied the effect of strain which is from the top electrode.[73] It is found that the stress and structure of an antiferroelectric PLZST thin film is changed completely by a ferroelastic strain in a magnetic shape memory alloy Ni-Mn-Ga (NMG) thin film on the top of the PLZST, despite the existence of the substrate constraint, as shown in Fig. 2.18. The ferroelastic strain in the NMG film results in AFE to FE phase transformation in the PLZST layer underneath. This finding indicates a different strategy to modulate the structure and function for multilayers thin films and to create unprecedented devices with ferroic thin films.

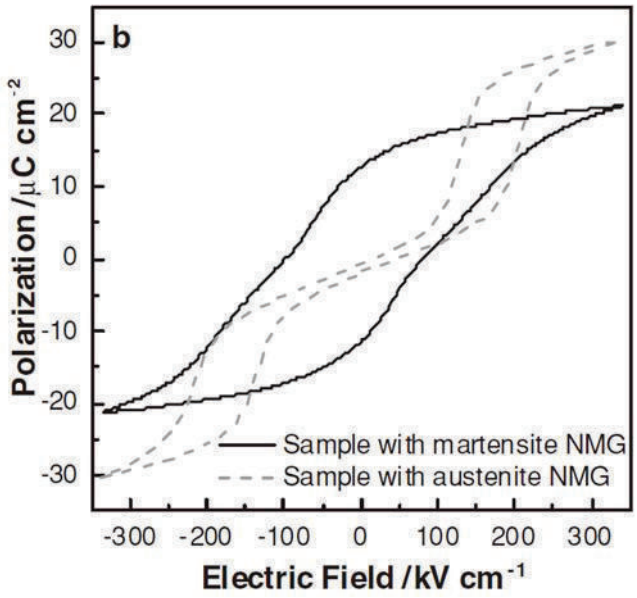

Figure 2.18 Hysteresis loops of the PLZST films with austenite and martensite NMG film on the top, before and after annealing, respectively

2.2.3 Scaling behavior of antiferroelectric material

Antiferroelectric materials are promising candidates of great current interest for future high-energy and fast-speed storage capacitors. Devices in practical applications are often required to operate under conditions of varying frequencies and electric fields, therefore, the scaling behavior of W, i.e., W as a function of the field amplitude E and frequency *f*, has become an important consideration. On the other hand, at present most of the AFE films under study are about 500 nm but in future device films are needed to be much thinner. Hence, studying the variation of film properties with thickness is also very important.

For the scaling behavior of AFE materials with testing frequency and amplitude of electric field, chen et al. investigated the relation of energy density of PNZST ceramics with the frequency and applied electric field.[74] Fig. 2.19 shows the hysteresis loops of PNZST AFE bulk ceramics at various E and f.

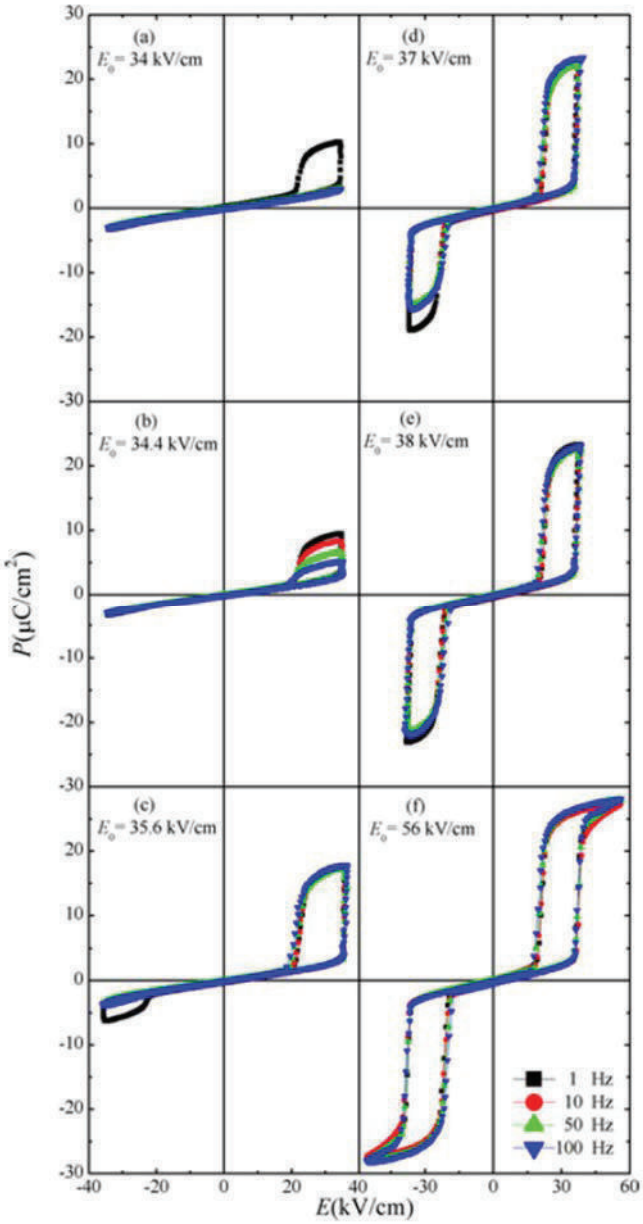

Figure 2.19 Hysteresis loops of PNZST AFE ceramics at various *f* and *E*

They fit these data of double loops with $w \propto f^{\alpha}(E-E_c)^{\beta}$ to obtain the suitable scaling relation for PNZST AFE bulk ceramics. The *f*-term exponent α is obtained by plotting w against $(E-E_c)$ at fixed *f* and the *E*-term exponent β is obtained by plotting w against *f* at fixed *E*, where the threshold field *E* is chosen as E_{AF}. As plotted in Fig. 2.20, it is revealed that these data of double loops can be fitted by

$$w \propto f^{-0.02}(E_0 - 36.8)^{0.08} \qquad (2\text{-}3)$$

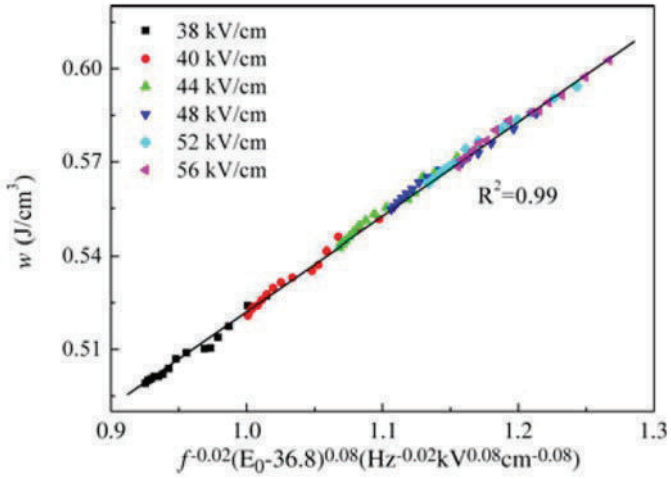

Figure 2.20 Scaling plot of energy densities *w* for double loops of PNZST AFE bulk ceramics

On the other hand, studies on scaling behavior of AFE film with thickness have also gained some results. Firstly, Zhai et al. deposited PNZST AFE film using CSD method on Si substrate and investigated the relation between the electric properties and thickness range from 170 to 920 nm.[75] From Fig. 2.21 we can see that the film with 920 nm-thick has a typical antiferroelectric double hysteresis loop. With the decreasing of thickness, the loop does not change much. It is until the thickness decreases to 285 nm, that the shape of loop start to become relaxed. When the thickness decrease to 170 nm, the double loops is becoming very faint. Besides, with the decreasing of thickness, the curve of dielectric constant with temperature is becoming broader and broader.

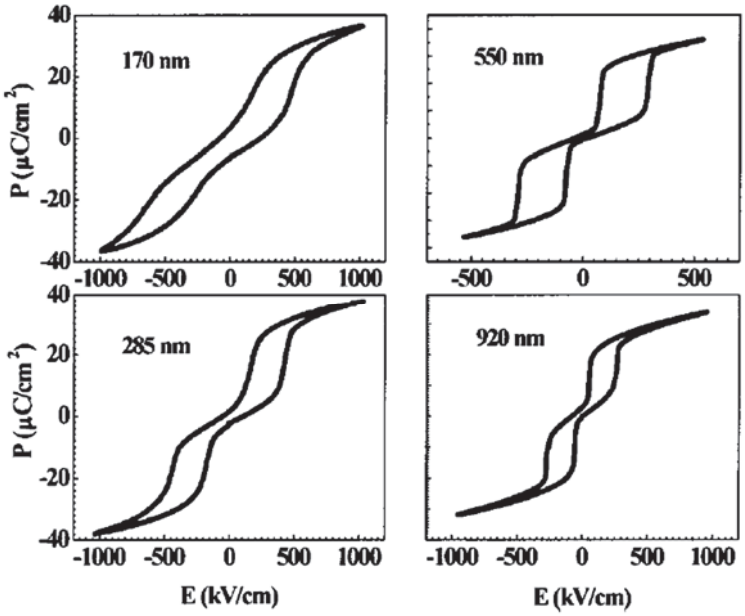

Figure 2.21 the hysteresis loops of PNZST thin film with various values of thickness

Ayyub et al. deposited $PbZrO_3$ films with different thickness on high-resistant Si substrate. They found when the thickness of films decreases to below 400 nm, the hysteresis loop turns to ferroelectric-like loops. They attribute this phenomenon to the high built-in electric field produced at the surface of the semiconducting substrate. However, this explanation can not be applied in other circumstances where highly conductive bottom electrodes are used. Hence, the behavior of deterioration of electric properties with decreasing thickness have not been well explained yet.

2.3 Main purpose and content of this thesis

As we mentioned before, antiferroelectric materials, especially antiferroelectric films, is potential to have a relative high energy density with high power density. $PbZrO_3$ is the first compound that is identified as AFE and the basic material in the area of AFE film. Hence the behavior of $PbZrO_3$ can describe many of the AFE materials. At present, the studies concerning AFE are mainly focused on modification of composition and investigation on effect of strain in AFE materials is quite rare. In addition, the scaling behavior of AFE films has not been reported yet.

In this thesis, to fulfill the demand of high energy density dielectric capacitors, we choose to investigate W of the $PbZrO_3$-based AFE films. We studied the effect of different substrates on electric properties of AFE films and determined the best substrate to increase the energy density of the film. We also investigated the mechanism of phase transition in AFE materials and obtained the relation between phase transition and orientation of films and thickness. Combined with the electric measurements, we could calculate the energy density of the films and inversely guided the experiments we designed to increase the energy density of the films.

CHAPTER 3

Experiment procedures

Chapter 3 Experiment procedures

3.1 Radio-Frequency magnetron sputtering method

Sputtering is a kind of physical vapor deposition technique which generates a glowing discharge and results in a target surface being bombarded by energetic particles such as Ar ions. Magnetron sputtering is another technique which can increase the sputtering rate and operate at lower pressure. In magnetron sputtering, a permanent magnet is installed on the backside of the cathode and generates a magnetic field to trap secondary electrons close to the target during the sputtering process. The electrons follow helical paths around the magnetic field lines and have more ionizing collisions with the neutral gas near the target than would otherwise occur. This enhances ionization of the plasma near the target and leads to a higher sputtering rate.

3.1.1 Preparation of bottom electrode

Single crystal silicon wafers with (100) orientation were cleaned using acetone, isopropanol and deionized water, then dried with a nitrogen gun and loaded into the Addax sputtering chamber. Then we deposit about 150 nm-thick $LaNiO_3$ (LNO) film. The detailed parameter will be mentioned in the following chapters. After the deposition, $LaNiO_3/SiO_2/Si$ heterostructures were then post-annealed at 700 °C for 1 h in a conventional furnace to improve the crystallization and electrical conductivity.

3.1.2 Preparation of PZ films

The PZ films were prepared by RF-magnetron sputtering method. The detailed parameters of deposition are shown in table 3.1.

Table 3.1 Details of the $PbZrO_3$ thin films deposition conditions

Condition	parameter
Vacuum (mbar)	$<3\times10^{-5}$
Pressure of deposition (mbar)	1×10^{-2}
Power density (W/cm^2)	1.52
Gas	Ar
Deposition rate (nm/min)	~1
Composition of target	15% PbO excess of $PbZrO_3$ powders
Temperature (^oC)	RT

After the deposition, the sample was annealed in furnace at 625 ^oC for 30 min, then cooled down in the furnace.

3.2 Chemical Solution Deposition

Using CSD method, it is easy to control the composition of film. In addition, the equipment to perform this deposition is low cost. We applied CSD method to deposit various materials including $La_{0.7}Sr_{0.3}MnO_3$ (LSMO), $Pb(Zr_{0.96}Ti_{0.03})Nb_{0.01}O_3$ (PNZT) and $Pb_{0.97}La_{0.02}(Zr_{0.95}Ti_{0.05})O_3$ (PLZT). The raw materials are listed in table 3.2.

Table 3.2 Main raw materials for the preparation of LNO, PNZT and PLZT thin films

Molecular formula	Standard	Company
CH_3COOH	99.5%	Sinopharm
$CH_3COCH_2COCH_3$	99%	Sinopharm
$Pb(CH_3COO)_2 \cdot 3H_2O$	99%	Sinopharm
$Ti(OCH(CH_3)_2)_4$	97%	Alfa Aesar
$Zr(OCH_2CH_2CH_3)_4$	99%	Alfa Aesar
$La(CH_3COO)_3 \cdot 1.5H_2O$	99.9%	Alfa Aesar
$Ni(CH_3COO)_3 \cdot 4H_2O$	98.5%	Sinopharm
$Nb(OC_2H_5)_5$	99%	Alfa Aesar

3.2.1 Procedure of CSD method

The basic procedure of CSD method I shown in Figure 3.1.

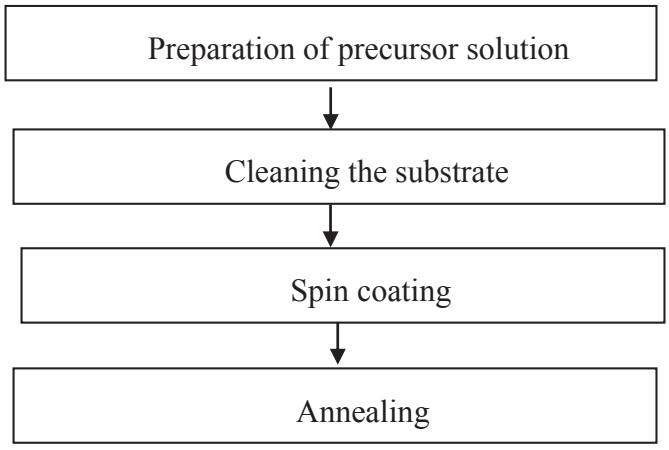

Figure 3.1 Flowing diagram of fabricating thin films by sol-gel method

The details of preparation of LNO, LSMO, PLZT precursor solution are shown Figure 3.2, 3.3 and 3.4.

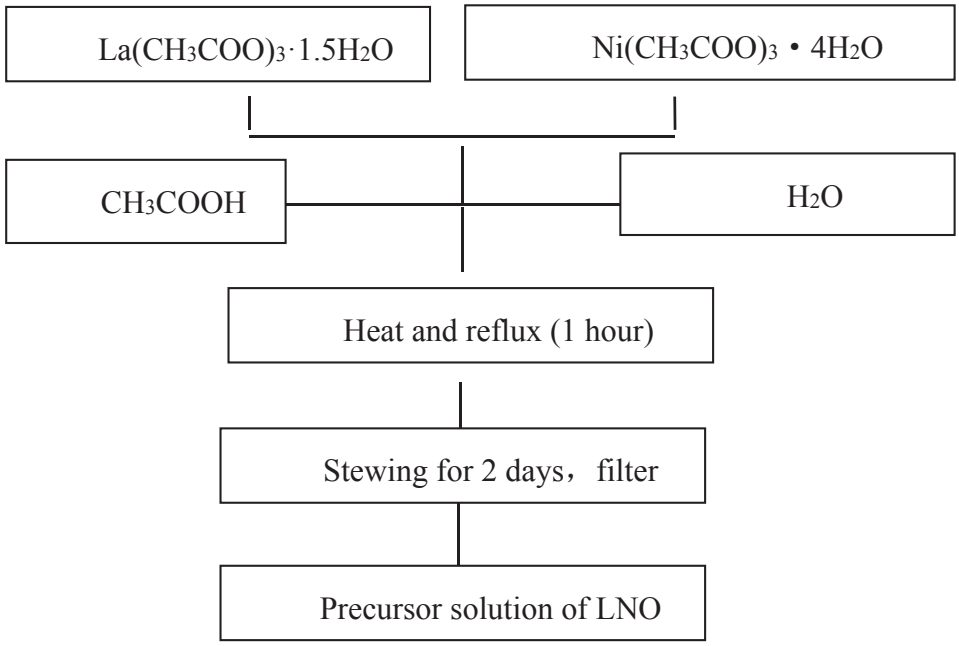

Figure 3.2 Flowing diagram of preparation of LNO precursor solutions

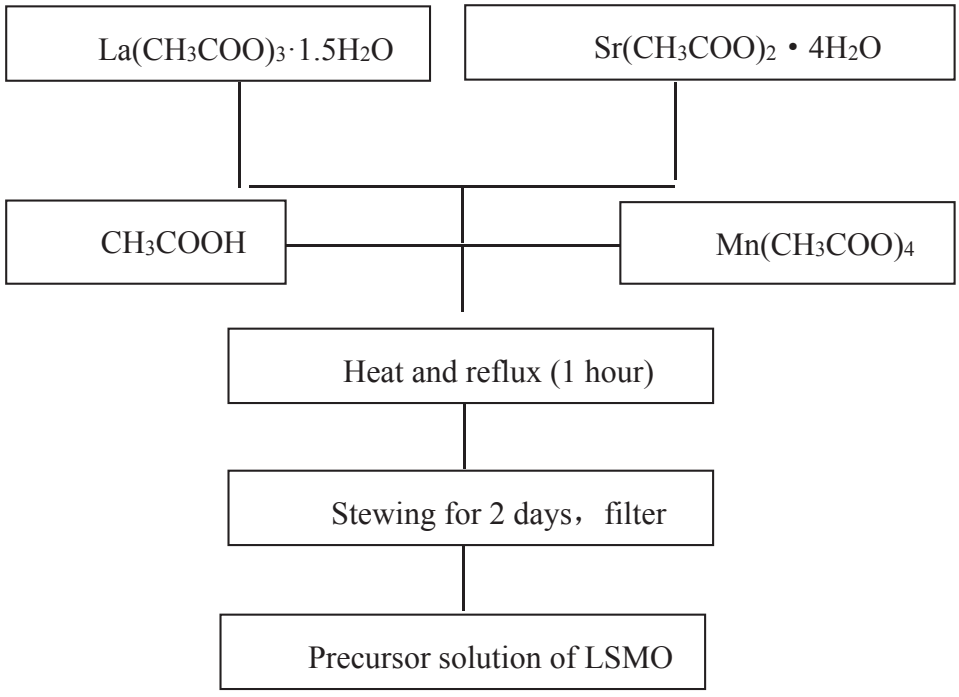

Figure 3.3 Flowing diagram of preparation of LSMO precursor solutions

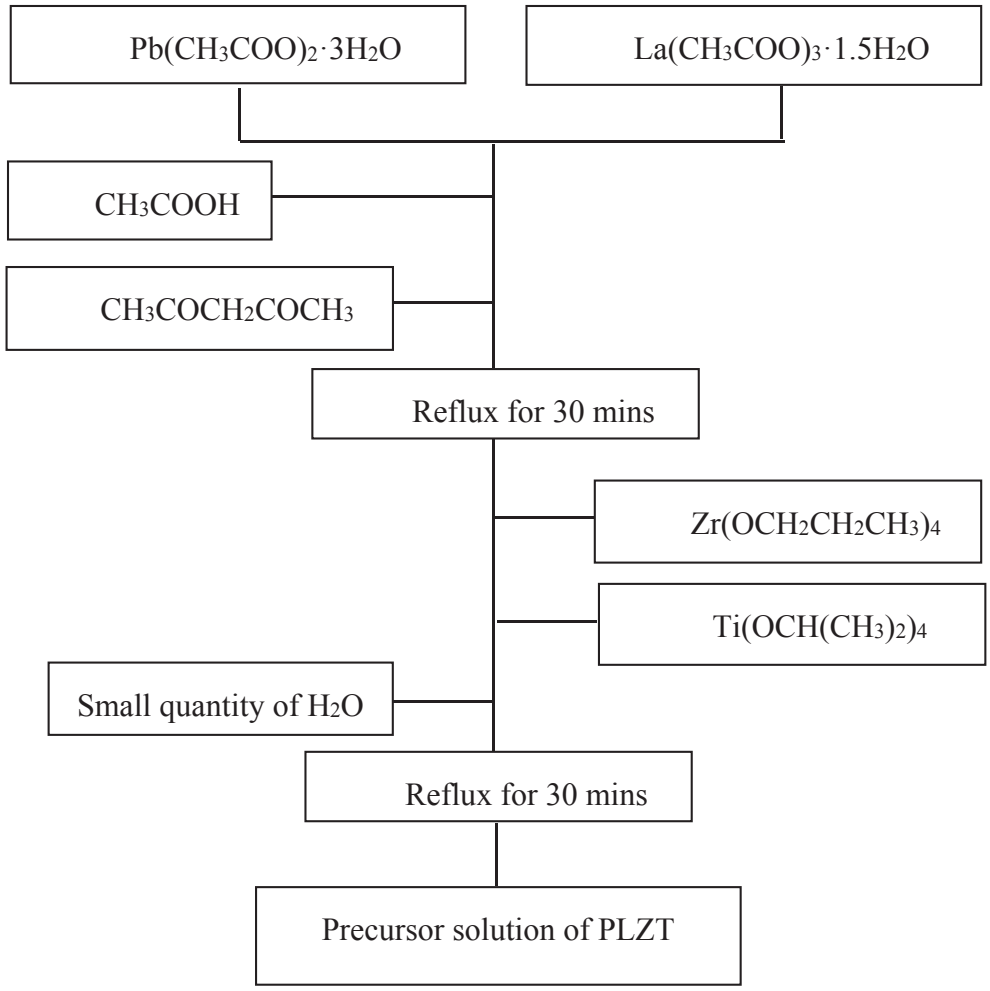

Figure 3.4 Flowing diagram of preparation of PLZT precursor solutions

3.3 Characterization Techniques

3.3.1 X-Ray Diffraction (XRD) Analysis

X-ray diffractometers (Siemens D5000, München, Germany) were used to characterize ceramic targets and related thin films. All the XRD patterns were collected using Cu Kα radiation in a step-scan mode with voltage and current at 40 Kv and 40 mA. XRD patterns were obtained at a scan speed of 0.4°/min with a scan step of 0.04° over 2θ range of 20-60° for phase identification.

3.3.2 Scanning Electron Microscopy (SEM)

A high resolution scanning electron microscopy (SEM, Ultra55, Zeiss, Oberkochen, Germany) equipped with a field-emission source were used to examine the microstructure and morphology of PZ thin films. Also, the thicknesses of the films were determined with FE-SEM from film cross-section observations. The acceleration voltage used was between 5-15 kV. Work distance was between 8 to 15 mm.

3.3.3 Atomic Force Microscopy (AFM)

AFM is a microscopic technique that measures the morphology and properties of surfaces on the atomic scale operating under environmental conditions. It can be used to measure surface topography, surface hardness, and elastic modulus. The interaction that is monitored in AFM is the Van Der Waals force between the tip and the surface; this may be either the short-range repulsive force (in contact-mode) or the longer-range attractive force (in non-contact mode). For AFM, a sharp tip, typically made from Si_3N_4 or Si is placed at the end of cantilever with a very low spring constant. The nanoscope AFM head employs an optical detection system in which the tip is attached to the underside of a reflective cantilever. A diode laser is focused onto the back of a reflective cantilever. As the tip scans the surface of the sample, moving up and down with the contour of the surface, the laser beam is deflected off the attached cantilever into a dual element photodiode.

In the present work, the surface morphologies of the thin films were imaged using contact mode atomic force microscopy (AFM, Veeco, Santa Barbara, CA, USA).

3.3.4 Electrical Measurements

For electrical measurements at low frequency, metal-insulator-metal (MIM) structure capacitors were defined by standard photolithographic lift-off technique using dc magnetron sputtered 120-nm-thick Pt electrodes ($A=1.766\times10^{-4}$ cm^2) on the films surface. The capacitors were then annealed at 500 °C for 60 min in ambient air to improve the top electrode/PZ interface. The dielectric properties of the films with MIM structure were measured with an Agilent 4192A (HP, Englewood, CO, USA) precision impendance analyzer by applying 100 mV oscillating test field at frequency of 10 kHz at room temperature (RT). The MIM structure for capacitance measurement was shown in Fig. 3.5. The dielectric constant of the films ε_r was extracted from the capacitance by the equation: $\varepsilon_r=Cd/\varepsilon_0A$. Where d is the thickness of the film and A is area of the top electrode.

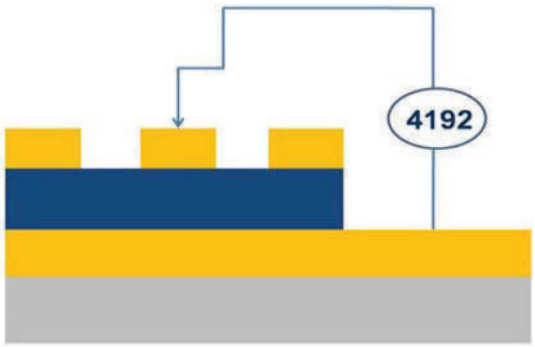

Figure 3.5 The MIM structure for capacitance measurement

CHAPTER 4

Preparation and Energy storage of PZNT Films

Chapter 4 Preparation and properties of PZNT films

The demand of high power density storage applications needs the dielectric materials to have relative high dielectric constant, saturated polarization, low dielectric loss and good stability. Meanwhile, the capacitors are often needed to operate under different electric field and frequencies in practical applications. Hence, investigation on the effect of electric field and frequencies on the properties of AFE films becomes very important.

There are literatures reported[18,19] that Nb dopants can help the AFE materials to possess a sharp electric field induced phase transition with square shape of hysteresis loop, which is good for energy storage applications.

4.1 Structure information of PZNT films

The composition of the film is chosen as $Pb(Zr_{0.96}Ti_{0.03})Nb_{0.01}O_3$. Firstly, we deposited three kinds of electrodes as LNO, Pt, $La_{0.5}Sr_{0.5}CoO_3$ (LSCO) on SiO_2/Si substrates. The thickness of PNZT film is about 1 μm and bottom electrodes is about 200 nm. Fig. 4.1 shows the XRD patterns of PNZT films on different bottom electrodes. Because the thickness of PNZT films is much larger than bottom electrode, hence the intensity of PNZT peak is much higher than bottom electrode LNO and LSCO. We can see from the map than all the films are showing a pervoskite structure with no impurity phase detected. For convenience, we marked the peak as cubic structure. The PNZT film on LSCO didn't show any preferred orientation. In contrast, on Pt electrodes PNZT film has a (111)

preferred orientation and LNO bottom electrodes facilitate PNZT film to be (100)-oriented.

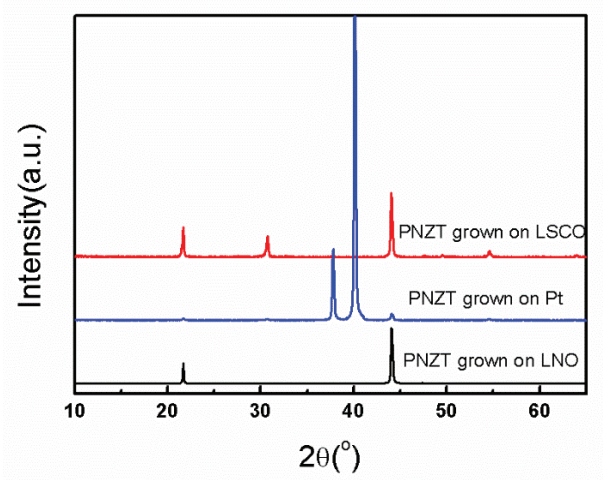

Figure 4.1 Room temperature XRD of films with different bottom electrode

Fig. 4.2 shows the SEM figures of surface of PNZT films on different electrodes. We can see that the grain size of PNZT films are similar, about 100 nm in diameter. It is worth noticing that the films are not very dense, however, we can see very small grains above the bigger ones. It is possibly due to the loss of Pb in the surface of PNZT films. To obtain a better morphology, it is suggested to put a layer of PbO solution to compensate the loss.[18] However, it is worth noting that the thickness of PbO layer should be carefully controlled, an excess of PbO will also damage the surface and properties of films severely.

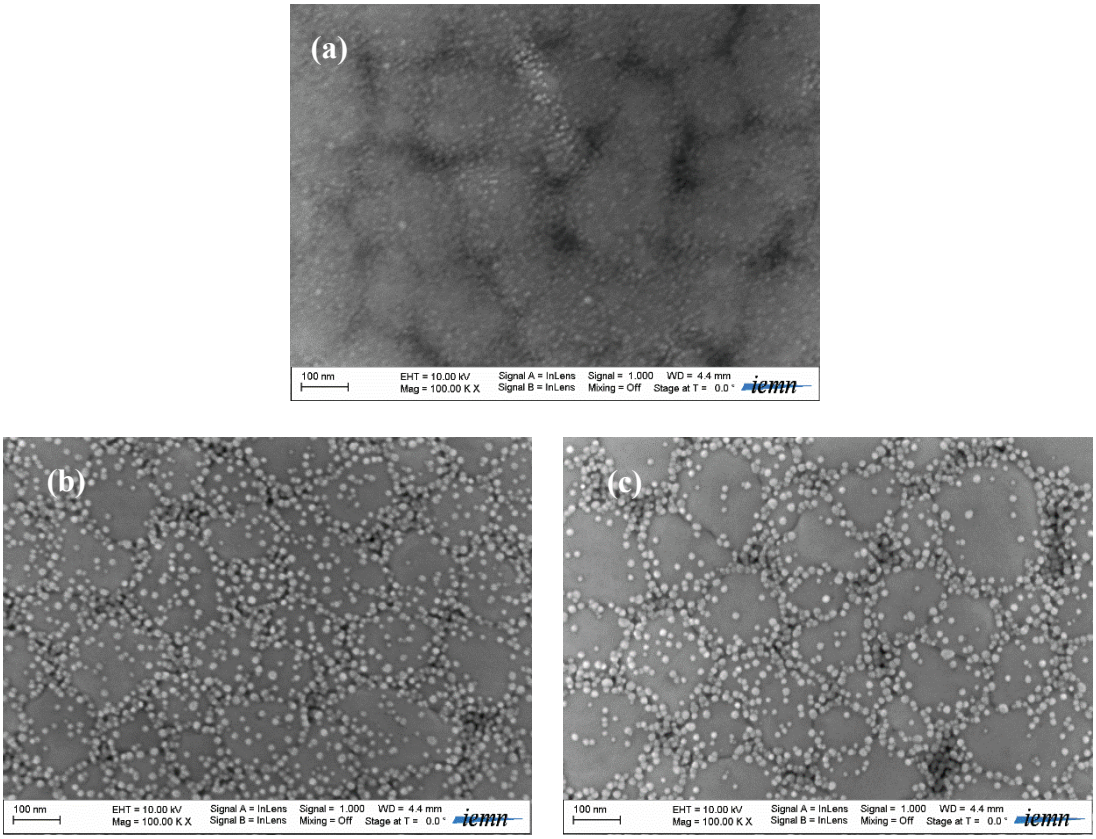

Figure 4.2 Surface SEM of PZNT films (a) LNO (b) Pt (c) LSCO bottom electrode

Fig. 4.3 shows the SEM figures of cross-section of PNZT films on different electrodes. We can see clearly the thickness of each layer because we annealed the film layer by layer. And we can also see that small grains exist between layers and this is consistent with the SEM figures of the surface. Hence this indicates that the small grains only formed in the surface of each layer and are very few so should not have large influence on the films.

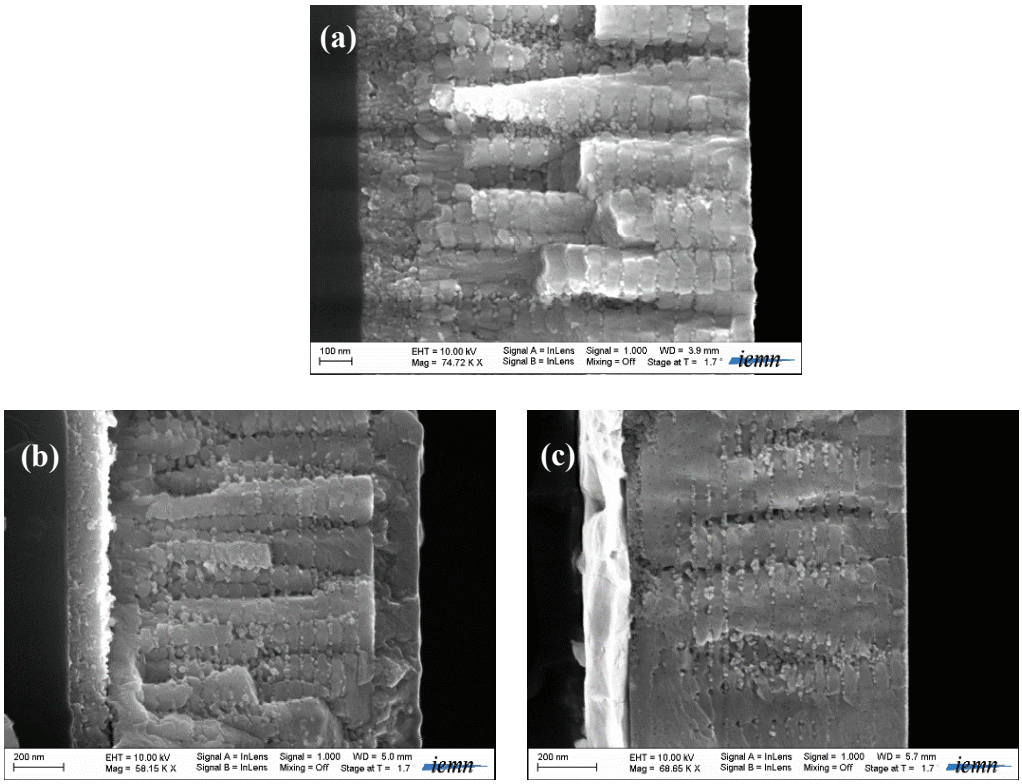

Figure 4.3 Cross-section SEM of PZNT films (a) LNO (b) Pt (c) LSCO bottom electrode

4.2 Dielectric properties

Fig. 4.4 shows the curve of ε_r-T of PZNT films. At room temperature, the relative dielectric constant ε_r of PZNT films is about 300. With the increasing of temperature, ε_r increases and reaches the peak of 2200 at 218 ^oC, which is 7 times bigger than the value at room temperature. It is worth mentioning that because of the broadness of dielectric properties in films, the ratio of maximum ε_r and ε_r at room temperature is normally about 4. Hence, our result indicates that the films have very good crystallinity. In addition, compared with ferroelectric PZT films, which normally show a maximum ε_r of 1000, the Nb^{5+} dopant might correspond to the larger ε_r here.

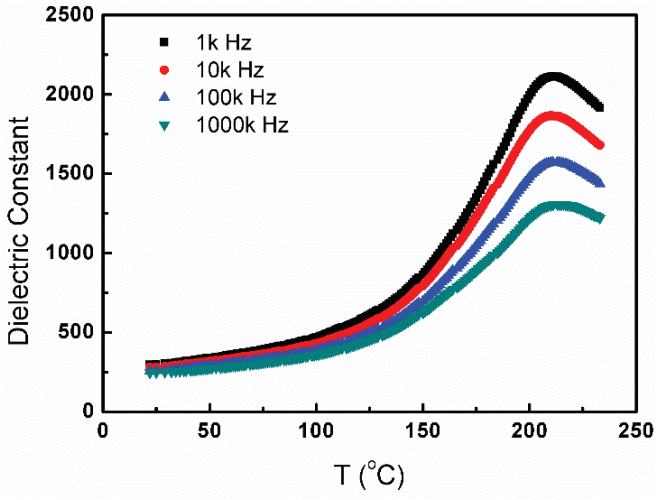

Figure 4.4 ε-T curve of PZNT films with Pt bottom electrodes

4.3 Polarization properties

Figure 4.5 shows the hysteresis loops of PNZT films on LNO bottom electrodes with different frequencies at room temperature. As we can see from the map, the loop is in a typical AFE shape. The phase transition field $E_{AFE\text{-}FE}$ is about 350 kV/cm and $E_{FE\text{-}AFE}$ is about 120 kV/cm. The relatively high remanent polarization means the films contain a certain amount of FE phase. Figure 4.6 gives us information on the relation of P_s and P_r with the frequency. We can see that P_s and P_r decrease with the increase of frequency. This might be because induced FE phase is retained due to the high frequency of measurement.

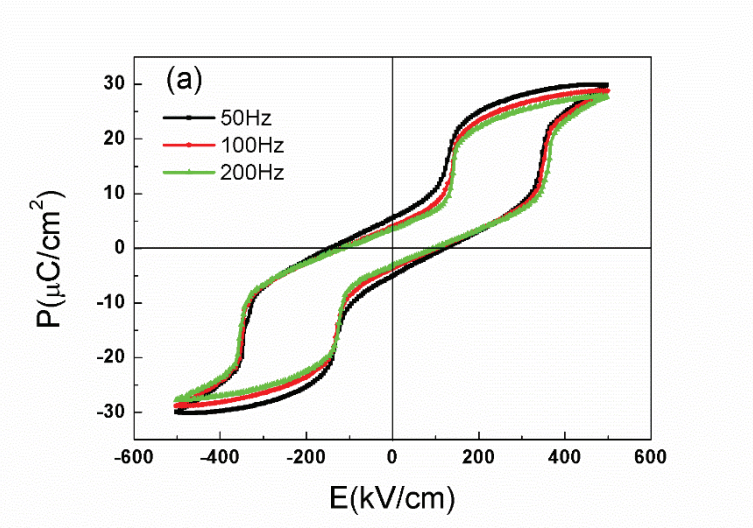

Figure 4.5 *P*-E loops of PZNT films with LNO bottom electrode at different frequencies

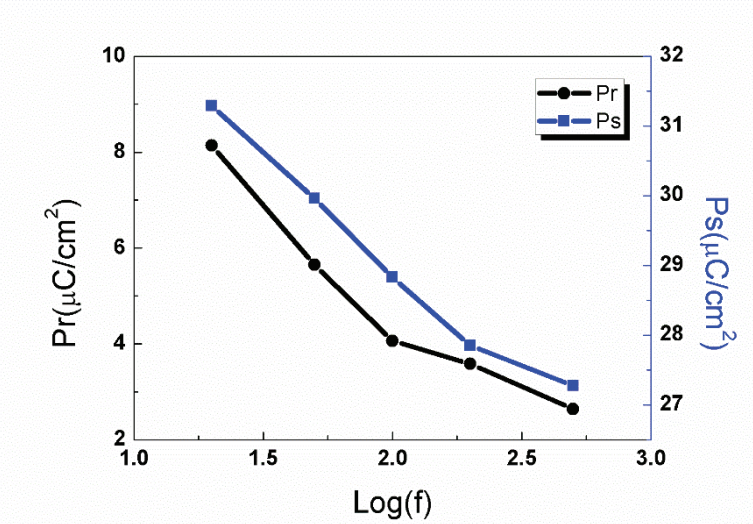

Figure 4.6 Relations of P_s and P_r with frequency for PZNT films with LNO bottom electrode

Fig. 4.7 shows the hysteresis loops of PNZT films on Pt bottom electrodes with different frequencies at room temperature. Compared with the sample with LNO bottom electrodes, the film contains more FE phases. Because of the broadness of phase transition, the value of $E_{AFE\text{-}FE}$ is hard to define. $E_{FE\text{-}AFE}$ is about 50 kV/cm, which is less than 50% compared with film on LNO bottom

electrodes. This is because the PZNT film is (111)-oriented on Pt electrode and it is the same direction where the polarization of PNZT unit cell lies in. Hence it is more easily to be polarized.

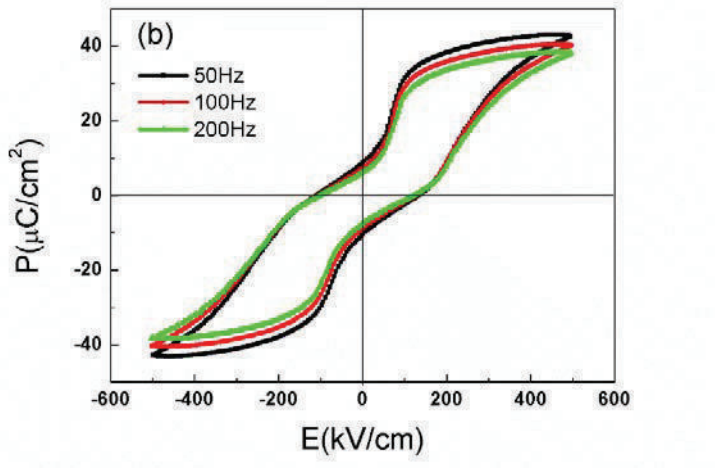

Figure 4.7 *P*-E loops of PZNT films with Pt bottom electrode at different frequencies

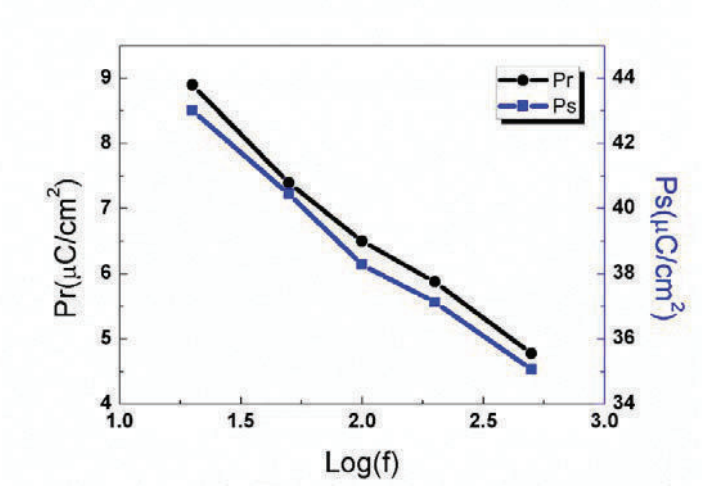

Figure 4.8 Relations of Ps and Pr with frequency for PZNT films with Pt bottom electrode

Fig. 4.8 shows the relations of P_s and P_r with frequency. We can see from the map that, P_s and P_r decrease with the increase of frequency. Fig. 4.9 gives the

hysteresis loop of PZNT at different frequencies at 500 kV/cm. Different with the other two kinds of films above, the P_s and P_r show trends that are not the same. P_s decreases with the frequency increasing, while P_r increases at first and then decreases with the frequency increasing. We believe it is due to the larger amount of retentive FE phases. With the increase of frequency, more and more FE phases do not have enough time to turn back to AFE phases, hence leading to the increase of P_r.

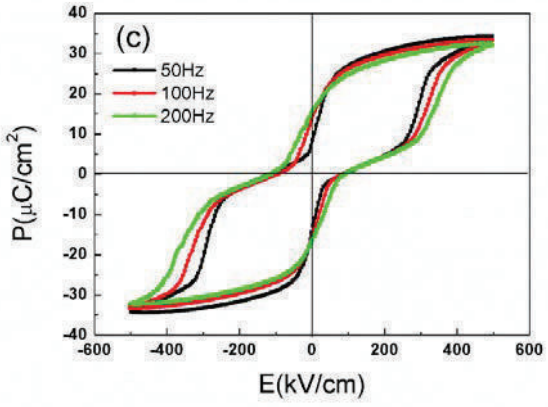

Figure 4.9 *P*-E loops of PZNT films with LSCO bottom electrode at different frequencies

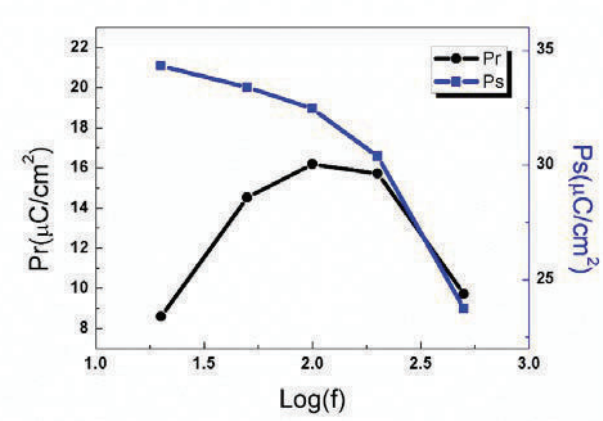

Figure 4.10 relations of Ps and Pr with frequency for PZNT films with LSCO bottom electrode

4.4 Energy storage properties

According to the P-E loops in section 4.3, we caculated the energy density of three kinds of films with the freuqency. Fig. 4.11 shows the curve of log energy density log(W) with log(*f*). We can see that with the increasing of frequency, the W of PZNT on LNO bottom electrode increases slowly with a relation of $W \propto f^{0.08}$; however, the W of PZNT on Pt bottom electrode remains basically unchanged; in contrast, the W of PZNT on LSCO bottom electrode decreases with a relation of $W \propto f^{-0.14}$. As we mentioned before, the decrease of W with frequency in PZNT on LSCO bottom electrode can be attributed to the larger amount of FE phase remaining. This means some of the energy is still stored in these phases and does notrelease, hence resulting in a decrease the W of films.

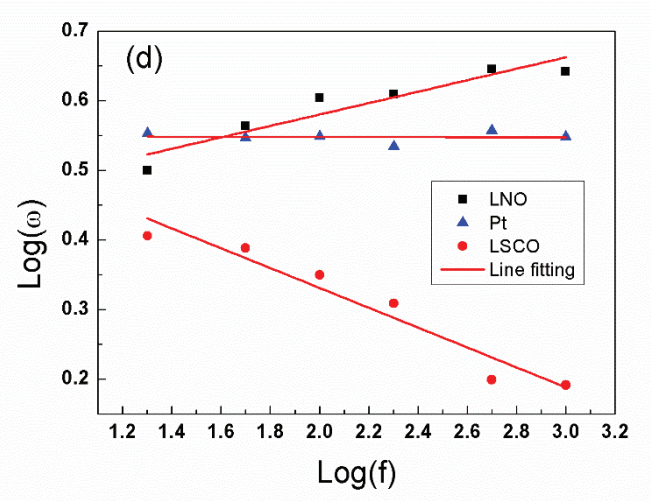

Figure 4.11 The relation of log(W) against log(*f*) for the saturated hysteresis loops

To further confirm our speculation, we draw the curves of energy density with electric field for the samples. Fig. 4.12 shows that the curve of PZNT film on LNO bottom electrode is “step” like, which is often observed in AFE materials.

The energy densities rise steeply from 0.96 to 3.49 J/cm^3 with increasing of *E* from 300 to 400 kV/cm. On the other hand, film on Pt bottom electrode shows a little diffused curve and the energy density at 400 kV/cm is 3.28 J/cm^3 which is a little less than that of film on LNO bottom electrode. This could be explained by the increase of stable retained FE state in film grown on Pt/SiO_2/Si. Especially, for film on LSCO bottom electrode, the energy density shows a much more diffused curve with only a little jump from 0.94 to 1.77 J/cm^3 between 300 and 400 kV/cm, which is very similar to that of soft Nb doped ferroelectric $Pb(Zr_{0.52}Ti_{0.48})O_3$ ceramics[13]. The results indicate a much higher percentage of stable FE phase retention in PZNT films on LSCO/SiO_2/Si, which further prove the result we discussed before.

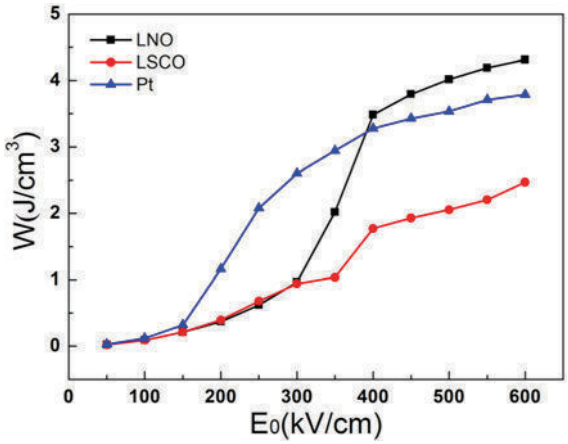

Figure 4.12 Dependence of energy density W on field amplitude E0 at 100 Hz

The coexistence of ferroelectricity and antiferroelectricity in films has been explained by the lattice strain[36,76] or surface charges and self-biasing[77] at the interfaces between the films and substrates. However, these interpretations seem

not to work for our films because they are all based on a precondition that the films should be at least thinner than 300 nm. Here, we believe there are two major factors influencing the results in our cases. The first one is related to the nonuniform strain field. When the grains in films deform because of polarization switching under the applied electric field, each grain containing AFE/FE domains experiences a strain field, depending on the orientation of adjacent grains and configuration of domains therein. As we mentioned before, film on LSCO bottom electrode is less oriented than LNO and Pt film so one can expect to see more nonuniform strain field of film on LSCO bottom electrode. The result is that in some regions of film, the strain field is large enough so that the field-induced FE phase may no longer be able to switch back, therefore, giving rise to the relatively larger remanent polarization.

The second potential cause is related to the depolarization field generated during polarization. Normally the depolarization field substantially affects the physical properties of ferroelectrics, because this field tends to suppress spontaneous polarization and, thus, to destroy the ferroelectric state. However, the depolarization field may help the FE phases to return back to AFE phases in antiferroelectic. Electrode can considerably decrease the depolarization field.[81,82] For example, superconducting electrodes in bulk ferroelectrics lead to complete compensation for the depolarization field[81]. The PZNT films can be treated as p-type semiconductors because of the unavoidable Pb vacancies,[83] so at the PZT/LNO[84,85] and PZT/LSCO[86] interfaces, p-n-like and p-p-like junctions will be

formed. However, the barrier height in the p-p junction is usually lower,[84,85] whereas the barrier height in the p-n junction should be larger [83] and compensation for the depolarization field is difficult resulting in an easier returning back to AFE phases at low electric field and smaller remanent polarization.

4.5 Conclusion

In summary, energy-storage properties and scaling behavior of $Pb(Zr_{0.96}Ti_{0.03})Nb_{0.01}O_3$ films using different bottom electrodes were first investigated. Although with similar composition and thickness, the scaling relation for energy densities of films on $LNO/SiO_2/Si$ takes the form of $W \propto f^{0.08}$, which is very different from $W \propto f^{-0.14}$ of films on $LSCO/SiO_2/Si$. Additionally, the scaling relation of films on $Pt/Ti/SiO_2/Si$ shows that W is basically independent of frequency. These behaviors demonstrate that electrode materials might heavily influence the scaling behavior of energy density in $Pb(Zr_{0.96}Ti_{0.03})Nb_{0.01}O_3$ antiferroelectric films, which is closely related to the nonuniform strain field and depolarization field generated within the AFE films.

CHAPTER 5

Preparation and Energy storage of PLZT Films

Chapter 5 Preparation and energy storage properties of $Pb_{0.97}La_{0.02}Zr_{(0.95}Ti_{0.05)}O_3$ AFE films

Because of the electric field induced AFE-FE phase transition, PZT with high Zr content are of high interest for sensor, actuator and transducer applications. According to the recent report, certain amount of La^{3+} dopants can dramatically increase the saturated polarization of the film, hence is helpful to enhance the energy density W.[58] Ma et al. deposited $Pb_{0.92}La_{0.08}Zr_{(0.95}Ti_{0.05)}O_3$ on metal foils and an energy density as high as 50 J/cm^3 can be obtained in their films.

However, in general the investigation on La^{3+} doped Zr-rich PZT film is still quite rare, hence in this chapter we investigated the properties of $Pb_{0.97}La_{0.02}Zr_{(0.95}Ti_{0.05)}O_3$ (PLZT) films made by CSD method.

5.1 Preparation of bottom electrode

5.1.1 Introduction

From conclusions of last chapter we know that, bottom electrode can have a huge impact on the properties of AFE films. Hence, it is very important to obtain good bottom electrodes for enhancing the performance of AFE films, hence, in the following section we will describe the procedure of preparation of $La_{0.7}Sr_{0.3}MnO_3$ (LSMO) films.

Lanthanum strontium manganite is an oxide ceramic material with a perovskite-based crystal structure. LSMO has a rich electronic phase diagram,

including a doping-dependent metal-insulator transition, paramagnetism and ferromagnetism.

5.1.2 Experiments

Firstly we use a conventional synthesize method to prepare LSMO ceramic target. The image of target is shown in Figure 5.1. The detailed procedure of preparation of the target can be found in chapter 3. The target is sintered under 1850 ^{o}C for 2 h to crystallize into perovskite phase.

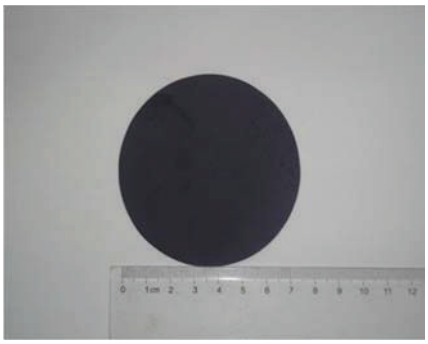

Figure 5.1 Picture of LSMO ceramic target

Figure 5.2 shows TG-DTA results of LSMO powders. The powders loss their weights severely around 400 ^{o}C and 800 ^{o}C. However, the weight does not change after 900 ^{o}C. Hence, our synthesize temperature is set to 900 ^{o}C.

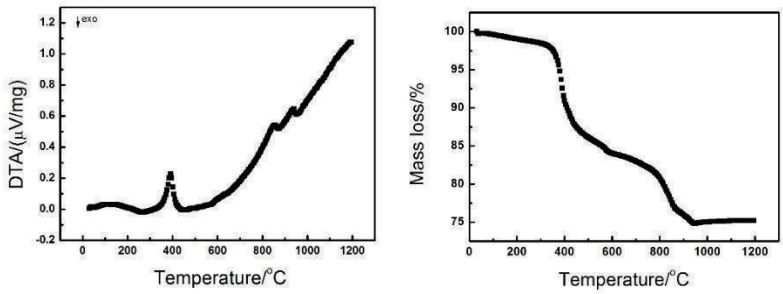

Figure 5.2 TG-DTA curves of $La_{0.7}Sr_{0.3}MnO_3$ powders

Table 5.1 gives the deposition parameters of LSMO films. After deposition, the film is submitted to conventional furnace for annealing at 650 °C for 1 h.

Table 5.1 Details of the LSMO thin films deposition conditions

Deposition parameter	values
Vacuum (Pa)	$<3\times10^{-7}$
Deposition pressure (Pa)	1
Power density (W/cm^2)	~3.90
Gas	Ar/O_2：4/1
Deposition rate (nm/min)	~8
Target	stoichiometric LSMO ceramic
Substrate temperature (°C)	500

5.1.3 Results and discussion

Figure 5.3 shows the XRD results of LSMO films after annealing. We can see that the film shows a typical pervoskite structure and has a (110)-preferred orientation.

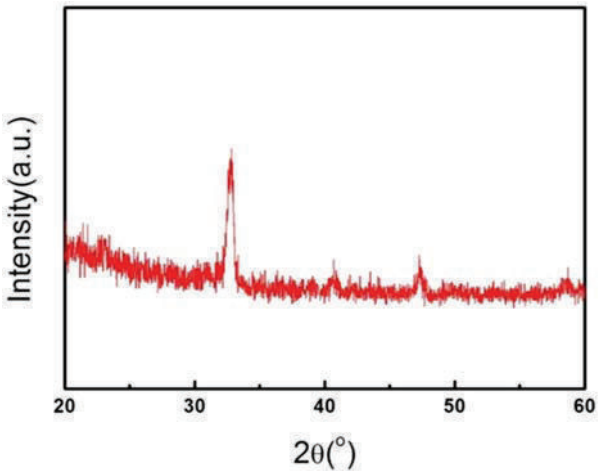

Figure 5.3 XRD of LSMO films made by sputtering

Figure 5.4 shows the cross-sectional and surface SEM images of LSMO films. The film are very dense with a grain size of about 25 nm.

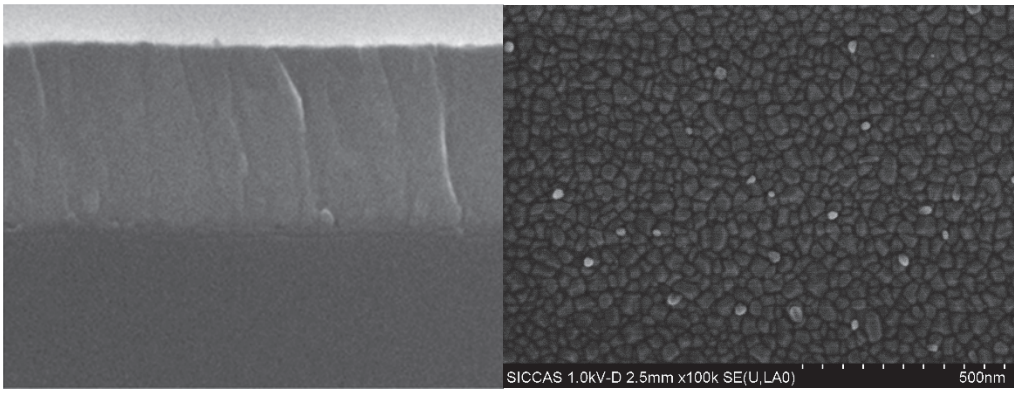

Figure 5.4 Cross section and surface SEM image of LSMO film

Figure 5.5 depicts the curve of electric resistance of LSMO film with temperature. We can see that with the increasing temperature, the resistance increases at first and reaches a peak at around 200 K, where resistance starts to decrease with temperature, corresponding to a metal-insulator phase transition.[87-89]

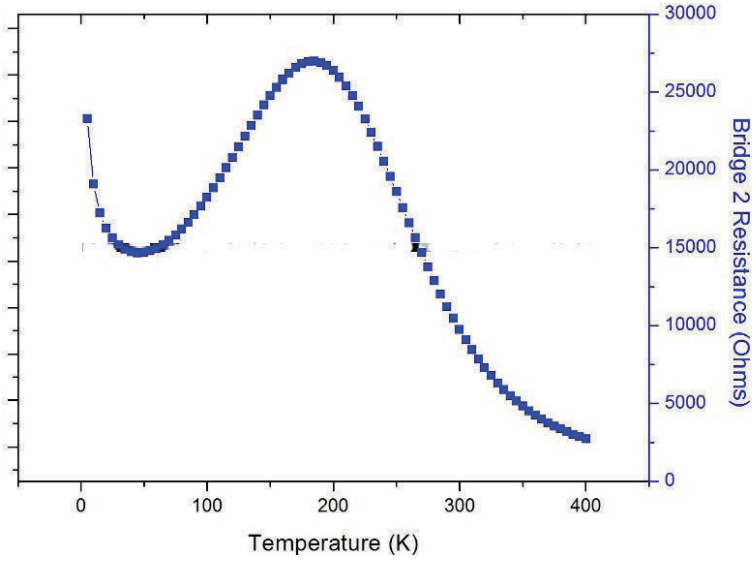

Figure 5.5 variation of resistnace of LSMO with temperature

5.1.4 Conclusion

We deposited LSMO bottom electrode on SiO_2/Si substrate by RF-magnetron sputtering. The film has pure pervoskite phase without any impurity detected from XRD result. The cross-sectional and surface SEM images show that the film is very dense with a grain size of about 25 nm in diameter. From the curve of electric resistance of LSMO film with temperature we can see that LSMO film has a metal-insulator phase transition around 200K.

5.2 Preparation of characterization of PLZT/LNO AFE films

5.2.1 Introduction

$PbZrO_3$ film has relatively high phase transition field, however, with low saturated polarization value, which leads to low energy storage densities. PLZT antiferroelectric film has relatively high energy density, hence has drawn some attention in recent years. At present, there are some reports of PLZT AFE films on substrates with Pt bottom electrode. However, films on Pt bottom electrodes are subjected to fatigue,[80,83] which should decrease the energy density W and energy storage efficiency dramatically. Using oxide metal can effectively solve the problem of fatigue.[90-92] Hence in this part of work, we will present the PLZT films made by CSD method on $LaNiO_3$ buffered SiO_2/Si substrate. We found that via modification of the solution preparation, the microstructure of films could be improved and hence enhancing the properties of PLZT films.

5.2.2 Experiments

The preparation method of LNO bottom electrode has been shown in chapter 3. For the solution of PLZT, first we mixed $Pb(CH_3COO)_2 \cdot 3H_2O$ and lanthanum acetate powders in CH_3COOH. Then we added Zr propoxide and Ti isopropoxide and reflux for 1 hour. After we divide the solution into two parts, in one part we added glycerin and lactic acid as stabilizer, named as solution A; while in the other part we added diacetone as stabilizer, named as solution B. The concentrations of two kinds of solutions are both adjust to 0.3 M. The films are annealed at 600 ^oC.

5.2.3 Results and discussions

Figure 5.6 shows the XRD patterns of PLZT AFE films with different thicknesses. Derived from the position of each peak, we calculated the lattice parameter of films and the degree of orientation (100) and (110) which are shown in table 5.2. The formula to calculate the degree of orientation is shown below.

$$\alpha_{(100)}=\frac{I(100)}{I(100)+I(110)+I(111)+I(200)+I(210)} \quad (5\text{-}1)$$

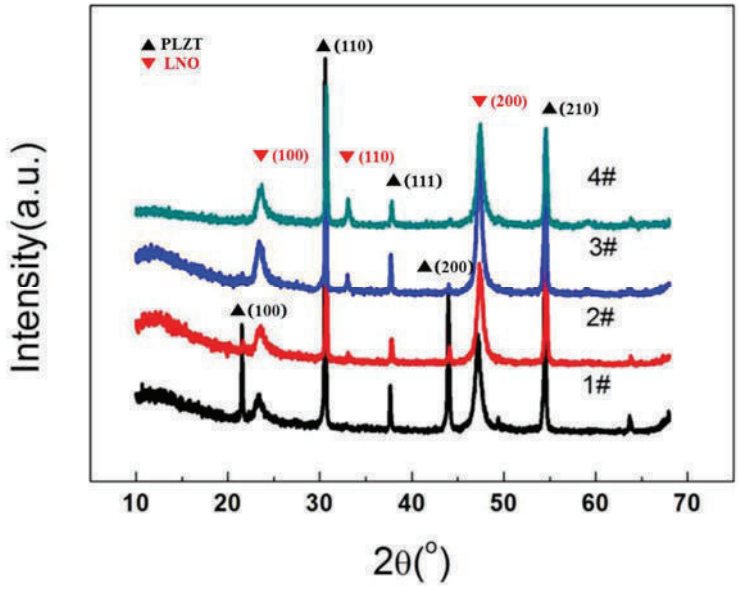

Figure 5.6 XRD of PLZT films of A group with different thickness

Table 5.2 Lattice parameter, $\alpha_{(100)}$ and $\alpha_{(110)}$ of PLZT films with different thickness

Sample	thickness	*a* (Å)	*c* (Å)	$\alpha_{(100)}$ (%)	$\alpha_{(110)}$ (%)
1#	750	4.134	4.118	29	46
2#	600	4.116	4.105	3	47
3#	450	4.113	4.124	3	43
4#	300	4.113	---	0	53

Figure 5.7 shows the variation of lattice parameter α with thickness. From the figure we can see that, with the increase of thickness, the parameter α increases slowly. This could be attributed to the thermal stress that come from the different thermal expansion coefficients (TECs) of films and substrate. The TECs of $PbZrO_3$ and SiO_2/Si are 2.6 and 8.0 ppm/K, respectively. Hence, the films should receive tensile stress on SiO_2/Si substrate and this should decrease the lattice parameter. Hence with the increase of thickness, the lattice parameter should increase as the stress is released by lattice relaxation.

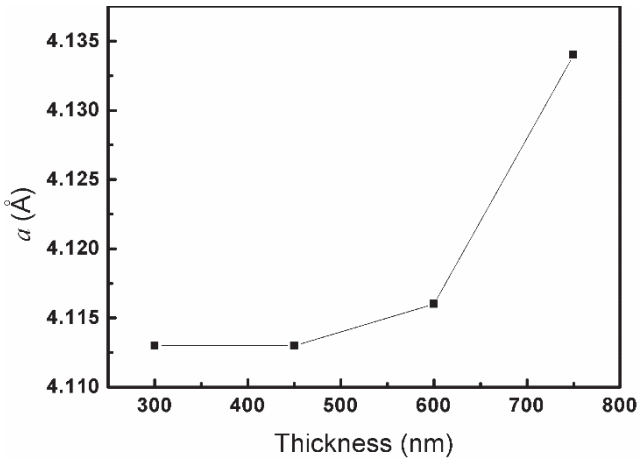

Figure 5.7 Relation between lattice parameter *a* and thickness

Fig. 5.8 and 5.9 depict the relations of degree of orientation $\alpha_{(100)}$ and $\alpha_{(110)}$ with thickness. We can see that $\alpha_{(100)}$ increase from 0% to 30% with the increase of thickness, while $\alpha_{(110)}$ decrease from 53% to 46%.

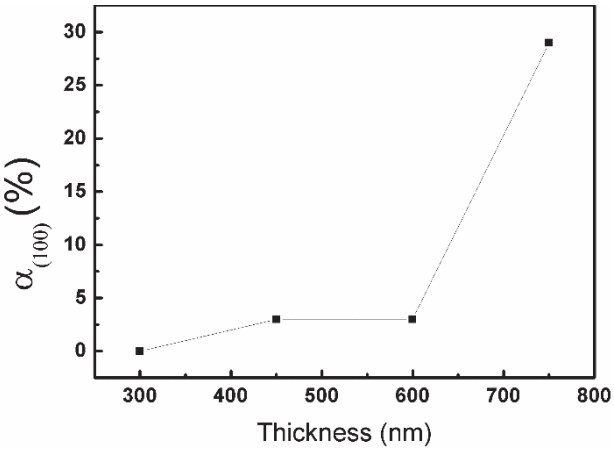

Figure 5.8 Relation between $\alpha_{(100)}$ and thickness

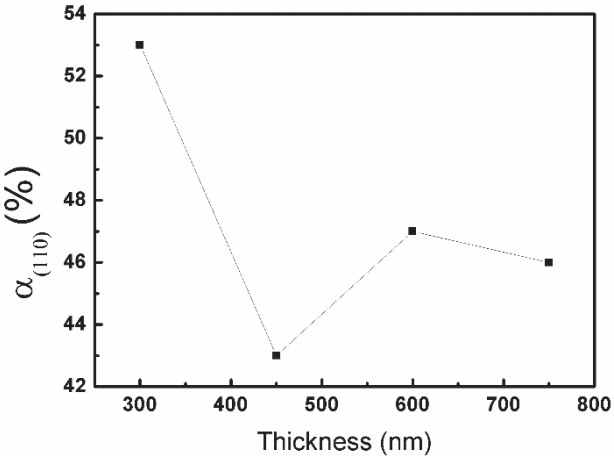

Figure 5.9 Relation between $\alpha_{(110)}$ and thickness

Fig. 5.10 shows the surface SEM picture of PLZT with different thicknesses. The film with 750-nm thickness has the largest average grain size of which the diameter is about 150 nm. The films with 450 and 600-nm thickness have a little smaller grains, while the films with 300-nm thickness have obvious smaller gains. In addition, around the normal grains, there are many small grains with the diameter of about 10 nm. These small grains are thought to be related with the Pb loss.[80]

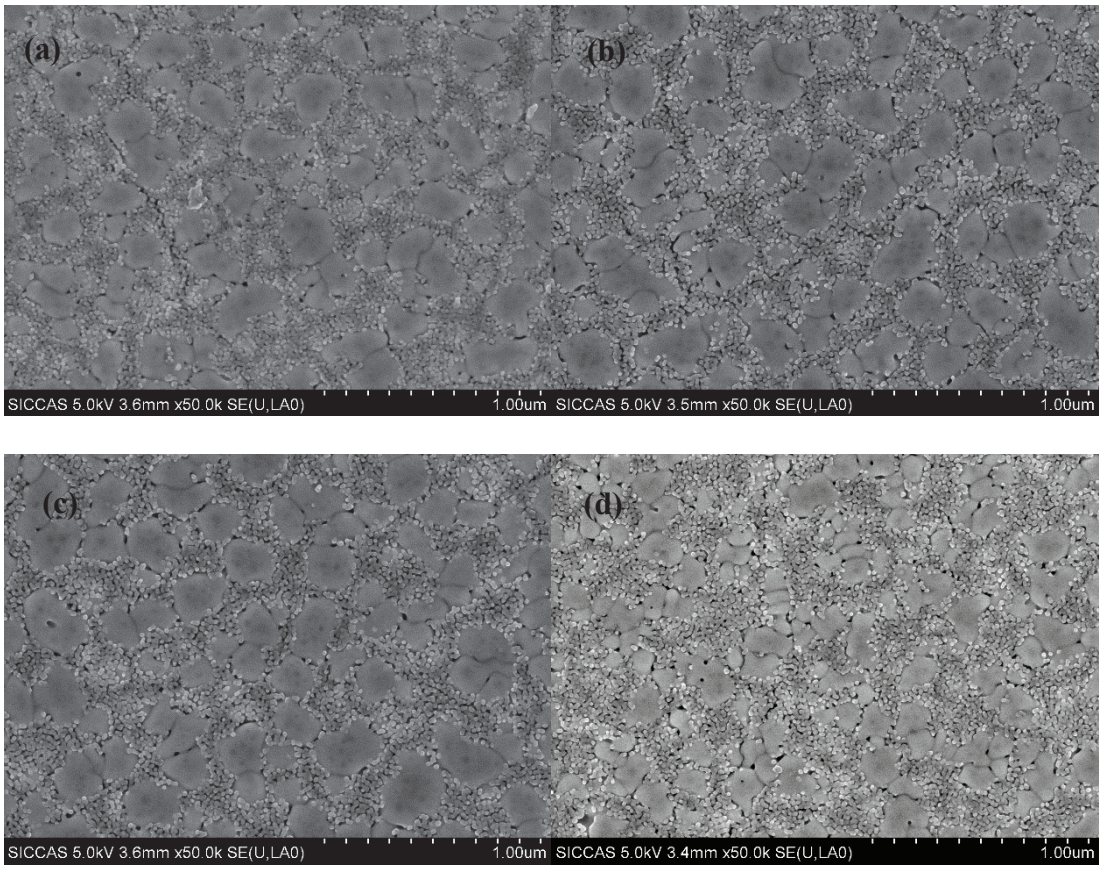

Figure 5.10 SEM surface image of PLZT films with different thickness (a)750 nm (b) 600 nm (c) 450 nm (d) 300 nm

Figure 5.11 gives the hysteresis loops of PLZT films with different thickness. The maximum polarization is between 20 and 30 μC/cm^2. Because of the restriction of measurement conditions, for 750-nm thick film we can not obtain loops with fully saturation. However, it can be seen that the film is a typical AFE with a remanent polarization of about 5 μC/cm^2. With the decreasing of thickness, the remanent polarization increases meanwhile phase transition field decreases. It is not good for energy storage application. We will discuss this phenomenon in details in following chapters.

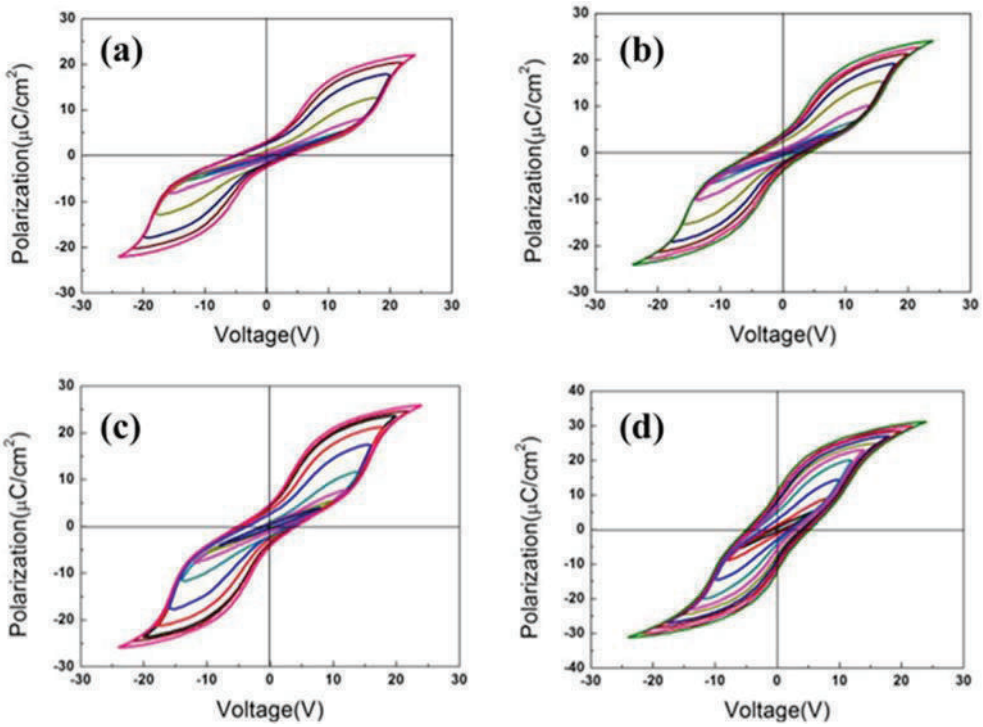

Figure 5.11 Hysteresis loops of PLZT films with different thickness (a)750 nm (b) 600 nm (c) 450 nm (d) 300 nm

Figure 5.12 shows the XRD results of PLZT film under different annealing temperature. All the films have similar thickness of about 300 nm. From the figure we see that, the PLZT films can crystallized at a relatively low temperature of 450 ^{o}C. It is because the LNO bottom electrodes facilitate as a template to help the growth of PLZT.

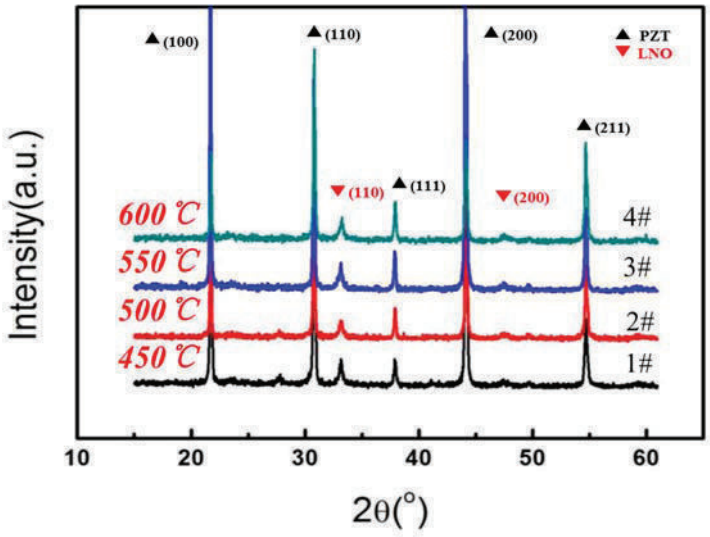

Figure 5.12 XRD of PLZT films of B group with different annealing temperatures

Table 5.3 gives the effect of annealing temperature on lattice parameter, $\alpha_{(100)}$ and $\alpha_{(110)}$. We can conclude that with the increasing of annealing temperature, the lattice parameter doesn't change much. However, the degree of orientations have been influenced. At 550 °C, $\alpha_{(100)}$ is highest while $\alpha_{(110)}$ is lowest. But when the annealing temperature increases to 600 °C, the film shows a large peak of (110) orientation. Hence we can conclude that by controlling the annealing temperature, we can adjust the degree of orientation of our AFE films.

Table 5.3 lattice parameter, $\alpha_{(100)}$ and $\alpha_{(110)}$ of PLZT films with different annealing temperatures

Sample	Annealing Temperature (°C)	*a* (Å)	*c* (Å)	$\alpha_{(100)}$ (%)	$\alpha_{(110)}$ (%)
1#	450	4.102	---	59	27
2#	500	4.104	---	49	32
3#	550	4.104	---	67	21
4#	600	4.102	---	37	37

5.2.4 Conclusion

AFE PLZT films were deposited via a sol-gel process on LNO buffered SiO_2/Si substrates. We investigated the properties of films with thickness and annealing temperature. From XRD patterns we found that the film displayed a pure perovskite structure and no impurity phase is found. SEM figures show that the grain is around 100 nm in diameter while surrounded by very small sub-grains. With the decreasing of thickness, the hysteresis loops degenerate. Annealing temperature could have a big influence on AFE films, especially the degree of orientations.

5.3 Preparation and characterization of PLZT/LSMO films

5.3.1 Introduction

Magnetoelectric films have become a hot research topic around the world because of their both academic and practical applications potential.[88,89,93,94] Magnetoelectric effects can be generated via strain, between two materials such as a ferromagnet (FM) and a ferroelectric. Each phase may then be independently optimized for room temperature performance, and the coupling limit of equation is lifted. Strain coupling requires intimate contact between a piezomagnetic (or magnetostrictive) material and a piezoelectric (or electrostrictive) material. This can be achieved in the form of composites laminates or epitaxial multilayers.

AFE film can generate a large strain (~0.4%)[44,97] during the electric-induced phase transition, hence study in AFE/FM composite film should be interesting. Therefore in the following, we deposited the AFE/FM composite film on SiO_2/Si substrates and investigated its electrical properties.

5.3.2 Experiments

First we deposited LSMO films on SiO_2/Si substrate. Detailed deposition parameters of LSMO can be found in the first part of this chapter. Then we start deposition of PLZT films on top of LSMO by CSD method. The films were prepared through a multiple layers spin coating procedure. Each spun-on PLZT layer was heated at 700 ^oC for 5 min. The spin coating and heat treatment were repeated several times to obtain the desired thickness. These films were further

used to prepare Pt/PLZT/Pt capacitor structures with top electrode (diameter of 150 μm) sputtered through a photolithography process.

5.3.3 Results and discussions

Figure 5.13 shows the XRD results of PLZT/LSMO composite films. According to the Debye-Scherrer formula we can calculate the average grain size:

$$D=K\lambda/\beta\cos\theta \qquad (5\text{-}2)$$

Where D is the mean size of the ordered (crystalline) domains, which may be smaller or equal to the grain size; K is a dimensionless shape factor; λ is the X-ray wavelength; β is the line broadening at half the maximum intensity (FWHM), after subtracting the instrumental line broadening, in radians; θ is the Bragg angle. The calculated grain size is about 60 nm in diameter.

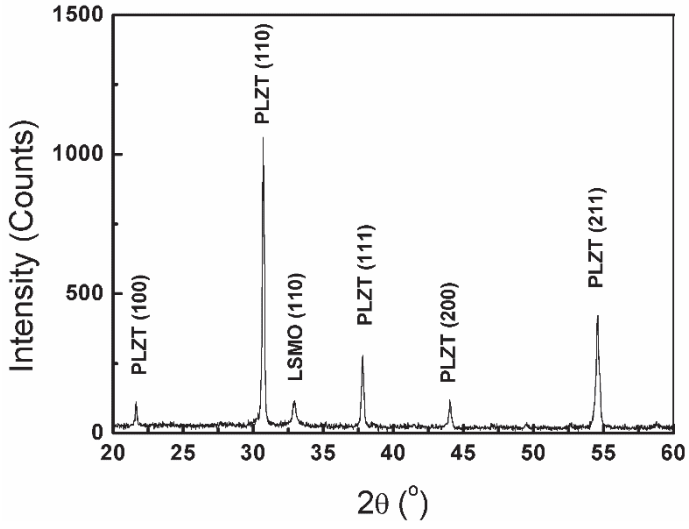

Figure 5.13 XRD of PLZT films with LSMO bottom electrodes

Fig. 5.14 shows the hysteresis loops of PLZT/LSMO at different electrical fields. We found the maximum polarization is about 25 μC/cm^2 with a remanet polarization of 5 μC/cm^2. Also we can see that the electric field induced phase transition is quite broad here and the AFE-FE phase transition voltage is about 12 to 18 Volts.

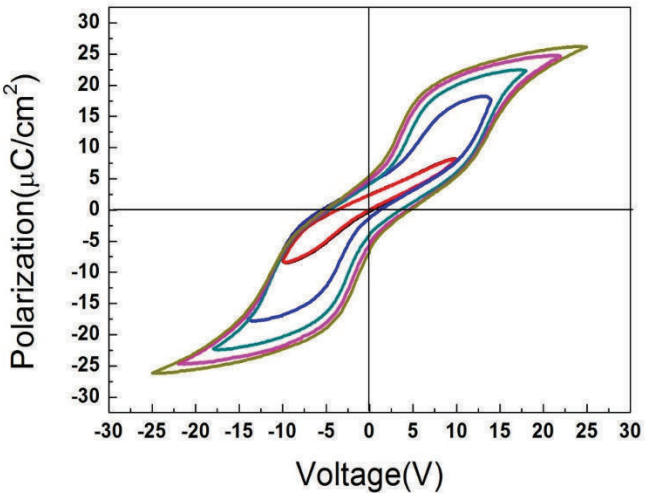

Figure 5.14 Hysteresis loops of PLZT/LSMO films at different electric fields

We test the fatigue properties of PLZT/LSMO films. First we test the behavior of sample after 10^9 times of cycles at 6 V, with a frequency of 10^5 Hz. The results are shown in Fig. 5.15. We can see that the hysteresis loop does not change after 10^9 times of cycles.

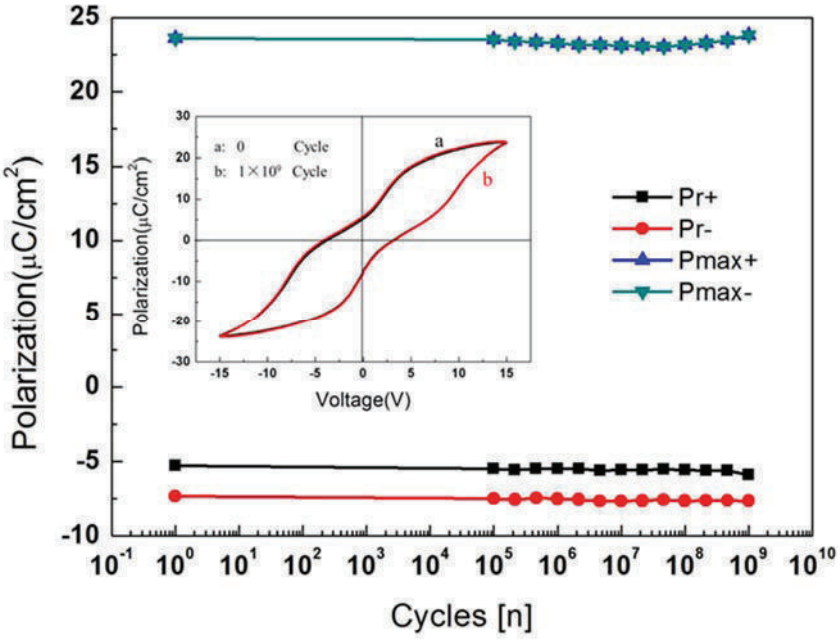

Figure 5.15 Fatigue measurement of PLZT/LSMO film under 6V, inset is the hysteresis loop before and after the cycles

Then we try to increase the testing voltage to excess the phase transition voltage. Hence the testing voltage is set to 10 V. The other parameters maintain unchanged. As we can see in Fig. 5.16, the maximum polarization decreases and remanent polarization increases. The shape of AFE double hysteresis loop becomes more and more ferroelectric like.

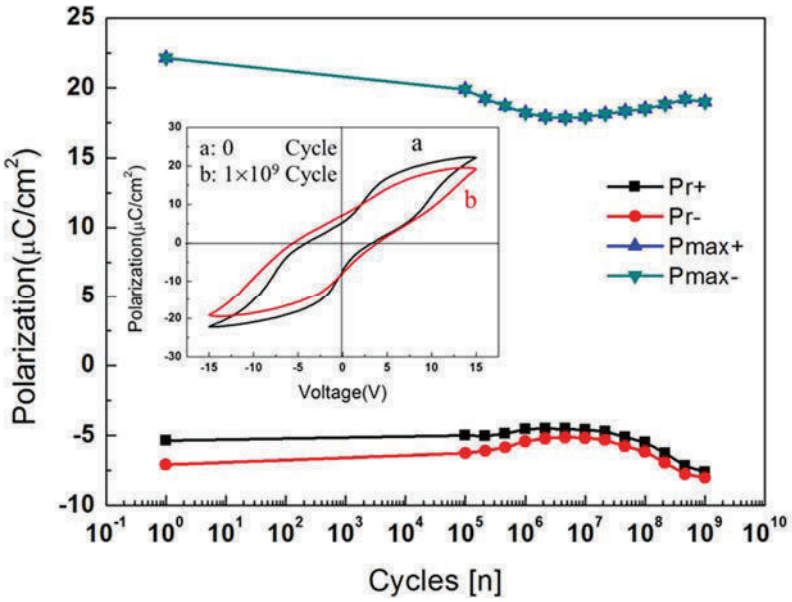

Figure 5.16 Fatigue measurement of PLZT/LSMO film under 6V, inset is the hysteresis loop before and after the cycles

Those behaviors might be understood on the basis of nonuniform strain fields. When the grains in thin films deform due to polarization switching under the applied electric field, they deform differently because of the dielectric and electromechanical anisotropy of individual grains. Each grain containing AFE/FE domains experiences a different degree of expansion/contraction, depending on the orientation of adjacent grains and the configuration of domains therein. Therefore, one can expect to see the internal buildup after repetitive cycles of switching because of the increasing population of retained FE phase as evidenced by the increasing remanent polarization in Fig. 5.16. Some regions may be subject to tensile stresses while other regions may be subject to compressive stresses. These internal stresses could modify the transition field of different regions. Thus, the AFE–FE switching field, or its reverse field, would become more diffused.

5.3.4 Conclusion

PLZT/LSMO composite films were deposited on SiO_2/Si substrate by CSD method. The films display a pure perovskite structure, and no impurity phase is found. The P-E loops show typical AFE double hysteresis loops. We found under a voltage under phase transition, 10^9 times of cycles did not cause fatigue of material, however, when applied voltage excessed the phase transition voltage, fatigue behavior appeared. It might be closely related to the nonuniform strain buildup due to switching that tends to stabilize the FE phase.

5.4 Effect of top electrode on the energy density properties of films

5.4.1 Introduction

The advantages of excellent thermal stability, mechanical toughness, radiation hardness, and desirable electrical properties have made FE/AFE materials candidates for non-volatile memories, infrared detectors, high density capacitors, electro-optic elements, and energy conversion systems.[98,99] Meanwhile, because of lacking electrode materials for high temperature environment, the application of FE/AFE materials at high temperature has been severely restricted. Increased leakage, diminished chemical stability, and poor adhesion of electrodes at elevated temperatures has made this particularly difficult. Fortunately, advances in sophisticated thin-film growth techniques have been made.[101-108] Many experimental and theory studies have found that oxide metals ($SrRuO_3$, $La_{0.5}Sr_{0.5}CoO_3$, SrO, etc.) perform significantly better than elemental metals as contacts due to their structural and chemical compatibility.[109,110] Such oxide metals improve fatigue and retention,[100] can help to minimize imprint,[111] help to prevent the formation of ferroelectric dead layers,[102] and result in large permittivity and remanent polarization even in ultrathin ferroelectric layers. In addition, electrode asymmetry has also been shown to affect temperature dependent properties adversely.[112] As a result, researchers have focused on non-contact techniques (e.g., second harmonic generation[113,114] and XRD) to probe temperature dependent properties of thin films, but quantitative measures of ferroelectric properties are hard to obtain with these techniques.

5.4.2 Experiments

The choice of the composition used in this work is $Pb_{0.97}La_{0.02}Zr_{(0.95}Ti_{0.05)}O_3$ (PLZT). The substrates are (111) oriented, n-type silicon wafers with 120-nm-thick sol-gel derived LNO layer as the bottom electrode. The procedure of preparing LNO bottom electrode has been described in chapter 3. Each layer of LNO films was annealed at 600 ^oC for 6 minutes. The precursor solution for PLZT was prepared from Pb acetate, La acetate, Zr propoxide, and Ti isopropoxide. In order to compensate the lead loss during annealing and prevent the formation of a pyrochlore phase, 20 mol. % excess of lead acetate trihydrate was added, and the films were prepared through multiple layers spin coating procedure. Each spun-on PLZT layer was heated at 700 ^oC for 5 minutes. The spin coating and heat treatment were repeated several times to obtain the desired thickness. The structure and phase purity of the films were checked using XRD in a θ-2θ scan. The surface morphologies and the phase microstructure were observed using SEM. These films were further used to prepare metal/PLZT/metal capacitor structures with top electrode (diameter of ~150 μm) sputtered through a photolithography process. The thickness of $LaNiO_3$ and Pt top electrodes is about 100 nm and for $LaNiO_3$ top electrode, additional Pt (~ 80 nm) layer was sputtered on top of it to facilitate the contact for electrical characterization. The hysteresis loops were performed by aixACCT TF2000FE equipment.

5.4.3 Results and Discussions

Figure 5.19 shows two typical XRD patterns of PLZT films with thickness of 100 and 250 nm, respectively. It can be observed that all films display a pure perovskite structure, and no impurity phase is found. Although the Si substrate is (111) oriented, the $LaNiO_3$ layer shows highly oriented (100) fiber texture, which facilitates the high (100) orientation of the overlaying PLZT films. It has been suggested that the (100)-oriented nuclei of $LaNiO_3$ have lower surface energy than the (110)-oriented nuclei, which may be the reason for the (100)-oriented growth of $LaNiO_3$ layer. Cross-sectional SEM image of films with thickness of 150 nm is shown as an inset in Fig. 5.19. All films exhibit a dense and columnar microstructure in the thickness range studied.

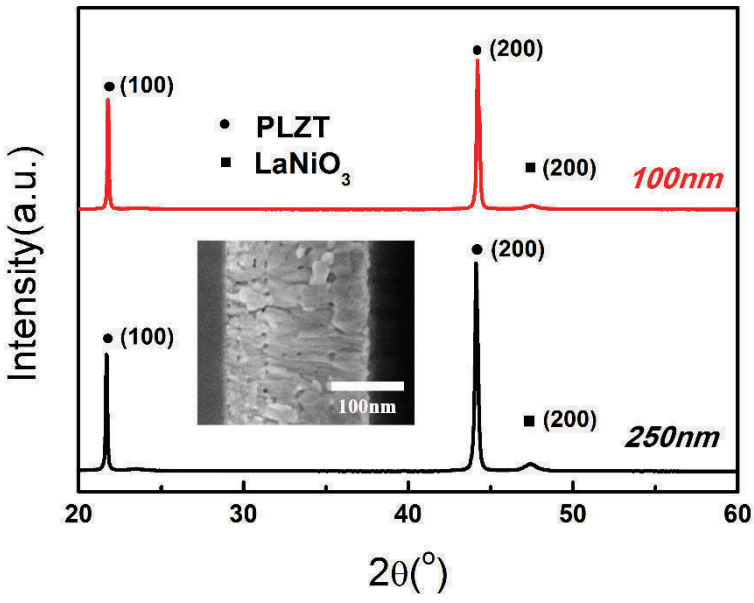

Figure 5.19 Room temperature XRD θ-2θ of PLZT films with thickness of 100nm and 250 nm, respectively. The inset shows the microstructures of the cross-section of the PLZT/$LaNiO_3$/Si films with thickness of 150 nm for PLZT layer

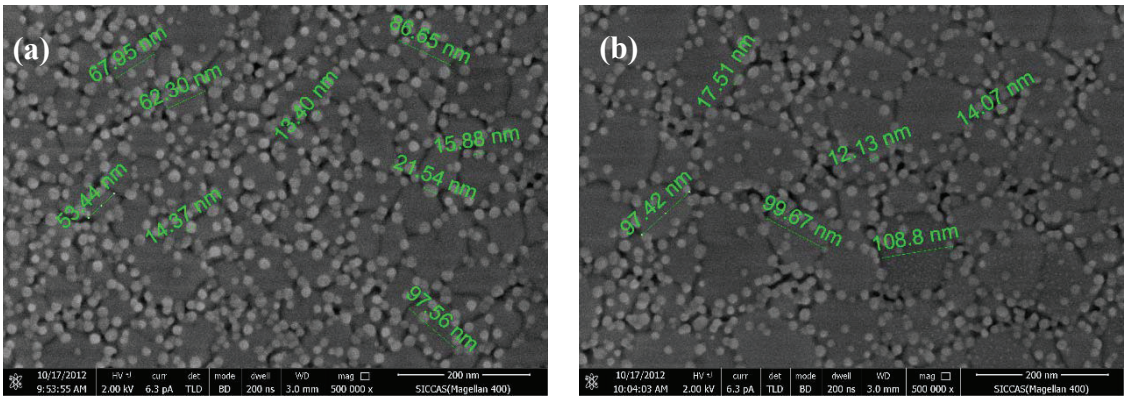

Figure 5.20 SEM surface image of PLZT films of (a) 150 nm and (b) 250 nm

Figure 5.20 shows the SEM surface morphology of PLZT films image with 150 nm (a) and 250 nm-thick (b). We can see that they have similar grain size of about 80 nm in diameter.

Figure 5.21 shows the dependence of polarization versus electric field (P-E) curves on thickness in film capacitors with two different top electrodes ($LaNiO_3$ and Pt) and identical $LaNiO_3$ bottom electrodes. It is shown that using Pt as the top electrode, the quality of the hysteresis loops depends strongly on film thickness. Although with some remanent polarization, the films with thickness equal to about 250 nm demonstrate evident double switching loops (Figure 5.21(a)). However, the hysteresis loops of films with thickness equal to or less than about 150 nm (Figures 5.21(c) and 5.21(e)) show ferroelectric-like switching loops indicating the smearing of field-induced phase transition. The films with thickness of 100 nm demonstrate a saturation polarization (P_s) of ~ 30 $\mu C/cm^2$ and a large remanent polarization (P_r) of ~5 $\mu C/cm^2$. In contrast, the thickness dependence in films using $LaNiO_3$ as top electrode is lower: the films of about

250-nm thickness demonstrate zero remanent polarization (Figure 5.21(b)) and when the thickness decreases to 150 nm, although with some remanent polarization, the hysteresis loop maintains its square shape (Figure 5.21(d)). Even for films as thin as about 100 nm, the P-E curve changes to a more diffused one with a larger P_s of ~37 μC/cm^2 and a smaller P_r of ~2 μC/cm^2 (Figure 5.21(f)) compared to that of films using Pt top electrodes. The results unequivocally indicate that the size effect of antiferroelectric films can be dramatically improved by using oxide metal $LaNiO_3$ as top electrode.

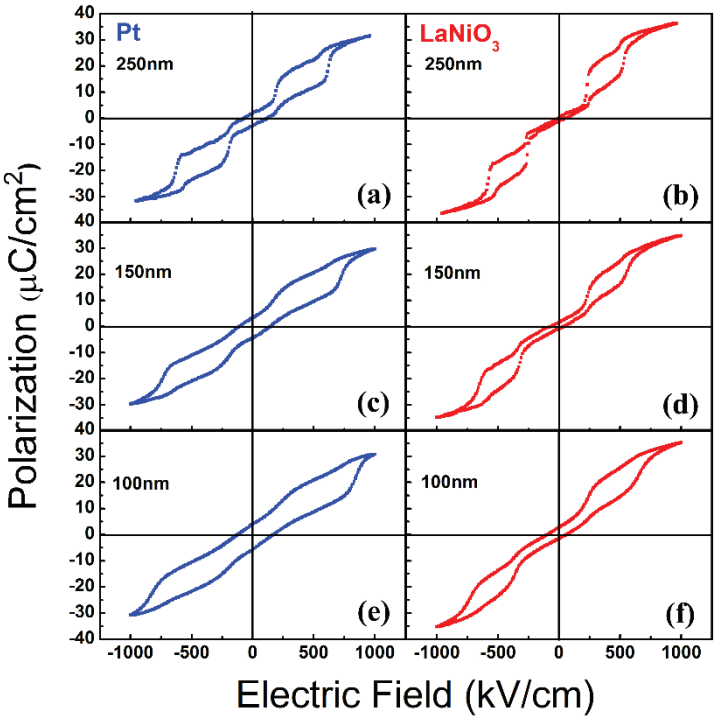

Figure 5.21 The hysteresis loops of PLZT thin films with various thickness: (a),(c), and (e) P-E loops of PLZT thin films using Pt as top electrode; (b), (d),and (f) P-E loops of PLZT thin films using $LaNiO_3$ as top electrode (measured at room temperature with 1 kHz)

To clarify the effect of top electrode, we plot the curve of P_r with thickness (Fig. 5.22). We can see that with the decreasing of thickness, the P_r increases

slowly. However, the P_r of films with LNO top electrodes is always lower than that of films with Pt top electrodes.

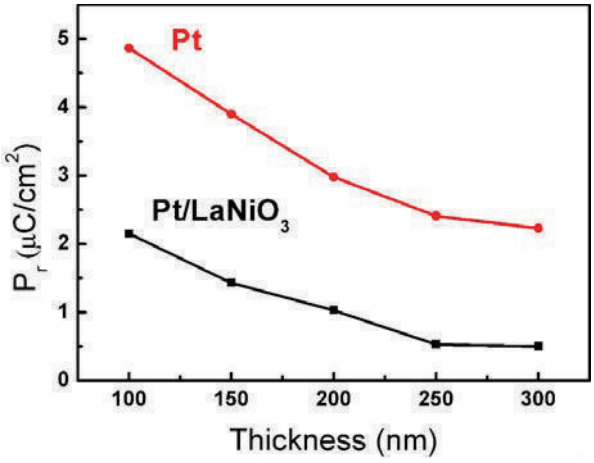

Figure 5.22 Relation of P_r with thickness of PLZT films using different top electrodes

Figure 5.23 shows the P-E loops of 100-nm-thick films with different top electrodes. Compared to ferroelectric thin films, the study of size effect in antiferroelectric thin films is still very limited and the mechanisms underlying it remain contentious. We believe in our cases the size effect is related to the extrinsic contribution of electrode/film interfacial layers. The interfacial layer at the electrode/film interface has been investigated extensively and thought to be the dominant factor for the thickness-dependent properties in ferroelectric films.[11,12] It has been proposed that a non-ferroelectric layer is formed at the Pt electrode/ferroelectric interface, which results in a lower P_s and P_r. Similarly, we can assume that a non-antiferroelectric layer with a relatively low value of spontaneous polarization is formed between the antiferroelectric and the electrode. Hence, at high electric field, the antiferroelectric phases are switched to the ferroelectric phases and the interfacial layer will decrease the P_s. Further, at low

electric field, when ferroelectric phases transform back to the AFE phases, the non-antiferroelectric layer at the PLZT/electrode interface remains some polarization and increases the P_r. In general, the interface layer of films using oxide metals as contact is usually thinner than that of films with elemental metal electrodes because of their structural and chemical compatibility. Therefore, films with $LaNiO_3$ top electrodes give better hysteresis loops with relatively low dependence on thickness.

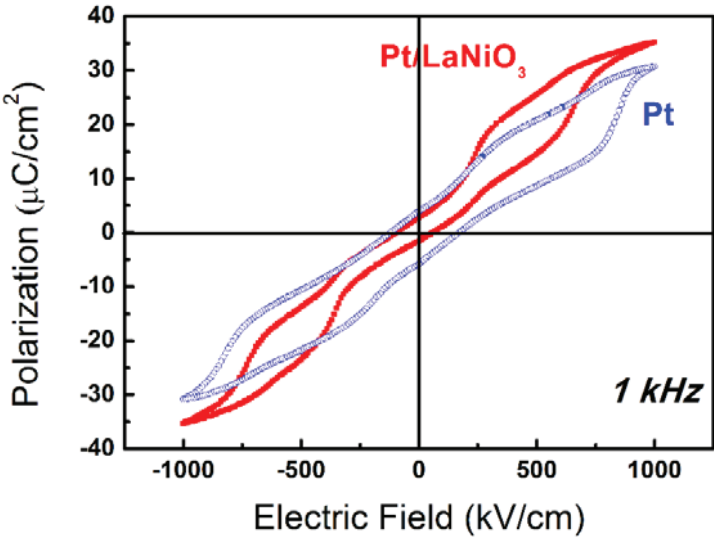

Figure 5.23 Hysteresis loops of PLZT films with Pt and $LaNiO_3$ oxide top electrode

According to the definition of energy storage density by P-E loops, $W = \int E_0 dP$, the energy storage density W, the energy loss density W_{loss} and energy efficiency η ($\eta = W/(W+W_{loss})$) were calculated at different external field. The dependence curves of W on electric field (E_0) observed at 1 kHz of 100-nm-thick films with $LaNiO_3$ and Pt top electrodes shown in Fig. 5.24 and Fig. 5.25 were investigated. Both electrode configurations showed the expected three distinct linear regions indicating the antiferroelectric nature of all samples, which is consistent with the

results that the size effect is extrinsic and induced by interfacial layer. It is particularly noteworthy that these films have very high dielectric strength (>1.5 MV/cm), possibly due to their uniform and pore-free microstructures. It is found that the *W* is equal to ~14.8 J/cm^3 and ~10.2 J/cm^3 at applied field of 1 MV/cm, and ~19.0 J/cm^3 and ~13.6 J/cm^3 at 1.5 MV/cm for films with $LaNiO_3$ and Pt top electrodes respectively. These results are larger than those reported previously for PLZT films (12.4 J/cm^3 at about 1.1 MV/cm, breakdown at higher E_0. Moreover, the energy efficiency of films with $LaNiO_3$ top electrodes as shown in Fig.5.25 is elevated greatly. For example, the η for PLZT films with $LaNiO_3$ top electrodes at 1 MV/cm is ~66% and the corresponding value for films with Pt top electrodes is ~55%. Hence, using $LaNiO_3$ as top electrode, an enhancement of 4.6 J/cm^3 in the energy storage density and an increase of 11% in the energy efficiency are realized in contrast to Pt top electrodes.

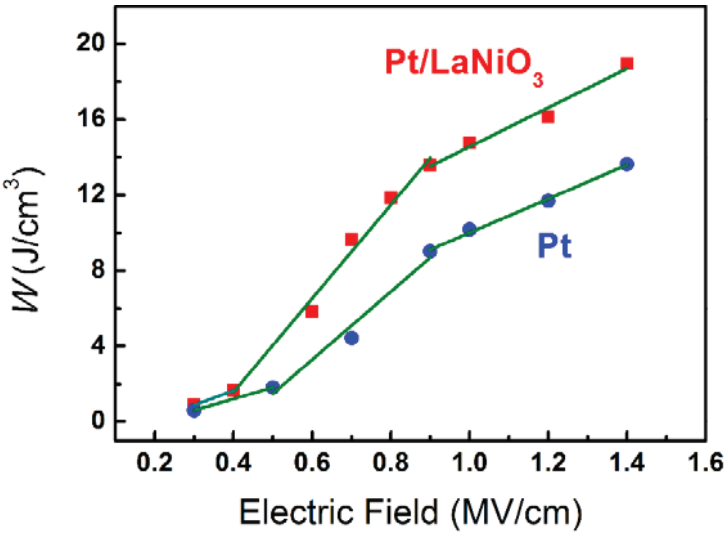

Figure 5.24 Dependence of energy density W on field amplitude E_0 at 1 kHz in 100-nm-thick PLZT films with Pt and $LaNiO_3$ top electrodes

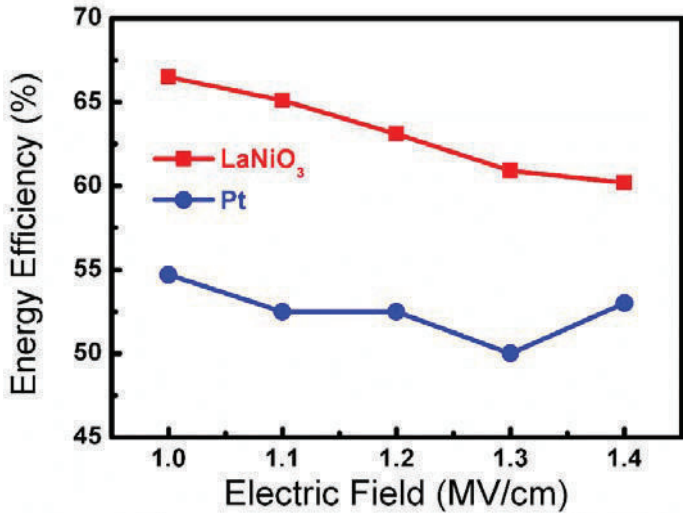

Figure 5.25 Dependence of energy efficiency on field amplitude E_0 at 1 kHz in 100-nm-thick PLZT films with Pt and $LaNiO_3$ top electrodes

Focusing now on 250-nm-thick samples, we have investigated the hysteresis loops and the energy storage properties in a broad temperature range. Figure 5.26 shows that the double hysteresis behavior becomes less pronounced with increasing temperature and eventually transforms into a ferroelectric hysteresis loop at 423K, corresponding to the thermo-induced antiferroelectric to ferroelectric transition.

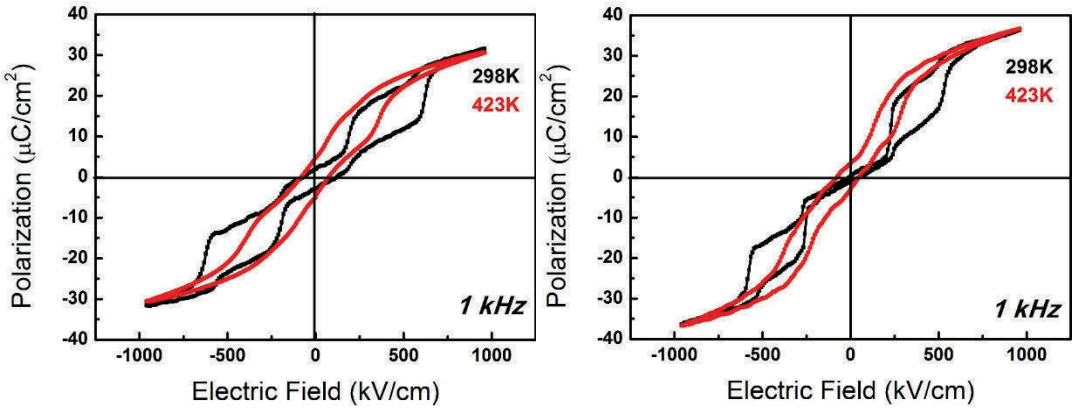

Figure 5.26 The hysteresis loops of 250-nm thick PLZT films measured at different temperatures with (a) Pt top electrodes and (b) $LaNiO_3$ top electrodes

From these measurements, we can obtain the temperature dependence of *W* (Figure 5.27(a)). We see that the *W* of films with either top electrodes decreases monotonically and constantly as the temperature increases from 298K up to 423K, which may imply that the AFE-FE phase transition is processing in a rather broad temperature region. In order to have a closer look on the comparison of the films with different top electrodes, we divide *W* by *W* at 298K (W_{RT}) and extract the temperature dependence of normalized W/W_{RT} (*W'*) *W* (Figure 5.27(b)). We see that the *W'* can be described by a linear relationship of the form $W' = \alpha T$ (+m). We observe two scaling regimes with different α. The presence of two scaling regimes is likely due to the presence of two mechanisms that influence the *W*. At relative low temperature, the thermally activated AFE-FE phase transition has not happened and for films with Pt electrodes, the deterioration of Pt/film interface controls the decrease of *W* and at 323K the *W* decreases ~12% of W_{RT}. In contrast, by using $LaNiO_3$ top electrodes, the excellent high-temperature stability enables the *W* of the films basically unchanged up to 323K. At high temperature, the phase transition is activated and the *W* decreases of both electrode configurations. Further, the temperature dependence of *W'* shows that the α is roughly the same for films with either top electrode materials at temperature higher than 363K, which may imply the effect of phase transition has dominated the decrease of *W*. The temperature-dependence characterization gives useful insights into the intrinsic and extrinsic contributions to the energy storage properties of PLZT AFE

thin films and shows that the high-temperature energy storage properties can be greatly improved with the choice of oxide electrodes.

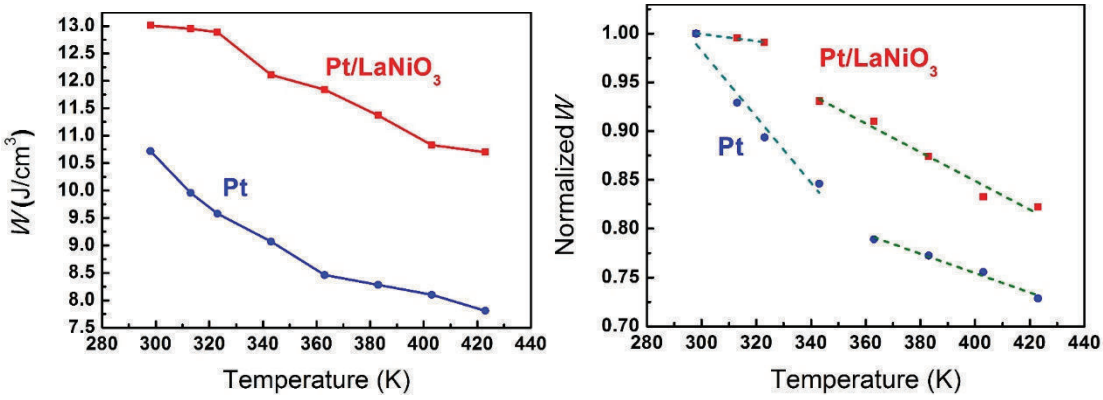

Figure 5.27 (a) The temperature dependence of W measured at 1 MV/cm in films with Pt and $LaNiO_3$ top electrodes. (b) The temperature dependence of normalized W/W_{RT} calculated from (c) (measured at 1 kHz)

5.4.4 Conclusion

We find that by using oxide $LaNiO_3$ as top electrode, the size effect of antiferroelectric films has been greatly improved compared to that of films using traditional metal top electrode, such as Pt. The results suggest that a non-antiferroelectric layer may form at the interface between the PLZT film and the Pt top electrode, which is responsible for the inferior double hysteresis loops of films. However, the interfacial layer can be reduced by using oxide metals as contact. As a result, *W* as well as the energy efficiency of films is enhanced using $LaNiO_3$ as top electrode. In addition, the films are more capable of providing high *W* over a wide temperature regime above room temperature by choosing $LaNiO_3$

as top electrode, due to its structural and chemical compatibility with the PLZT films.

CHAPTER 6

Preparation and energy storage of PZ Films

Chapter 6 Preparation and energy storage properties of $PbZrO_3$ films

Dielectric materials that provide the capability of high-performance energy storage are of great importance for the power electronics in a wide range of technological applications. Among various dielectric materials, antiferroelectrics (AFEs) are promising candidates for dielectrics in high energy density electrical capacitors due to the field-induced phase transition into the ferroelectric state accompanied by large charge storage. In general, the recoverable energy density (W) can be calculated by the integral $W=\int EdD$, where E is the electric field and D is the electric displacement or charge density. Therefore, antiferroelectric thin films can develop greatly enhanced energy density compared with their bulk counterparts because they typically have higher dielectric strength and the electric displacement tends to saturate at higher electric field. To further enhance the energy storage property of AFE films, many efforts have been made including modification of film composition, PbO content excess, and using oxide top electrodes[16,117-119]. However, it appears that no report on strain dependency of AFE films on different substrates has been published. In contrast, for FE materials, especially films, there are many researches on effect of strains[94,114,120,121].

6.1 Properties of $PbZrO_3$ films on different substrates

6.1.1 Introduction

As we know, the substrates can have huge effect on films. For example, the mismatch of lattice parameter between the film and substrate can lead to a strain

in films, and change the properties of films in many aspects. [122-124] However, investigation of effect of strain on AFE films is relatively rare [63]. Hence, we choose different substrates to create different states of strain in films, to know how the strain will influence the properties of films.

6.1.2 Experiments

We use $PbZrO_3$ (PZ) powder target with 15% Pb excess for sputtering. The fabrication process can be found in Chapter 3. The deposition parameters are shown in table 3.1. Before the deposition of PZ, LNO bottom electrode is deposited and annealed at 700 ^oC for 1 h. The parameters can be found in table 6.1.

Table 6.1 Details of the LNO films deposition conditions

Condition	parameter
Vacuum (mbar)	$<3\times10^{-5}$
Pressure of deposition (mbar)	1×10^{-2}
Power density (W/cm^2)	1.52
Gas	Ar
Deposition rate (nm/min)	~3.5
Target	$LaNiO_3$ ceramic
Temperature (^oC)	450

6.1.3 Results and discussion

Figure 6.1 shows the XRD results of PZ films on $SrTiO_3$, Al_2O_3 and SiO_2/Si substrates. LNO was chosen as bottom electrode. As we can see from the map, all

LNO films are highly (100)-oriented. Hence, the PZ films follow the preferred orientation of LNO films.

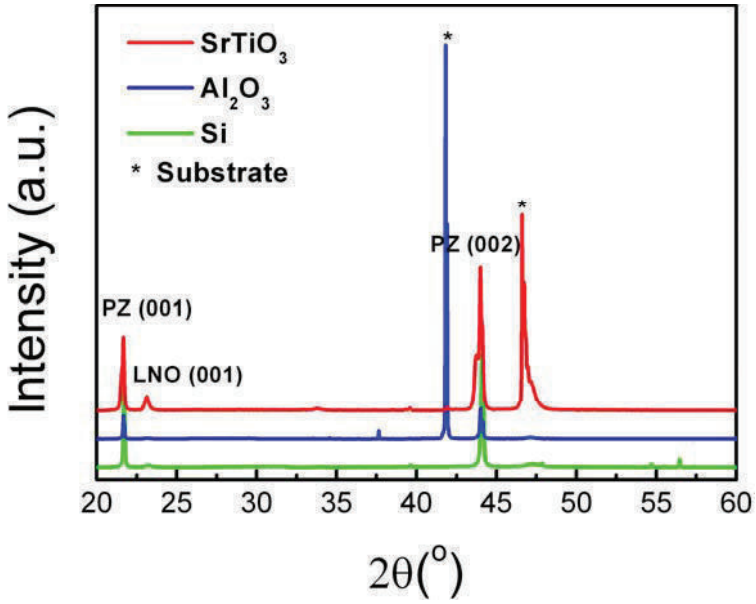

Figure 6.1 Room temperature XRD θ-2θ of PZ films with LNO bottom electrodes on $SrTiO_3$, Al_2O_3 and SiO_2/Si, respectively

Based on the peak of PZ diffraction, we can calculate the out-of-plane lattice parameter. To look closer about the moving of the peak, Fig. 6.2 shows the peaks from 20° and 23° and from 42° and 46°. We can see from the map, the peak of PZ film on SiO_2/Si shift to right position obviously, compared with those of PZ films on $SrTiO_3$ and Al_2O_3. This indicates that films on SiO_2/Si receives more tensile stress.

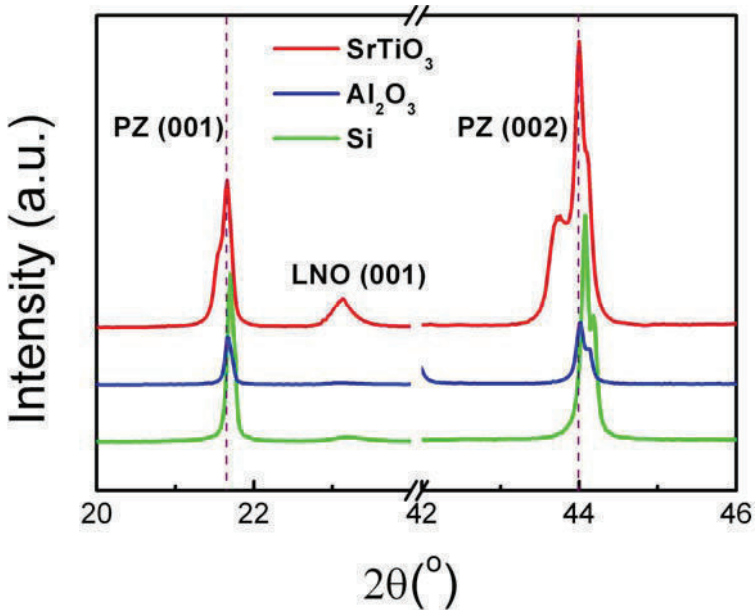

Figure 6.2 Room temperature XRD θ-2θ of PZ films with LNO bottom electrodes on $SrTiO_3$, Al_2O_3 and SiO_2/Si respectively

Because all the films are polycrystalline films, hence the epitaxial strain can be neglected. Similarly, all films are prepared under the same deposition parameters, hence the strains come from defects and phase transition should be same. Therefore, the cause that lead to the difference of strain state of our films should be the different thermal coefficients. We know that the thermal coefficient of SiO_2/Si is from 2.6 to 4 ppm/K,[70] for Al_2O_3 is about 7.5 ppm/K[29] and for $SrTiO_3$ is about 11 ppm/K[29] and for PZ is about 8 ppm/K[41]. Hence, PZ films on SiO_2/Si substrates should receive thermal tensile stress, while films on Al_2O_3 and $SrTiO_3$ should receive thermal compressive stress.

Figure 6.3 shows the relationship of the d-spacing of (002) with the thermal coefficient of substrate. As we can see from the figure, the d-spacing increases with the thermal coefficient, indicating that the films suffer more and more in-

plane compressive strain. This is consistent with our conclusion from the analysis of thermal coefficients.

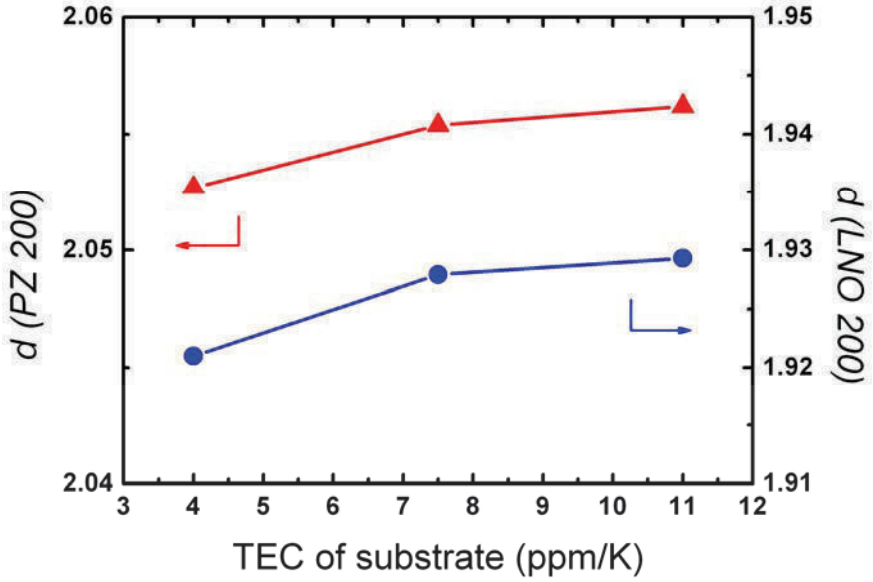

Figure 6.3 Distant of (200) lattice plane of PZ and LNO films on $SrTiO_3$, Al_2O_3 and SiO_2/Si respectively

Figure 6.4 shows the P-E loops of PZ films on different substrates. As we can see from the map, films on Al_2O_3 and $SrTiO_3$ substrates show a more diffused phase transition compared with the films on SiO_2/Si substrates. This means that we can adjust the properties of PZ films by choosing different substrates.

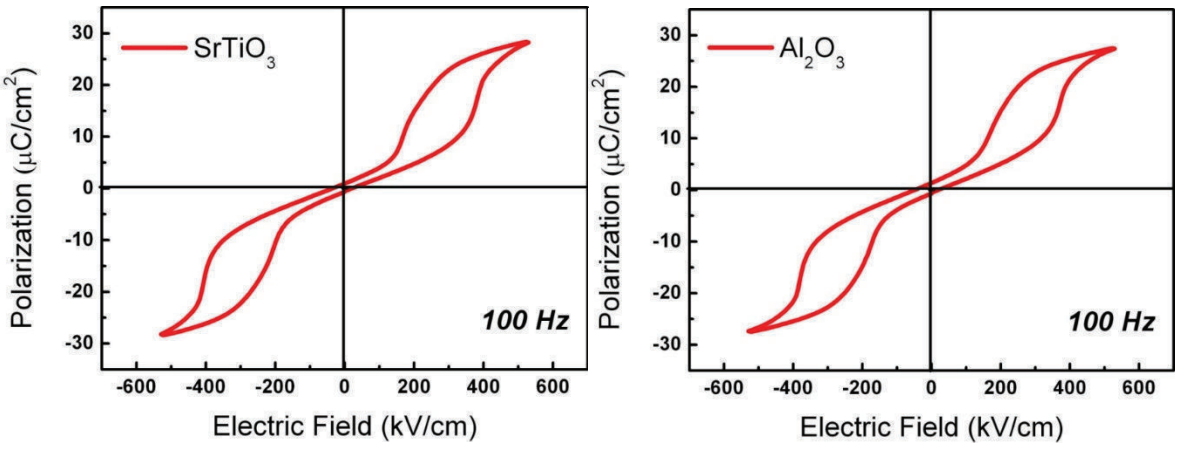

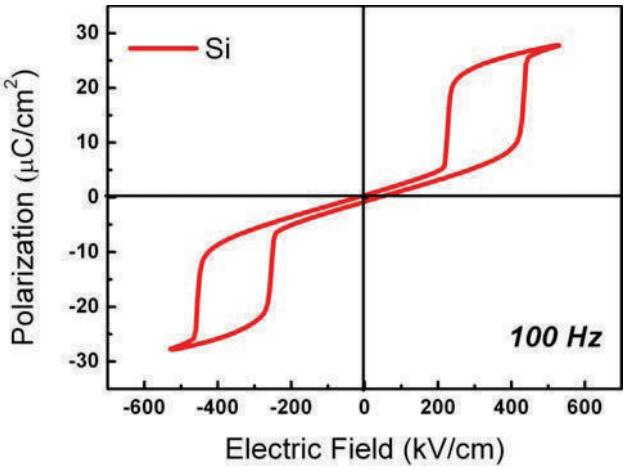

Figure 6.4 Hysteresis loops of PZ films measured at 100 Hz

Figure 6.5 compares the Ps, phase transition field E_F and W of PZ films on various substrates. We find that Ps increases with the increasing of thermal coefficient, however E_F decreases with the increasing of thermal coefficient. Combining these influences, we find that the W of film decreases with the increasing of thermal coefficient.

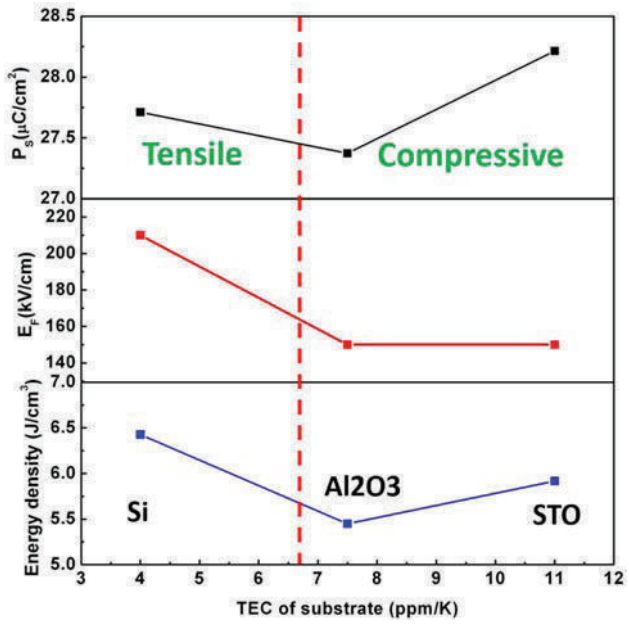

Figure 6.5 The dependence of P_s, E_F and energy density of PZ films on thermal expansion coefficients of substrates

6.1.4 Conclusion

We deposited PZ films on SiO_2/Si, Al_2O_3 and $SrTiO_3$ substrates. We found all PZ films are highly (100)-oriented. Based on the calculation of thermal coefficient and peak position of PZ, we found PZ on SiO_2/Si received tensile stress while films on Al_2O_3 and $SrTiO_3$ received compressive stress. The P-E loops show that Ps increases, while E_F and W decrease with the increasing of thermal coefficient.

6.2 Effect of residual stress on energy storage property in $PbZrO_3$ antiferroelectric thin films with different orientations

6.2.1 Introduction

In the last chapter we investigated the influence of strain state on the properties of PZ films. We have found the relation between W and the changing of substrate materials for PZ films. In practical applications, PZ films might have better performance with another preferred orientation [78,126]. Hence, in the following we investigated the properties of PZ films on different substrates.

6.2.2 Experiments

The method of preparing PZ films is the same as that of chapter 6.1. However, we prepared LNO bottom electrodes with different orientations. $LaNiO_3$ (LNO) thin films were deposited by RF magnetron sputtering. A 3-in.-diameter stoichiometric target for LNO thin films was made by using a conventional mixing-oxides method, which included calcining La_2O_3 and Ni_2O_3 powders (both of 99.99% purity).The sintering was carried out at 1180 ^oC for 2h. The as-deposited films were annealed under air atmosphere at 700^oC for 1 hour. The sputtering parameters and texture conditions of LNO films are concluded in Table.Ⅰ.

Table.Ⅰ Summary of sputtering parameters and texture condition of $LaNiO_3$ films

Sample No.	Power density (W/cm^2)	Working pressure (Pa)	Atmosphere $O_2/(Ar+O_2)$ (%)	Substrate Type	Preferred orientation	Epitaxial Condition
S1	1.8	1	0	$SrTiO_3$	(100)	uniaxially textured
S2	1.8	1	0	Si	(110)	uniaxially textured
S3	1.8	1	20	$SrTiO_3$	(100)	Fully epitaxial
S4	1.8	1	20	Si	(100)	uniaxially textured

6.2.3 Results and discussions

Figure 6.6 shows the schematic diagram of our samples. They were PZ films with (101) preferred orientation, named as $PbZrO_3$/LNO/$SrTiO_3$, $PbZrO_3$/LNO/SiO_2/Si. The other two kinds of samples are (100)-oriented on $SrTiO_3$ and SiO_2/Si substrates.

Figure 6.6 Schematic illustrations of four sample variables studied in this work: PZ (110)/STO, PZ(110)/Si, PZ(001)/STO, PZ(001)/Si

Figure 6.7 shows the XRD patterns of LNO bottom electrodes. It can be seen that S1, S3 and S4 show high (100) orientation texture whereas S2 shows preferential (110) orientation.

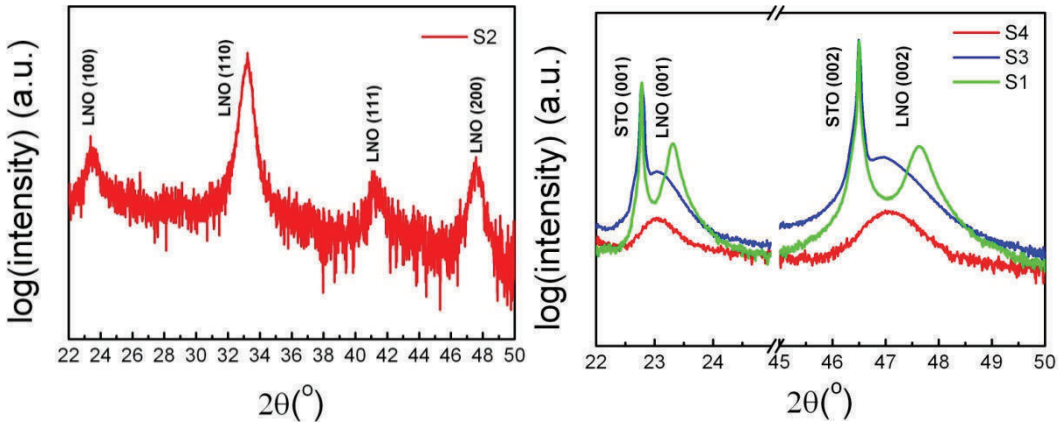

Figure 6.7 θ-2θ XRD patterns of LNO films on different substrates

Focusing on S3, Fig. 6.8(a) shows the rocking curve of the LNO (001) peak with a full width at half maximum (FWHM) value, Δω, of 2.1°. Fig. 6.8(b) shows the Φ scan of the $LaNiO_3$ (110) peak with a four-fold in-plane symmetry, which indicates $LaNiO_3$ is highly biaxially textured.

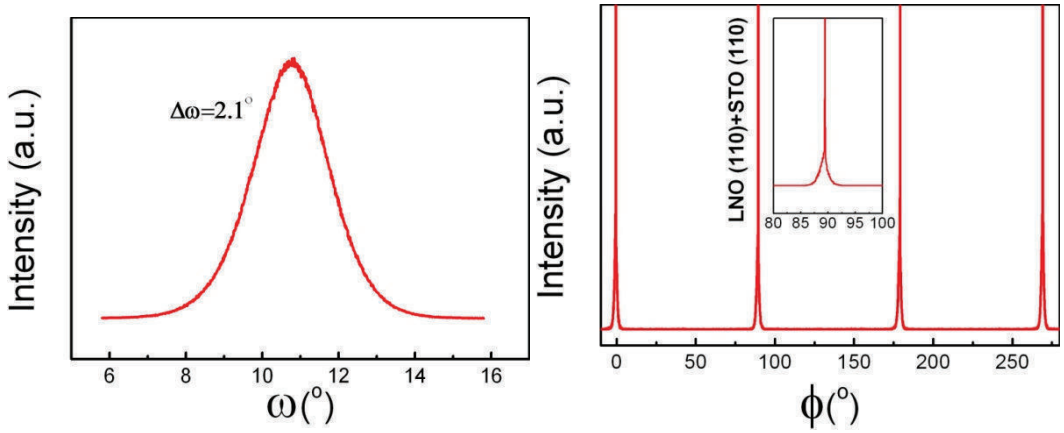

Figure 6.8 (a) ω rocking curve on S3 (001) peak, (b) Φ scan of S3 (110) peak

The rocking curve and Φ scan on S1, S2 and S4 show that all other LNO films are uniaxially textured with no in-plane texture. Fig. 6.9 shows the Φ scan of the (110) peak of S1. The Φ scan patterns of S2 and S4 (not shown here) are similar.

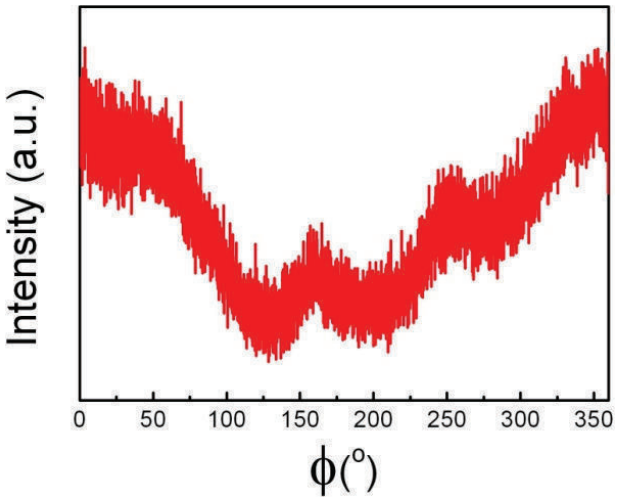

Figure 6.9 Φ scan of S1 (110) peak

Figure 6.10 illustrates the Φ-scan patterns of PZ (101) and $SrTiO_3$ (101) planes. The patterns show a fourfold symmetry which indicates the PZ film epitaxially grows on the $LaNiO_3$ buffered $SrTiO_3$ substrate.

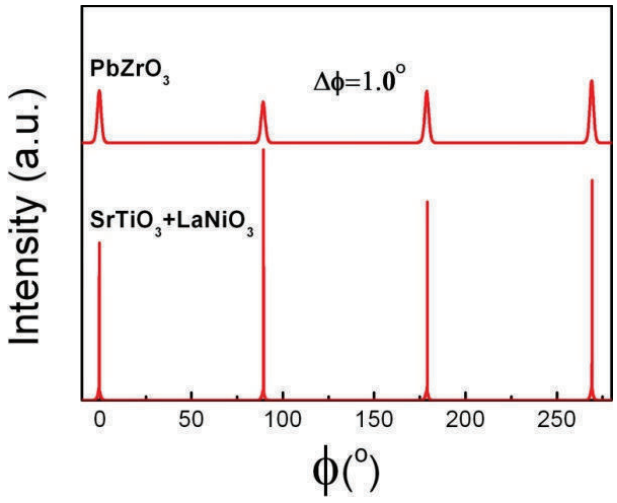

Figure 6.10 Φ scan of PZ (101) peak

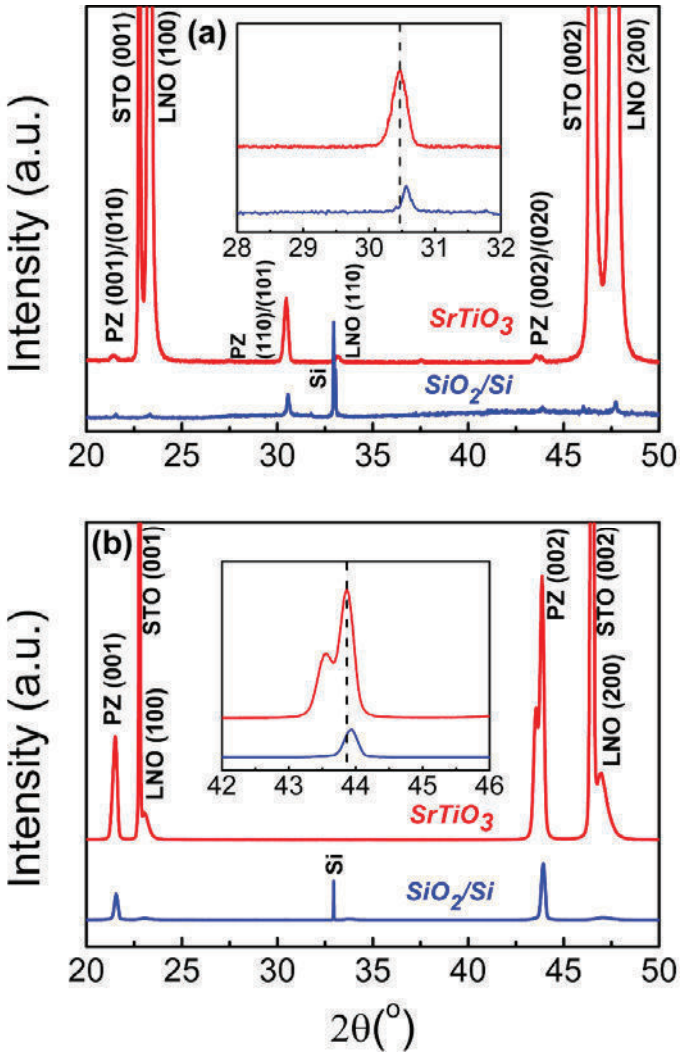

Figure 6.11 Room temperature XRD θ-2θ of PZ films grown on (a) LNO (0% oxygen partial pressure) buffered (001) $SrTiO_3$ and SiO_2/Si, (b) LNO (20% oxygen partial pressure) buffered (001) $SrTiO_3$ and SiO_2/Si

Figure 6.11 shows X-ray diffraction (XRD, CuK_α radiation) patterns of PZ films deposited on LNO-buffered (001) $SrTiO_3$ and SiO_2/Si substrates. It should be noted that PZ possesses an orthorhombic structure below curie temperature (~230 °C) in which the orthorhombic cell is a multiple unit cell and contains eight primitive cells which have a tetragonal structure (a_0=~4.15 Å, b_0=~4.15 Å, c_0=~4.10 Å). Hence, for convenience all the peaks of PZ films are indexed based

on the tetragonal structure. In Fig. 6.11(a), it is shown that LNO deposited on $SrTiO_3$ at 0% oxygen partial pressure is highly (100)-oriented while on SiO_2/Si the figure shows a (110)-preferred orientation. However, PZ films on both substrates have (110)/(101) preferred orientation and the reflections from the LNO electrodes indicate an out-of-plane lattice constant of 3.81 Å. The fact that PZ doesn't follow the (100) orientation of LNO on $SrTiO_3$ is maybe due to the large lattice misfit between LNO (3.81 Å) and PZ (~4.14 Å as a pseudo-cubic), which makes it difficult to facilitate grain-on-grain growth. In contrast, Fig. 6.11(b) shows LNO films deposited at 20% oxygen partial pressure are all highly (100)-oriented and yield a lattice constant of 3.87 Å, which indicates smaller lattice misfit with the overlaying PZ film. Consequently, PZ films follow the (100) orientation of LNO and show highly (001)-oriented fiber texture on both substrates. The out-of-plane c parameter of films with (001) orientation is 4.107 Å on SiO_2/Si substrates (calculated from the (002) peak from XRD patterns) and as on $SrTiO_3$ substrates, the (002) peak is more split, with a lattice parameter about 4.113 Å from the dominant peak, indicating the c_0 axis of the PZ unit cell lies perpendicular to the film plane and the a_0 and b_0 axes lie in plane. In addition, the rocking curve and Φ-scan confirm that PZ with LNO electrode deposited at 20% O_2 partial pressure on $SrTiO_3$ are epitaxially grown and the other PZ films are uniaxially textured. Moreover, as we can see from the insets of Fig. 6.11, the peaks corresponding to PZ shift towards lower 2θ angle as the substrates change from Si to $SrTiO_3$, indicating an increase in the out-of-plane lattice parameter, which

means films on $SrTiO_3$ receive a higher compressive stress compared to films on Si substrate.

In general, stress in a thin film can come from various sources including (1) intrinsic stress induced from a particular growth process, (2) transformation stress due to structural phase transition, (3) lattice mismatch stress due to epitaxial growth and (4) thermal stress due to thermal expansion mismatch. Because all PZ films are deposited using the same parameters and the phase structures are essentially similar, the intrinsic and transformation stress can be treated as the same for all samples. Considering the thermal stress, the thermal expansion coefficients (TECs) of $SrTiO_3$ and SiO_2/Si substrates are 11.0[29] and 2.6[70] ppm/K, respectively, and assuming PZ films have a same value of TEC as PZ bulk ceramic (8.0 [41] ppm/K), thus films on $SrTiO_3$ and SiO_2/Si are under compressive and tensile stress, respectively. As for lattice misfit stress, in view of only PZ films on LNO (20% of oxygen partial pressure) buffered $SrTiO_3$ were epitaxially grown and lattice parameter of LNO (3.87 Å) is smaller than that of PZ, it seems that the film will receive additional epitaxial compressive stress. However, there are also some reports argue that in epitaxial $Pb(Zr_{1-x}Ti_x)O_3$ (PZT) films much thicker than the critical thickness (>80 nm), the lattice strain is completely relaxed.[127,128]

Polarization versus electric field hysteresis loops were measured on all four samples at a series of temperatures. Figures 6.12(a) and 6.12(b) show the loops of PZ films at 30 and 110 ^oC with a peak field of 700 kV/cm. It can be seen that with the temperature increasing, both critical electric fields E_F and E_A shift to lower

value leading to a decrease in W. The effect of residual stress can be verified by the comparison of hysteresis loops of films on different substrates at the same temperature. It can be concluded that with the same orientation, films on $SrTiO_3$ appear to have slightly higher maximum polarization compared to films on SiO_2/Si.

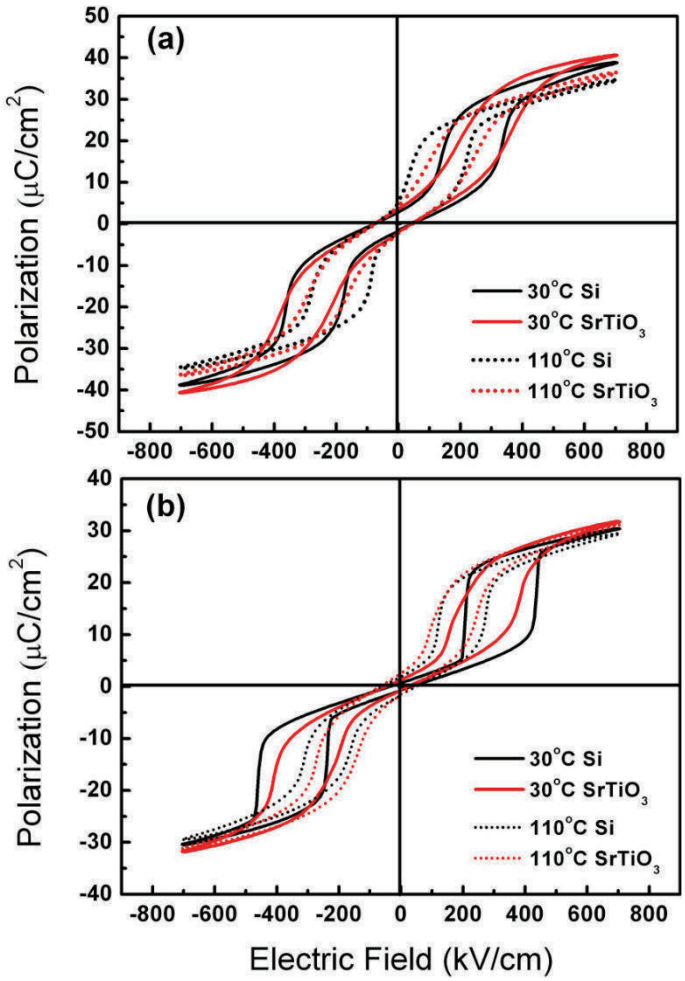

Figure 6.12 Polarization versus electric field hysteresis loops of (a) (110)/(101)-oriented PZ films and (b) (001)-oriented PZ films on SiO_2/Si and $SrTiO_3$ at 30 and 110 °C (measured at 100 Hz)

However, the relationships of E_F and E_A with thermal stress vary substantially as the orientations of films change. For PZ samples with (110)/(101) preferred orientation, the E_F and E_A of the sample on $SrTiO_3$ are slightly higher than that of

the sample on SiO_2/Si. In contrast, when the orientation of PZ films changes to (001), our observation shows an opposite trend that the films on $SrTiO_3$ display lower E_F and E_A compared to films on SiO_2/Si. Furthermore, the phase transitions (both forward and reverse ones) appear to be more abrupt in sample on SiO_2/Si substrate.

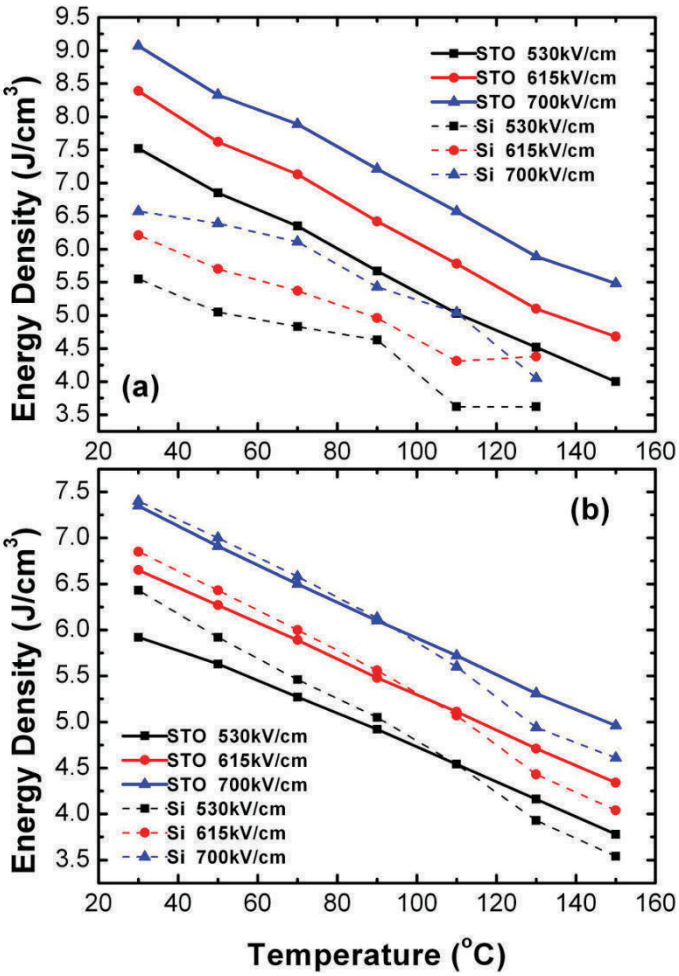

Figure 6.13 The temperature dependence of W for (a) (110)/(101)-oriented PZ films and (b) (001)-oriented PZ films on SiO_2/Si and $SrTiO_3$ measured at 530, 615, and 700 kV/cm, respectively

From the hysteresis loops data at different electric fields and temperatures, energy storage density can be further extracted (Fig. 6.13). For samples with (110)/(101) orientation, films on $SrTiO_3$ substrate exhibit higher energy density

in whole temperature range compared to films on SiO_2/Si, which means the compressive stresses enhance energy density of PZ films. For example, at 30°C, W at 700kV/cm is ~9.0 J/cm^3 in films on $SrTiO_3$ and ~6.5 J/cm^3 in films on SiO_2/Si, corresponding to a 38% increase. In contrast, for samples with (001) orientation, slightly higher energy density is achieved in films on SiO_2/Si compared to films on $SrTiO_3$ at room temperature, especially at relatively low electric field. For instance at 30 °C, W is ~6 J/cm^3 in films on $SrTiO_3$ and ~6.5J/cm^3 in films on SiO_2/Si at 530kV/cm. However, as the temperature increases, the energy density of films on SiO_2/Si decreases a little more rapidly and hence becomes smaller than that of films on $SrTiO_3$ at temperatures above 110 °C.

The fact that the PZ films with (110)/(101) orientation give larger energy density on $SrTiO_3$, while films with (001) orientation obtain better energy storage property on SiO_2/Si, can be explained by a consideration of the different constrain states in films with different orientations. We draw the schematic diagram of the primitive cells in AFE and FE phases with different orientations (Figure 6.14). The polar direction of the antiparallel dipoles are along the [110] direction of the tetragonal primitive cell.[129] When changed to the FE phase, the tetragonal primitive cell becomes rhombohedral with the polar directions along the [111] direction. The lattice angle of the unit cell of the FE rhombohedral phase α_{Rh} is very close to 90° (89.8° or 89.95°).[130] The lattice parameter a_{Rh} of FE rhombohedral phase is a little smaller than a_{tet} of the AFE tetragonal primitive cell,

but obviously larger than c_{tet}. Fig. 6.14(a) shows the primitive cells with (101) orientation in AFE and FE phases. The situation of primitive cells with (110) orientation would be similar. It can be seen that the films will expand in the plane parallel to the film surface after being switched to the FE phase. Hence, the residual compressive stress will make the films prone to the AFE phase, thus shifts the E_F and E_A to higher value. In contrast, if the films are (001)-oriented, as shown in Fig. 6.14(b), because a_{Rh} is a little smaller than a_{tet}, the films will contract along the in-plane direction and hence it is not compressive stress but tensile stress that will stabilize the AFE phase, leading to an increase in E_F and E_A of samples on SiO_2/Si in comparison to samples on $SrTiO_3$.

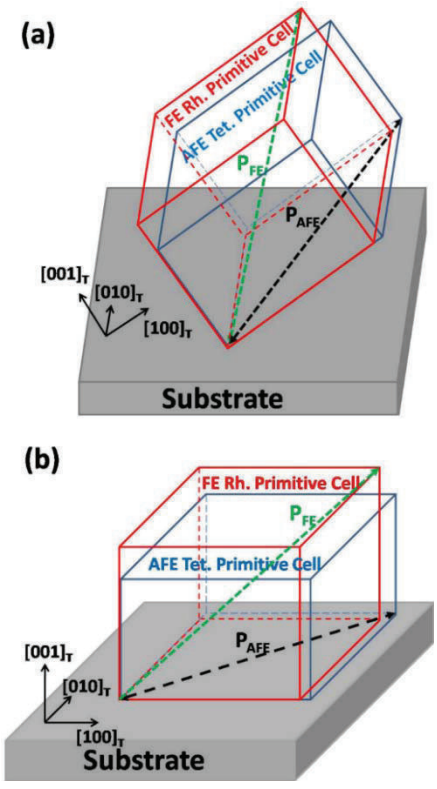

Figure 6.14 Schematic diagram of the primitive cells with (a) (101) orientation and (b) (001) orientation in AFE and FE phases. The primitive cell is tetragonal (Tet.) structure in AFE phase and rhombohedral (Rh.) structure in FE phase

6.2.4 Conclusion

In summary, we have grown (110)/(101)- and (001)-oriented PZ films on both LNO buffered $SrTiO_3$ and SiO_2/Si substrates. It is observed that the critical electric fields E_F and E_A of films with (110)/(101) orientation increase as the substrate change from SiO_2/Si to $SrTiO_3$ substrates, which lead to a higher energy density in films on $SrTiO_3$ substrate. However, for films with (001) orientation, the E_F and E_A decrease in films on $SrTiO_3$ substrate, which results in a higher energy density in films on SiO_2/Si substrate. These results demonstrate that the orientation of PZ films may heavily influence the relation between the energy density property and the stress field within the PZ films. We conclude that it is closely related to the different constrain states in films with different orientations.

6.3 Enhancement of energy storage in epitaxial $PbZrO_3$ antiferroelectric films using strain engineering

6.3.1 Introduction

The properties of thin films can be distinctly different from the intrinsic properties of the bulk counterpart materials because of the enormous strains existing in thin films when one material is deposited on another. Recently, there has been intense research interest in enhancement of particular properties of certain materials in thin film form, namely strain engineering, by elaborate control of substrates and growth parameters. In ferroelectric and multiferroic epitaxy (systems such as $Ba_{1-x}Sr_xO_3$ and $BiFeO_3$), epitaxial strain has been extensively studied and utilized for enhancement of remanent polarization,[37] increase of Curie temperature,[55] and modifying the phase diagram.[79] In the realm of AFEs, prior work on the effect of compressive strain/stress on bulk AFEs, mainly in $PbZrO_3$ system, has demonstrated a range of novel phenomena such as delayed phase transition,[135] electric field "induced" AFE phase out of FE phase,[136] and enhanced energy density.[137] Hence it is of highly scientific curiosity and technological significance to clarify the effect of strain on AFE films. Unfortunately, understanding the mechanisms of such effect on AFE films is not well established. Earlier research on $Pb(Zr_{1-x-y}Sn_xTi_y)O_3$ (PZST) films showed tensile strains would make the AFE films prone to the FE phase by observing a "slim loop" double hysteresis.[136] However, recent studies argued compressive strain could stabilize a FE phase in $(001)_{pc}$-epitaxial $PbZrO_3$ thin films[137] and multilayer PZST films.[138]

Recent theoretical calculations have suggested that AFE phase stability with strain is also related to the growth orientation of AFE films[131,132] and has been proven by experimental results from highly oriented polycrystalline $PbZrO_3$ films.[133,134] Previous studies, however, have focused on how AFE-FE phase transition and related polarization switching are affected by strain. Very little effort has been directed toward deliberate controlling the strain states and the polarization switching properties. Here, we experimentally demonstrate that the E_F and E_A can be greatly elevated in epitaxial $PbZrO_3$ films by changing a crystallographic orientation of the substrate. In addition, the maximum polarization of these films is also favorably increased hence yielding dramatically enhanced energy storage properties of $PbZrO_3$ films.

6.3.2 Experiments

A series of ~300 nm thick $PbZrO_3$ films were epitaxially grown on (100), (110) and (111) $SrTiO_3$ (STO) substrates at room temperature and 1×10^{-2} mbar of argon by off-axis rf magnetron sputtering. A ~100 nm thick $LaNiO_3$ (LNO) bottom electrode was firstly deposited at 450 ^oC and 1×10^{-2} mbar of 20% oxygen and 80% argon via rf magnetron sputtering. The deposited $PbZrO_3$/LNO/STO heterostructures were annealed under air atmosphere at 625^oC for 30 min to crystallize the films into the perovskite phase. The structure and phase purity of the films were checked using Rigaku SmartLab high resolution X-ray diffractometer (HRXRD) equipped with a 9 kW rotating anode X-ray generator (lambda $K_{\alpha1}$ = 1.54059 nm). In order to make the electric experiments, LNO top

electrode (diameter of ~140 μm) was deposited by RF magnetron sputtering at room temperature through a photolithography process. After, the samples were annealed at 450 ^{o}C for 1h to improve the electric conductivity. The hysteresis loops were performed by aixACCT TF2000FE equipment. The temperature dependence of hysteresis loops was measured in a vacuum of 10^{-5} mbar, increasing the temperature at a ramping rate of 1 K/min.

6.3.3 Results and discussions

Figure 6.15(a) present the θ-2θ X-ray diffraction (XRD) patterns of the $PbZrO_3$ thin films grown on STO substrates with (100), (110) and (111) orientations. All $PbZrO_3$ films followed the orientation of the substrates and grew in single-phase perovskite structure with no detectable impurity or other phases. The peaks are indexed based on the tetragonal structure. Limited by the accuracy of XRD measurements, we can not distinguish the (110) peak from (101) peak of $PbZrO_3$ film grown on STO (110) substrate. However, this will not affect our discussion below and our conclusion can be valid for both orientations. Hence, the samples are denoted as PZ(001)/STO, PZ(110)/STO and PZ(111)/STO. It should be noted that the (002) peak of (001)-oriented thin film demonstrates a weak splitting, which could be induced by formation of a small part of a-domains. The in-plane texturing of $PbZrO_3$ thin films was confirmed by XRD φ scan (Figure 6.15(b)) of $PbZrO_3$ (110), (100), and (100) reflections of the (001), (110), and (111)-oriented thin films, respectively. The peaks from $PbZrO_3$ films match well with the theoretical assumption, indicating epitaxial growth of all the samples.

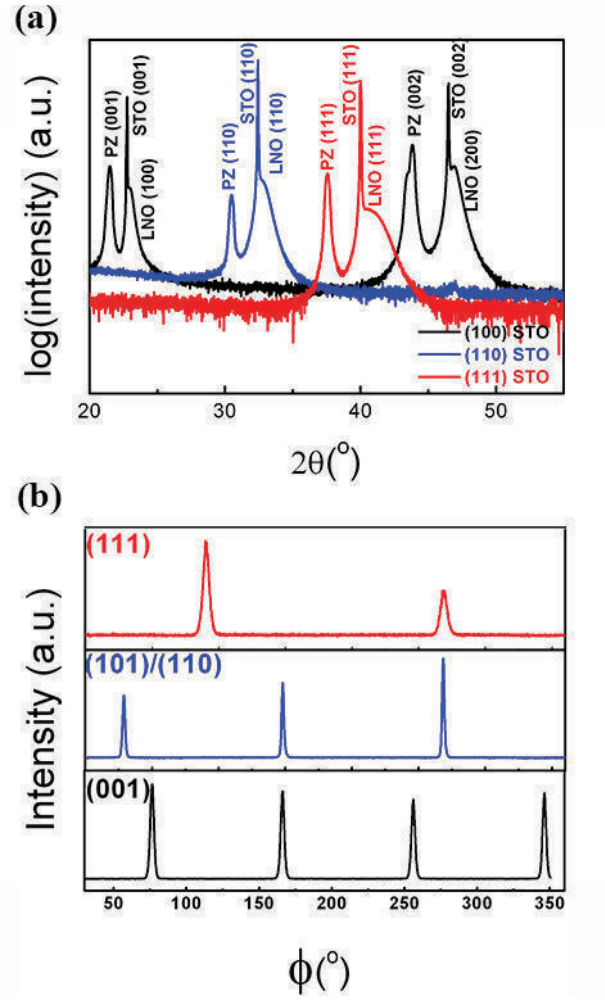

Figure 6.15 (a) θ-2θ X-ray diffraction patterns (XRD) of $PbZrO_3$/LNO/(100)STO,$PbZrO_3$/LNO/(110)STO, and $PbZrO_3$/LNO/(111)STO. (b) Patterns of XRD ϕ scan to confirm the in-plane texture of the $PbZrO_3$ films

The in-plane strain can be calculated by

$$\varepsilon_{ci}=\left(\frac{c-c_0}{c_0}\right)\left(\frac{\upsilon-1}{2\upsilon}\right) \quad (6\text{-}1)$$

where *c* is the (measured) out-of-plane lattice parameter, c_0 refers to the unstrained out-of-plane lattice parameter from bulk material and υ is the Poisson ratio (determined to be 0.3[47] from $(Pb_xLa_{1-x})Zr_{0.52}Ti_{0.48}O_3$). Because the film and corresponding substrate have the same growth orientation, we assume that all

$PbZrO_3$ films are under similar lattice misfit condition and should receive the same magnitude of strain. Given by Equation (6-1), we calculate the in-plane strain ε_{ci} of (001) $PbZrO_3$ film is -0.50%. To further confirm the in-plane compressive strain, the peak of (103) reflection was also measured. (the θ-2θ data are shown in Figure 6.16). Since the (001) peak is already established, the (100) component can be readily extracted. The resulting strain $\varepsilon_{mi}=(a_{film}-a_{bulk})/a_{bulk}$ is -0.55%, which is consistent with the value of strain we calculated from the out-of-plane lattice constant.

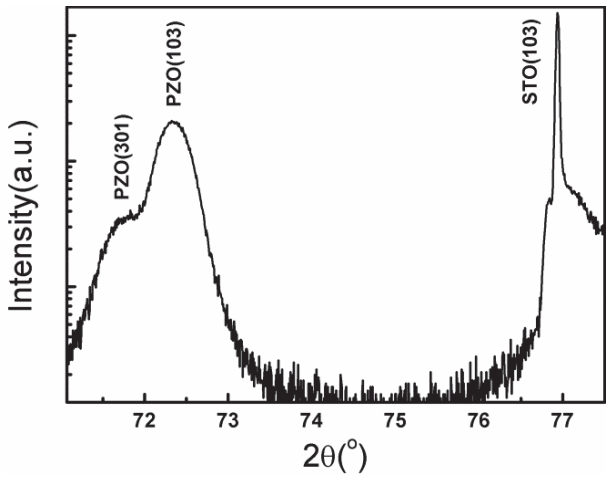

Figure 6.16 X-ray diffraction patterns of (103) scan for (001) $PbZrO_3$ epitaxial film on $SrTiO_3$

Figure 6.17 shows the polarization versus electric field (*P*-E) loops of all the three samples. It can be seen that PZ(001)/STO have a well-developed double hysteresis loops, indicating its AFE nature. Interestingly, PZ(110)/STO and PZ(111)/STO show a mixed antiferroelectric-ferroelectric behavior as suggested by the "triple" hysteresis loop. This phenomenon has recently also been found in

high-quality epitaxial $PbZrO_3$ film with (100) orientation.[67] A plausible explanation is the existence of a FE phase along the c-axis with a relatively low spontaneous polarization. The combination of double loop with single ferroelectric loop leads to the triple loop observed experimentally. Also, PZ(111)/STO has P_{max} slightly higher than PZ(110)/STO, but all possess larger polarization ~45 μC/cm^2 than ~32 μC/cm^2 of PZ(001)/STO, as the polar direction is (111) crystallographic direction of the pseudo-cubic perovskite unit cell. Finally, PZ(110)/STO and PZ(111)/STO illustrate a remarkable increase in the AFE-FE and FE-AFE switching field compared with PZ(001)/STO. The accurate value of E_F and E_A can be obtained from the switching current peak during the *P*-E loops measurements. It is observed that the E_F and E_A are ~500 kV/cm and ~320 kV/cm respectively for PZ(111)/STO and ~380 kV/cm and ~200 kV/cm respectively for PZ(001)/STO, corresponding to a 120 kV/cm increase. It is suggested that there is a small difference in the free energies of AFE and FE phases and the antiparallel dipoles can be flipped and forced to be parallel, corresponding to the electric field-induced AFE-FE phase transition. Thus, the increase of switching field implies the difference of free energies between two phases is enlarged and the AFE phase becomes more stable for PZ(110)/STO and PZ(111)/STO.

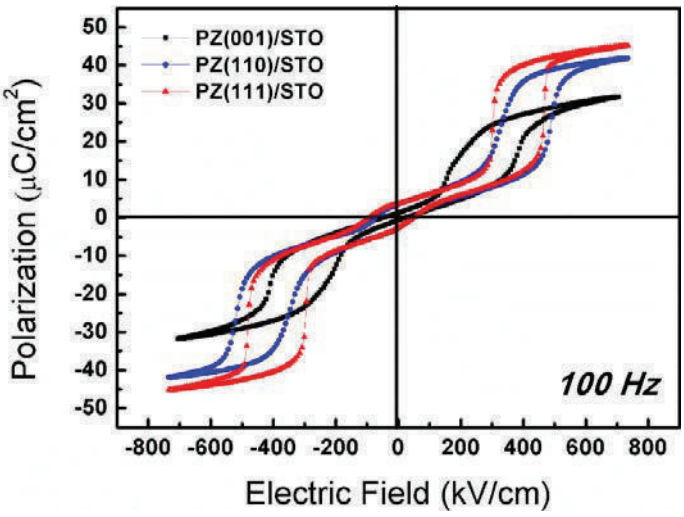

Figure 6.17 Room temperature hysteresis loops for PZ(001)/STO, PZ(110)/STO,and PZ(111)/STO

There exist a few discussions that might be helpful to explain the phenomena we observed here. Firstly, it is believed that the compressive stress can shift the AFE-FE and FE-AFE transition to higher electric field in $PbZrO_3$-based bulk ceramics[25] and even induce an AFE phase out of FE phase in particular situations.[73] This is due to the significant volume expansion during the AFE-FE transition of polycrystalline ceramics. Furthermore, Reyes-Lillo et al performed density-function calculations[74] on strained $PbZrO_3$ film and found different dependence relationships of AFE phase stability with strain for different growth orientation in a strain region of -1% to 1.5%, which can be applied to our films.

The increase of both maximum polarization and transition field could in turn increases the energy density of $PbZrO_3$ film following by

$$W=\int_{P_{max}}^{P_r} EdP \text{ (upon discharging)} \qquad (6\text{-}2)$$

Where E is the electric field, P_r and P_{max} are the remanent polarization and polarization at the highest field, respectively. The effect of manipulating the transition field and P_{max} can be seen explicitly by considering the fictitious example illustrated in Figure 6.18(a). There are three slim-loop polarization-field curves (A, B and C) along with the energy stored in each as a function of field (calculated according to Equation (6-2)). Although "B" has higher P_{max} than "A", the lower transition field restricts it to have the same energy density of "A". In contrast, "C'' can store much larger energy than "B" with the benefit of higher transition field.

However, it is worth noting that the high P_{max} and large transition field are usually exclusive in one certain material, which can be explained by that the higher P_{max} means the orientation of film is nearer to polar vector of FE phase hence leads to lower transition field.[78,139] Figure 6.18(b) shows a typical example to compare (110)/(101)-oriented $PbZrO_3$ film (PZ(110)/Si) with (001)-oriented $PbZrO_3$ film on Si (PZ(001)/Si). The shaded areas represent the recoverable energy during the FE-AFE switching. The inset plots the curve of energy density of two films with electric field indicating two films have similar value of energy density. By contrast, our epitaxial samples on STOs with certain orientations show promising energy storage density because of their capacity of both high P_{max} and large transition field.

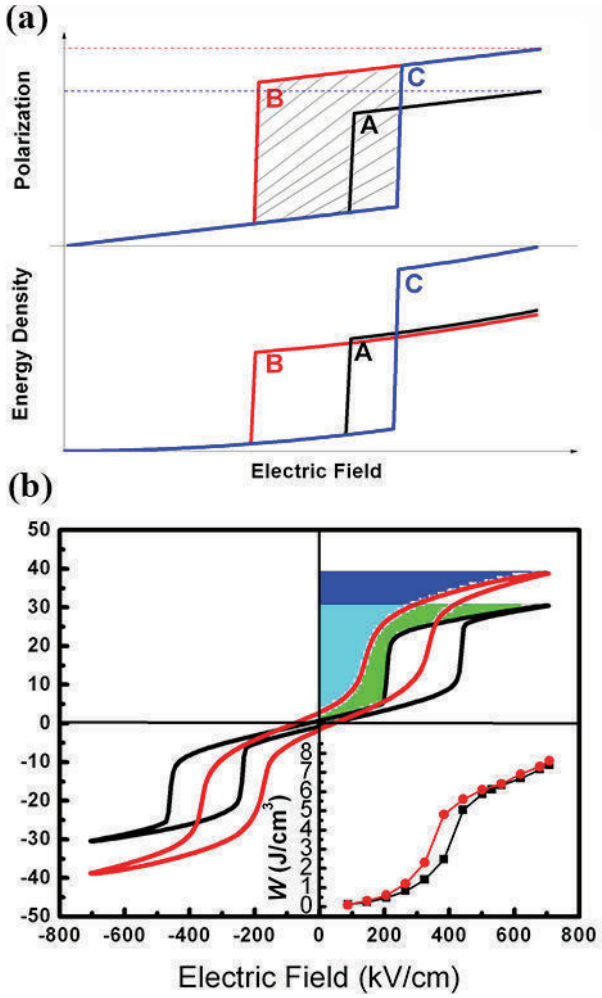

Figure 6.18(a) Fictitious AFE capacitor "A" develops lower saturated polarization than "B" but shows higher phase switching field. Therefore, while "B"develops greater energy density at low fields, the ultimate energy storage capabilities are the same as "A." (b) P-E loops of $PbZrO_3$ films on SiO_2/Si substrates with (001) and (110)/(101) orientation, respectively. Inset shows the energy density of both samples with electric field

The dependence curves of energy density on electric field of all three samples shown in Figure 6.19 were investigated. With the increasing of electric field, the energy density of all samples firstly increases slowly and shows an interrupt jump where the phase transition occurs. It is clear that PZ(110)/STO and PZ(111)/STO show a notable enhancement in the energy storage density when compared to

PZ(001)/STO sample. At room temperature, the energy density at 700kV/cm is 7.4 J/cm^3, 12.2 J/cm^3 and 12.5 J/cm^3 for PZ(001)/STO, PZ(110)/STO and PZ(111)/STO, respectively. Note that in pure $PbZrO_3$ film, 7.4 J/cm^3 is already a pretty high value of energy density compared with other reports.[22] It shows that approximately 70% enhancement in energy density can be obtained in PZ(110)/STO and PZ(111)/STO samples compared with PZ(001)/STO, which is not the case between PZ(110)/Si and PZ(001)/Si. In addition, in order to highlight the role of epitaxial strain, we deliberately prepared polycrystalline (110)/(101)-oriented $PbZrO_3$ film on STO substrate, denoted as PZ(110)-poly/STO. It can be seen that the PZ(110)-poly/STO shows a rather diffused curve with the energy density of 9.2 J/cm^3 at 700kV/cm, corresponding to a 24% increase compared with PZ(001)/STO, however, obviously lower than the energy density of PZ(110)/STO. This result strongly indicates that epitaxial strain in our samples is the dominated factor that influences the transition field and energy density of $PbZrO_3$ films.

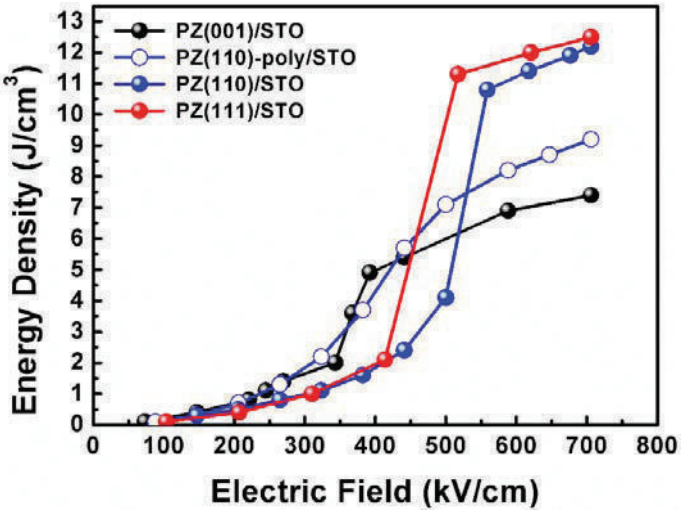

Figure 6.19 Dependence of energy density on electric field for PZ(001)/STO, PZ(110)/STO, PZ(110)-poly/STO, and PZ(111)/STO

Devices in practical applications are often needed to operate above room temperature, therefore the temperature stability of energy density is required. We measured the hysteresis loops in a broad temperature range in a vacuum of 10^{-5} mbar. The temperature was increased from 290K to 420K and electric measurements were made every roughly 15K. The AFE-FE and FE-AFE switching fields decrease with increasing temperature, corresponding to the thermo-induced AFE to paraelectric transition. The energy density can be plotted versus temperature as shown in Figure 6.20. It can be seen that the energy density of all samples show a slow decline as temperature increases and they retain at least 70% of their energy density at 420K. This finding indicates that all samples have rather good temperature stability up to 420K with the decreasing of energy density well below 0.3% per degree. This indicates that our electroceramic dielectric might have important advantages over the other technologies which might struggle in high temperature environments. For example, the terpolymer of VDF-TrFE–chlorofluoroethylene, an extensively studied polymer dielectric for energy storage,[23] will melt around 390K. Besides, it is worth noting that there is still plenty of scope for improving the temperature stability of our film, such as ion doping like partial substitution Sr^{2+} for Pb^{2+} which will increase the Curie temperature.[120]

The material devices are often required to operate under conditions of varying frequencies and electric field in practical applications. Therefore, a prior knowledge of how the material properties change under different operating

conditions and establishment of their scaling relation is considerably crucial for the selection of a suitable working condition and the design of a proper energy-storage device. Many theoretical studies have been focused on scaling law <A> $\propto f^{\alpha}E_0^{\beta}$ (where α and β are exponents that depend on the dimensionality and symmetry of the system) of hysteresis curves in polarization systems. In the realm of antiferroelectric, Kim et al.[4145] observed the *f*- and E_0-dependence of the dynamic hysteresis in a AFE betaine phosphate-arsenate ($BP_{0.9}A_{0.1}$) crystal, and found two scaling relations of hysteresis area <A> against *f* and E_0 at frequency below 200Hz, i.e.,

$$<A> \propto f^{0.40}(E-E_c)^{0.50} \text{ for saturated loops} \quad (6\text{-}3)$$

$$<A> \propto f^{0.28}(E-E_c)^{2.12} \text{ for minor loops} \quad (6\text{-}4)$$

where E_c is the threshold field for the AFE-FE phase transition. Hence in this study, we present the results on the scaling behavior of the dynamic hysteresis of epitaxial $PbZrO_3$ thin film.

The saturated polarization-electric field (*P*-*E*) loop and its corresponding current (*I*)-electric field (*E*) curve at 704 kV/cm and 50 Hz are illustrated in Figure 6.21. The film exhibits the AFE nature with a typical double hysteresis loops and four current peaks. The saturated polarization (P_s) reaches ~43 μC/cm^2 while the remanent polarization (P_r) is near zero with a small value around 2 μC/cm^2. The first two current peaks of the *I*-*E* curve, which correspond to the forward switching field E_{AF} and the backward switching field $E_{FA,}$ can be interpreted as AFE-FE and FE-AFE switching fields, respectively. According to the *I*-*E* curve,

the values of E_{AF} and E_{FA} are determined to be 499 kV/cm and 337 kV/cm, respectively.

The hysteresis loops of $PbZrO_3$ films at various E and f are shown in Figure 6.21. The hysteresis area <A> increases a little bit with the increase of frequency. The dependence of hysteresis loops on E is depicted by comparing loops in different figures. The lowest electric field is set deliberately high enough to avoid the antiferroelectric region, which ensures the well saturated loops are achieved.

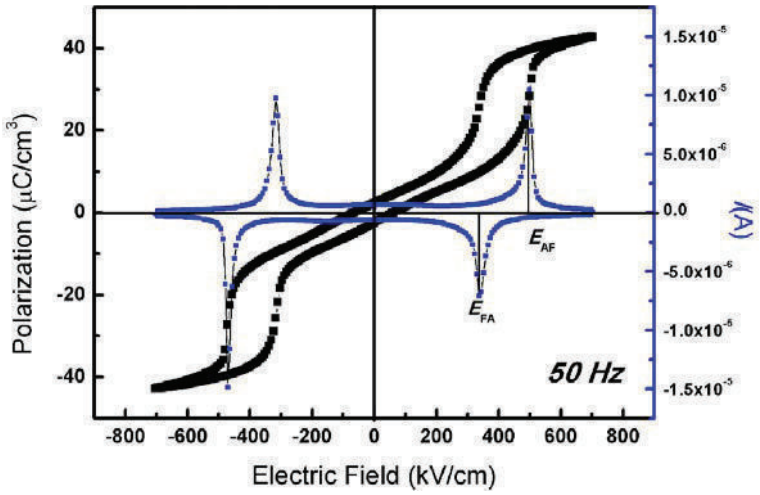

Figure 6.21 Double hysteresis loop and corresponding current curve of $PbZrO_3$ films at ~700 kV/cm and 50 Hz

The hysteresis loops of $PbZrO_3$ films at various E and f are shown in Figure 6.22. The hysteresis area <A> increases a little bit with the increase of frequency. The dependence of hysteresis loops on E is depicted by comparing loops in different figures.

To investigate the scaling behavior, we followed the scaling relations of Equation (6-3) and (6-4) and fitted these data of double loops with $<A> \propto f^{\alpha}(E-$

$E_{AF})^{\beta}$. To obtain the suitable scaling relation for our film, the E-term exponent β is obtained by plotting <A> against (E_0-E_{AF}) at 10 Hz. Similarly, the f-term exponent α is obtained by plotting <A> against f at fixed field of 667 kV/cm. The data are shown in Figure 6.23 and the solid line represents a fitting in terms of

$$<A> \propto f^{0.03}(E\text{-}499)^{0.20} \quad (6\text{-}5)$$

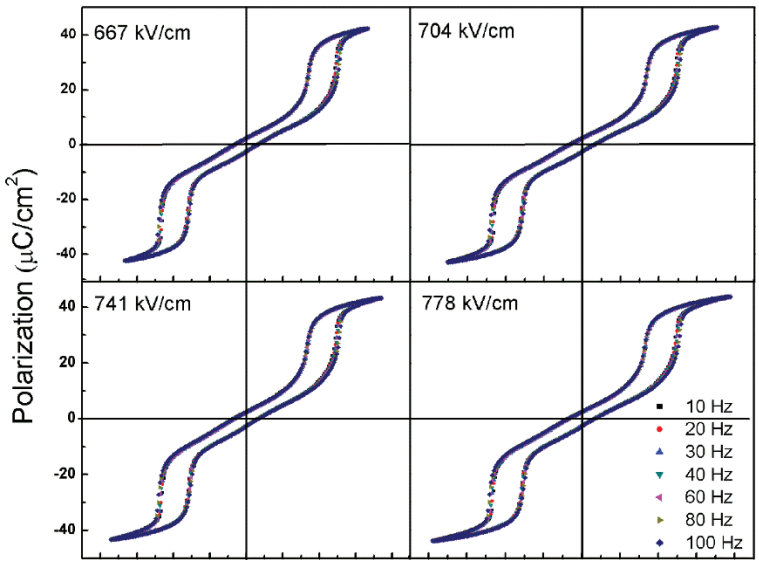

Figure 6.22 Hysteresis loops of epitaxial PZ films at various f and E_0 of (a) 667 kV/cm, (b) 704 kV/cm, (c) 741 kV/cm, and (d) 778 kV/cm

Clearly, large deviation observed implies that such scaling relation is not applicable to our films. However, a closer look shows that the low f-term data can be reasonable fitted (with R^2 >0.99). As the f continues to increase, the data deviate from the relation gradually with a higher slope. It is possible that a different scaling behavior might be established for the higher f-field region, as reported in previous investigations.[140-144]

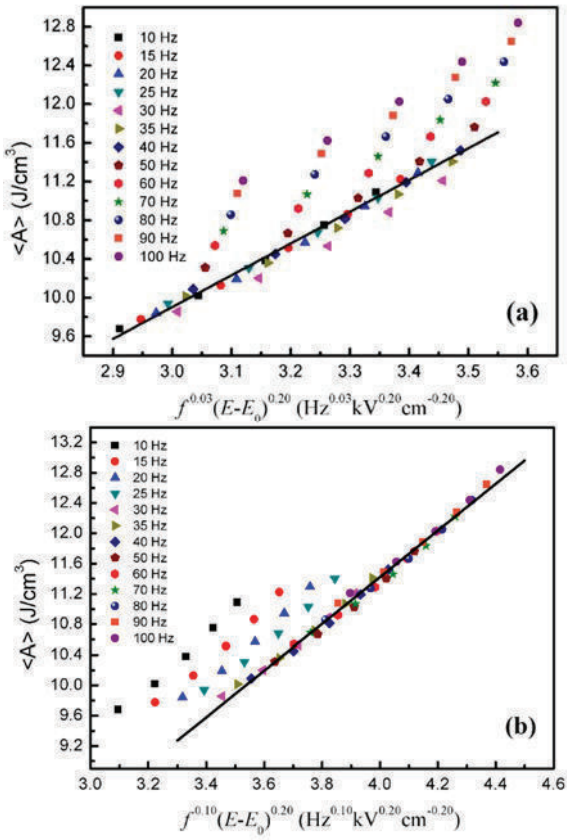

Figure 6.23 Scaling plot of hysteresis area <A> against (a) $f^{0.03}(E_0- E_A)^{0.20}$ and (b) $f^{0.10}(E_0- E_A)^{0.20}$ for double loops of $PbZrO_3$ films

Returning to the observation of Figure 6.23(a), there are actually two slopes-one at low frequency f and a different slope at relatively high frequency f (at different E fields). We fit the data with a higher α in terms of:

$$<A> \propto f^{0.10}(E\text{-}499)^{0.20} \qquad (6\text{-}6)$$

as shown in Figure 6.23(b). It is therefore important to explain the fundamental nature of different slopes with f. Firstly, we may interpret E_{AF} by the mechanical consideration as an effective field necessary to overcome restoring force (F_R) (turning back to AFE phases) and viscous force (F_V) in domain wall motions. Fig.

6.24(a) and 6.24(b) show schematically, how these forces act on the domains during the application and removal of electric field, respectively.

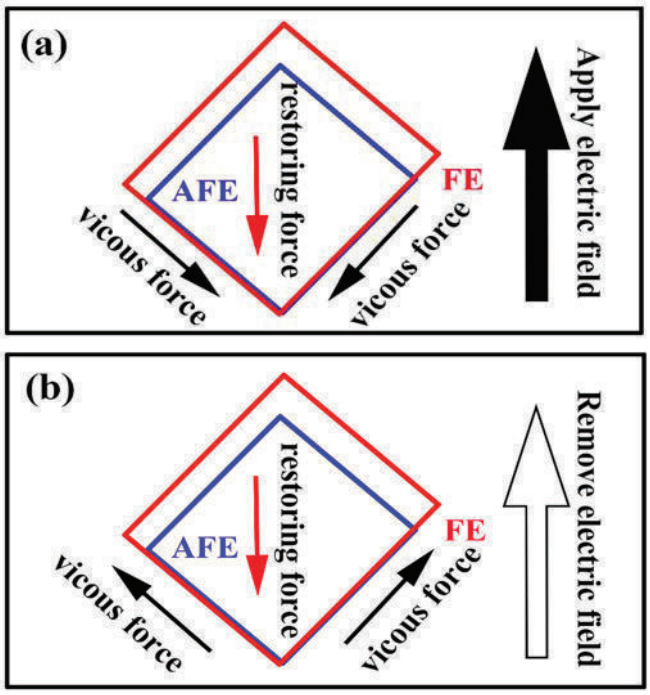

Figure 6.24 Representation of forces acting on phases during the phase transition: (a) during the application of the electric field and (b) during the removal of the field

As shown in the figures, the F_V always hinders AFE-FE and FE-AFE phase transition during forward and backward processes, thus increase the E_{AF} and decrease the E_{FA}, respectively. This will lead to an increase in hysteresis area <A>. At lower *f*, the velocity of the motions is relatively low and F_V could be neglected, and consequently, only F_R and electrical forces act on them. With increasing *f*, the material become more viscous because of the increasing speed of the phase transition movement, and F_V increases accordingly due to their higher velocity, thus this can lead to a higher rate of increase of <A> with *f*. Furthermore, the F_V

apparently is not affected by the magnitude of electric field, hence the relation of <A> with E goes with a constant parameter β.

6.2.4 Conclusion

In conclusion, we revealed the effect of strain on polarization switching of epitaxial AFE films with different orientations. Altering the crystallographic orientation of the substrate to (110) or (111) enabled us to change the constrain states of the films and suppress the AFE-FE phase transition to higher electric field. In addition, a larger saturated polarization could also be achieved for the film with (110) or (111) orientation, thereby yielding a dramatically enhanced energy storage density. Furthermore, the energy density showed a good stability with temperature up to 420 K. At last, it is worth mentioning that our demonstrated approach can also be applied to enhance properties for other applications. For example, reducing the E_F, which might be achieved by an engineering opposite from here, can be useful for enhanced piezoelectric response. We hope that these findings may open a new route to advance studies on $PbZrO_3$-based AFE functional devices.

The scaling relation for the saturated hysteresis loops of the epitaxial $PbZrO_3$ AFE thin film takes the form of $<A> \propto f^{0.03}(E_0\text{-}E_{AF})^{0.20}$ at relatively low testing frequency f. However, when frequency exceeds 30 Hz, the <A> shows stronger dependence on f while remains basically unchanged with E, leading to a form of $<A> \propto f^{0.10}(E_0\text{-}E_{AF})^{0.20}$. As a result, the study provides a detailed understanding of

how the <A> of the double loops of AFE thin film behaves in response to various frequency and electric field conditions. We model the dynamic behavior as occurring in a viscous medium where several forces, such as viscous and restoring forces, act on the phase transition process. We find that these relations are closely related to the variation of F_V with the frequency f.

CHAPTER 7

Conclusions and Future Work

Chapter 7 Conclusions and Future works

7.1 Conclusions

This thesis was dedicated to the phase transition and energy storage properties of $PbZrO_3$-based antiferroelectric films. The research was focused on the effect of strain on the shape of P-E loops and energy storage properties of the films and we further investigated the epitaxial strain in AFE films to enhance the energy density of films. In addition, we compared different top electrode materials and studied their impacts on energy storage density. Last, we investigated the scaling behaviors of AFE films by testing different electric fields and frequencies for practical application. Main conclusions are listed below:

(1) Firstly, antiferroelectric Pb(Zr, Nb, Ti)O_3 (PZNT) films were deposited via a sol-gel process on Pt(111)/Ti/SiO_2/Si, $LaNiO_3$- and $La_{0.5}Sr_{0.5}CoO_3$- buffered Si substrate. The scaling behavior of the energy density W of antiferroelectric films was investigated. The scaling behavior of W against frequency f of PZNT on $LaNiO_3$-buffered Si takes the form of $W \propto f^{0.08}$, which differs significantly from the form of $W \propto f^{-0.14}$ of PZNT on $La_{0.5}Sr_{0.5}CoO_3$-buffered Si. This indicates that the scaling relations of W vary substantially as bottom electrodes change and might be closely related to the variation of nonuniform strain field and depolarization field within the AFE films.

(2) Secondly, Polarization switching and energy storage properties of highly (100) oriented antiferroelectric (Pb,La)(Zr,Ti)O_3 thin films (≤ 250 nm) deposited via a sol-gel process with both $LaNiO_3$ and Pt top electrodes were investigated. By using $LaNiO_3$ top electrodes, the energy density as well as energy efficiency can be enhanced by 4.6 J/cm^3 and 11%, respectively. Furthermore, the films with $LaNiO_3$ top electrodes are more capable of providing high energy density over a wide temperature regime above room temperature compared to Pt. This work clearly highlights that oxide top electrodes can greatly improve the energy storage performance of antiferroelectric thin film capacitors.

(3) Thirdly, The effect of residual stress on energy storage property was investigated for a series of $PbZrO_3$ thin films on $SrTiO_3$ and Si substrates. Compressive or tensile residual stress influences the critical electric field E_A for the ferroelectric-to-antiferroelectric phase transition, thus for films with (110)/(101) orientation, energy density W of films on $SrTiO_3$ is 38% larger than films on Si; in contrast, (001)-oriented $PbZrO_3$ films on $SrTiO_3$ show slightly smaller W compared to films on Si. We conclude that the different responses of W to stress are related to the different constrain states in films with different orientations.

(4) On the basis of the previous work, we demonstrate an approach to enhance the energy storage density *W* of antiferroelectric films through simple altering a crystallographic orientation of the substrate. We reveal that the antiferroelectric

phase stability of $PbZrO_3$ can be enhanced for the (110) or (111) $SrTiO_3$ substrate orientation, thus suppresses the antiferroelectric-ferroelectric phase transition to higher electric field with ~120 kV/cm increment. In addition, the polarization values of these films are also favorably increased hence increases W by 5.3 J/cm^3 at 700 kV/cm. The observed enhancement is found to originate from a high sensitivity of phase transition to mechanical confinements due to the volume expansion at the transition.

(5) At last, we investigated the scaling behavior of dynamic hysteresis with frequency f and electric field E in epitaxial $PbZrO_3$ antiferroelectric film on (111)-oriented $SrTiO_3$ substrate. The scaling relation for the saturated hysteresis loops takes the form of hysteresis area $\langle A \rangle \propto f^{0.03}(E\text{-}499)^{0.20}$ at relatively low testing f. However, when frequency exceeds 30 Hz, the $\langle A \rangle$ shows stronger dependence on f while remains basically unchanged relation with E, leading to a form of $\langle A \rangle \propto f^{0.10}(E\text{-}499)^{0.20}$. The scaling behavior is modeled as occurring in a viscous medium where several forces, such as viscous and restoring forces, act on the phase transition process.

7.2 Future Work

Based on the previous experimental results and discussions, this work has opened up several directions and avenues where the materials can be improved and also further studies can be carried out to enhance the importance of the present

work in the energy storage and related fields of research. Some topics are described briefly below:

(1) Flexoelectricity in ferroelectric, especially thin films, has been widely studied in recent years and has found many interesting phenomena. However, study on flexoelectricity in antiferroelectric is rare. To investigate the effect of strain gradients on PZ antiferroelectric films, we can deposit PZ films with different thickness to create different strain state.

(2) Because Sn^{4+} dopant is reported to elevate the phase transition field of PZ antiferroelectric film, we can deposit Sn^{4+} doped PZ film to further enhance the energy density of films.

In Figure 7.1 we show some of our preliminary results on Sn-doped AFE films. The composition of the sputtering target is $PbZr_{0.9}Sn_{0.1}O_3$ (PZST). As we can see from the map, PZST film shows higher phase transition field and slimmer hysteresis loops, which offer higher energy density and energy efficiency. The next step is to make a series of experiments with different content of Sn dopant to obtain the optimal value.

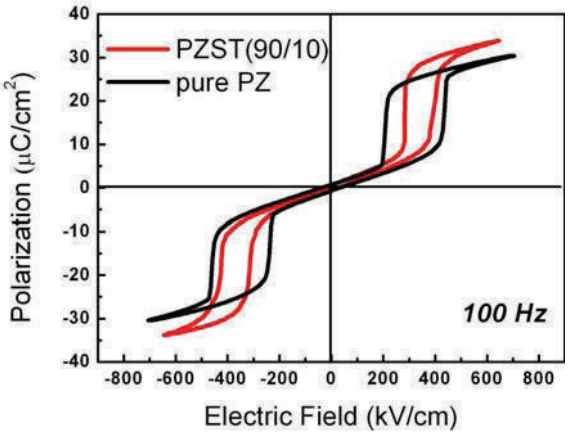

Figure 7.1 Hysteresis loops of PZST and PZ films measured at 100 Hz

(3) Because of the toxicity of Pb element, lead-free materials are more desirable. Hence, it is interesting and technologically important to obtain lead-free dielectric materials with high energy storage density.

$BiFeO_3$ (BFO) is a promising ferroelectric candidate with large saturated polarization and also room temperature multiferroic. The main obstacle that hinders its application in energy storage is the the high remanent polarization. A promising solution is to combine BFO films with paraelectrics to decrease the remanent polarization. In our group, we have a long history of deposition of paraelectric $Ba(Sr,Ti)O_3$ films, hence the main effort is to obtain BFO with good properties.

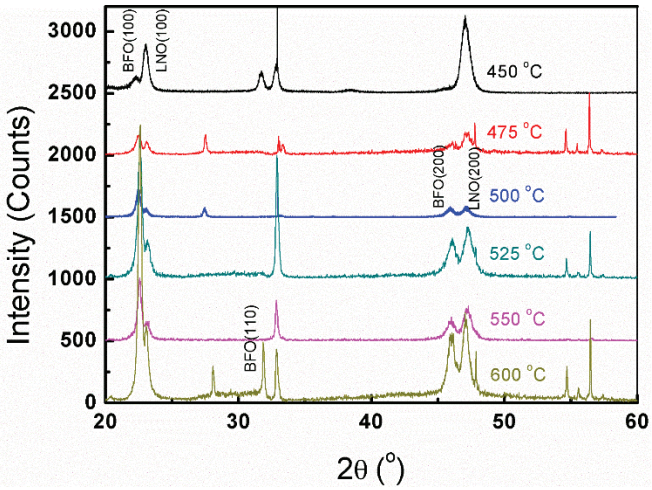

Figure 7.2 XRD patterns of BFO films depostied at various temperatures.

Figure 7.2 shows the XRD patterns of BFO films deposited at different temperatures. As it shows that, BFO peak can be seen even at a deposition temperature of 450 °C. As the temperature increased, the intensity of BFO peak increases accompanied by some peaks of impurity phase. Figure 7.3 shows the

cross-sectional and surface SEM figures of BFO deposited at 550 ºC. It can be seen that on the surface of the film there are big grains, which are Bi_2O_3 phases.

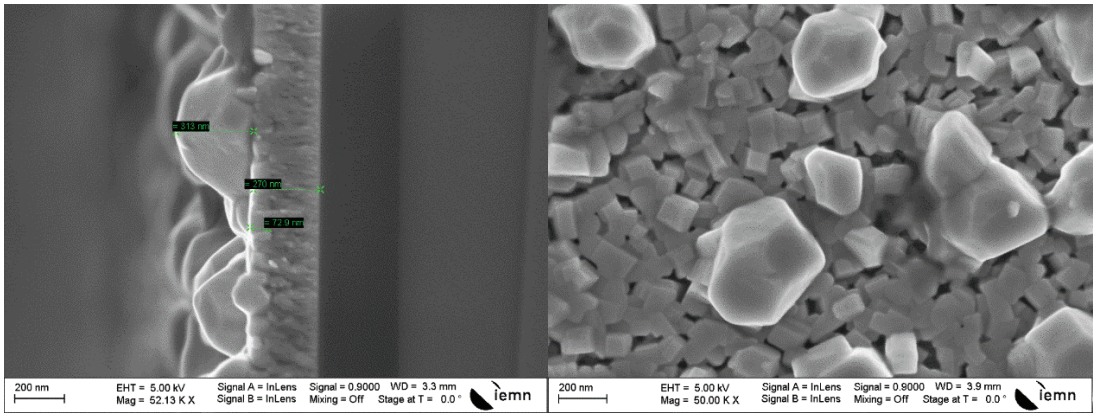

Figure 7.3 SEM figure of BFO films deposited at 550 ºC.

We found by increasing the deposition temperature to 620 ºC, Bi_2O_3 phases can be eliminated. Figure 7.4 shows the cross-sectional and surface SEM figures of BFO deposited at 620 ºC. The grains are much bigger than those deposited at 550 ºC and Bi_2O_3 phase is not found in these films. Hence, the next step is to measure the electrical properties of BFO films and combine the BFO film with BST films.

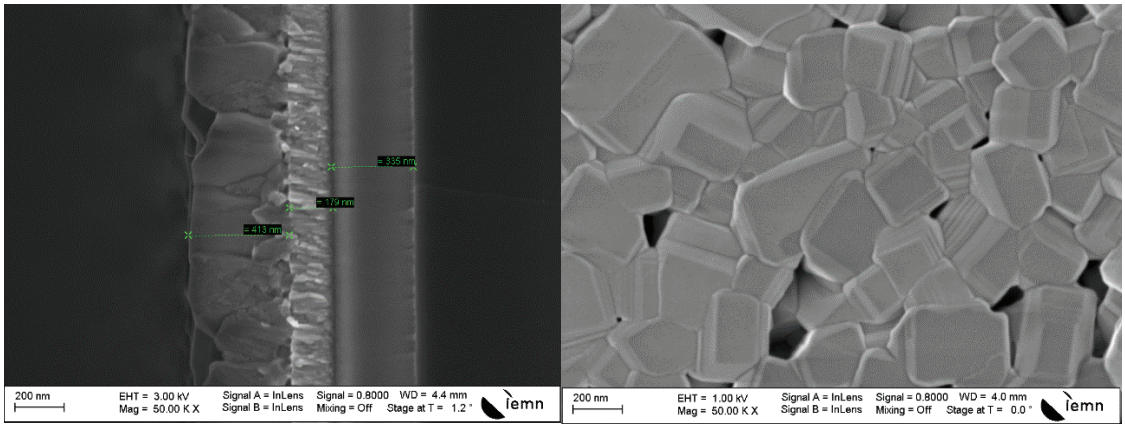

Figure 7.4 SEM figure of BFO films deposited at 620 ºC.

Reference

[1] M. F. El-Kady, R. B. Kaner. Scalable fabrication of high-power graphene micro-supercapacitors for flexible and on-chip energy storage [J]. Nat Commun. 2013, 4 1475.

[2] D. Pech, M. Brunet, H. Durou, P. Huang, V. Mochalin, Y. Gogotsi, P.-L. Taberna, P. Simon. Ultrahigh-power micrometre-sized supercapacitors based on onion-like carbon [J]. Nat Nano. 2010, 5 (9): 651-654.

[3] X. Hao and J. Zhai. Electric-field tunable electrocaloric effects from phase transition between antiferroelectric and ferroelectric phase [J]. Appl Phys Lett. 2014, 104 (2): 554-556.

[4] K. Yao, S. Chen, M. Rahimabady, M. S. Mirshekarloo, S. Yu, F. E. Tay, T. Sritharan, L. Lu. Nonlinear dielectric thin films for high-power electric storage with energy density comparable with electrochemical supercapacitors [J]. IEEE Trans Ultrason Ferroelectr Freq Control. 2011, 58 (9): 1968-1974.

[5] J. Li, S. I. Seok, B. Chu, F. Dogan, Q. Zhang, Q. Wang. Nanocomposites of Ferroelectric Polymers with TiO2 Nanoparticles Exhibiting Significantly Enhanced Electrical Energy Density [J]. Adv Mater. 2009, 21 (2): 217-221.

[6] A. L. M. Reddy, S. R. Gowda, M. M. Shaijumon, P. M. Ajayan. Hybrid Nanostructures for Energy Storage Applications [J]. Adv Mater. 2012, 24 (37): 5045-5064.

[7] L. Huang, Z. Jia, I. Kymissis, S. O'Brien. High K Capacitors and OFET Gate Dielectrics from Self-Assembled BaTiO3 and (Ba,Sr)TiO3 Nanocrystals in the Superparaelectric Limit [J]. Adv Funct Mater. 2010, 20 (4): 554-560.

[8] L. A. Fredin, Z. Li, M. T. Lanagan, M. A. Ratner, T. J. Marks. Substantial Recoverable Energy Storage in Percolative Metallic Aluminum-Polypropylene Nanocomposites [J]. Adv Funct Mater. 2013, 23 (28): 3560-3569.

[9] H. Tang, Y. Lin, H. A. Sodano. Synthesis of High Aspect Ratio $BaTiO_3$ Nanowires for High Energy Density Nanocomposite Capacitors [J]. Advanced Energy Materials. 2013, 3 (4): 451-456.

[10] Y. Qiao, M. S. Islam, K. Han, E. Leonhardt, J. Zhang, Q. Wang, H. J. Ploehn, and C. Tang. Polymers Containing Highly Polarizable Conjugated Side Chains as High-Performance All-Organic Nanodielectric Materials [J]. Adv Funct Mater. 2013, 23 (45): 5638-5646.

[11] S. Wu, W. Li, M. Lin, Q. Burlingame, Q. Chen, A. Payzant, K. Xiao, Q. M. Zhang. Aromatic Polythiourea Dielectrics with Ultrahigh Breakdown Field Strength, Low Dielectric Loss, and High Electric Energy Density [J]. Adv Mater. 2013, 25 (12): 1734-1738.

[12] Z.-M. Dang, J.-K. Yuan, S.-H. Yao, R.-J. Liao. Flexible Nanodielectric Materials with High Permittivity for Power Energy Storage [J]. Adv Mater. 2013, 25 (44): 6334-6365.

[13] B. Chu, X. Zhou, K. Ren, B. Neese, M. Lin, Q. Wang, F. Bauer, Q. M. Zhang. A Dielectric Polymer with High Electric Energy Density and Fast Discharge Speed [J]. Science. 2006, 313 (5785): 334-336.

[14] H. Tang, Y. Lin, H. A. Sodano. Enhanced Energy Storage in Nanocomposite Capacitors through Aligned PZT Nanowires by Uniaxial Strain Assembly [J]. Advanced Energy Materials. 2012, 2 (4): 469-476.

[15] C. Liu, F. Li, L.-P. Ma, H.-M. Cheng. Advanced Materials for Energy Storage [J]. Adv Mater. 2010, 22 (8): 28-62.

[16] B. Ma, D.-K. Kwon, M. Narayanan, U. Balachandran. Dielectric properties and energy storage capability of antiferroelectric $Pb_{0.92}La_{0.08}Zr_{0.95}Ti_{0.05}O_3$ film-on-foil capacitors [J]. J Mater Res. 2009, 24 (9): 2993-2996.

[17] W. N. Lawless, C. F. Clark, presented at the Energy Conversion Engineering Conference, 1996. IECEC 96., Proceedings of the 31st Intersociety, 1996 (unpublished).

[18] X. Tan, C. Ma, J. Frederick, S. Beckman, K. G. Webber. The Antiferroelectric ↔ Ferroelectric Phase Transition in Lead-Containing and Lead-Free Perovskite Ceramics [J]. J Am Ceram Soc. 2011, 94 (12): 4091-4107.

[19] X. Hao, J. Zhai, L. B. Kong, Z. Xu. A comprehensive review on the progress of lead zirconate-based antiferroelectric materials [J]. Prog Mater Sci. 2014, 63 (0): 1-57.

[20] D. Dragan. Ferroelectric, dielectric and piezoelectric properties of ferroelectric thin films and ceramics [J]. Rep Prog Phys. 1998, 61 (9): 1267.

[21] V. K. Sergei, N. M. Anna, C. Long Qing, J. R. Brian. Local polarization dynamics in ferroelectric materials [J]. Rep Prog Phys. 2010, 73 (5): 056502.

[22] H. R. Zeng, H. F. Yu, X. G. Tang, R. Q. Chu, G. R. Li, Q. R. Yin. Piezoresponse force microscopy studies of nanoscale domain structures in ferroelectric thin film [J]. Materials Science and Engineering: B. 2005, 120 (1–3): 104-108.

[23] R. Xu, S. Liu, I. Grinberg, J. Karthik, A. R. Damodaran, A. M. Rappe, L. W. Martin. Ferroelectric polarization reversal via successive ferroelastic transitions [J]. Nat Mater. 2014, advance online publication.

[24] D. Lee, B. C. Jeon, A. Yoon, Y. J. Shin, M. H. Lee, T. K. Song, S. D. Bu, M. Kim, J.-S. Chung, J.-G. Yoon, T. W. Noh. Flexoelectric Control of Defect Formation in Ferroelectric Epitaxial Thin Films [J]. Adv Mater. 2014, 26 (29): 5005-5011.

[25] A. Datta, D. Mukherjee, S. Witanachchi, P. Mukherjee. Hierarchically Ordered Nano-Heterostructured PZT Thin Films with Enhanced Ferroelectric Properties [J]. Adv Funct Mater. 2014, n/a-n/a.

[26] R. V. K. Mangalam, J. Karthik, A. R. Damodaran, J. C. Agar, L. W. Martin. Unexpected Crystal and Domain Structures and Properties in Compositionally Graded $PbZr_{1-x}Ti_xO_3$ Thin Films [J]. Adv Mater. 2013, 25 (12): 1761-1767.

[27] D. Lee, B. C. Jeon, S. H. Baek, S. M. Yang, Y. J. Shin, T. H. Kim, Y. S. Kim, J.-G. Yoon, C. B. Eom, T. W. Noh. Active Control of Ferroelectric Switching Using Defect-Dipole Engineering [J]. Adv Mater. 2012, 24 (48): 6490-6495.

[28] C.L. Jia, K. W. Urban, M. Alexe, D. Hesse, I. Vrejoiu. Direct Observation of Continuous Electric Dipole Rotation in Flux-Closure Domains in Ferroelectric Pb(Zr,Ti)O_3 [J]. Science. 2011, 331 (6023): 1420-1423.

[29] M. D. Nguyen, M. Dekkers, E. Houwman, R. Steenwelle, X. Wan, A. Roelofs, T. Schmitz-Kempen, G. Rijnders. Misfit strain dependence of ferroelectric and piezoelectric properties of clamped (001) epitaxial Pb($Zr_{0.52}Ti_{0.48}$)O_3 thin films [J]. Appl Phys Lett. 2011, 99 (25): 252904-252904.

[30] H. R. Jo, C. S. Lynch. Effect of composition on the pressure-driven ferroelectric to antiferroelectric phase transformation behavior of ($Pb_{0.97}La_{0.02}$)($Zr_{1-x-y}Sn_xTi_y$)O_3 ceramics [J]. J Appl Phys. 2014, 116 (7): 478-502.

[31] Z. Hu, B. Ma, R. E. Koritala, U. Balachandran. Temperature-dependent energy storage properties of antiferroelectric $Pb_{0.96}La_{0.04}Zr_{0.98}Ti_{0.02}O_3$ thin films [J]. Appl Phys Lett. 2014, 104 (26): -.

[32] J. Lasave, S. Koval, R. L. Migoni, N. S. Dalal. Ab initio studies of the para- and antiferroelectric structures and local polarized configurations in $NH_4H_2PO_4$ [J]. The Journal of Chemical Physics. 2011, 135 (8): 574-577.

[33] J. F. Webb. Theory of Size Effects in Antiferroelectric Ceramic Nano Scale Films on Metal Substrates [J]. AIP Conference Proceedings. 2009, 1136 (1): 523-527.

[34] S. S. N. Bharadwaja, S. B. Krupanidhi. Alternating current electrical properties of antiferroelectric lead zirconate thin films by pulsed excimer laser ablation [J]. J Appl Phys. 2000, 88 (4): 2072-2080.

[35] Y. Wang, X. Hao, J. Yang, J. Xu, and D. Zhao. Fabrication and energy-storage performance of (Pb,La)(Zr,Ti)O_3 antiferroelectric thick films derived from polyvinylpyrrolidone-modified chemical solution [J]. J Appl Phys. 2012, 112 (3): 147-152.

[36] S. S. N. Bharadwaja, S. B. Krupanidhi. Backward switching phenomenon from field forced ferroelectric to antiferroelectric phases in antiferroelectric $PbZrO_3$ thin films [J]. J Appl Phys. 2001, 89 (8): 4541-4547.

[37] R. Seveno, H. W. Gundel, D. Averty. Pulse characterization of antiferroelectric Pb(ZrTi)O_3 thin films [J]. J Eur Ceram Soc. 2005, 25 (12): 2263-2267.

[38] Y. Yao, S. G. Lu, H. Chen, J. Zhai, K. H. Wong. Role of oxygen pressure during pulsed laser deposition on the electrical and dielectric properties of antiferroelectric lanthanum-doped lead zirconate stannate titanate thin films [J]. J Appl Phys. 2004, 96 (1): 569-574.

[39] I. W. Kim, D. Su Lee, S. Hee Kang, C. Won Ahn. Antiferroelectric characteristics and low frequency dielectric dispersion of

$Pb_{1.075}La_{0.025}(Zr_{0.95}Ti_{0.05})O_3$ thin films [J]. Thin Solid Films. 2003, 441 (1–2): 115-120.

[40] R. Seveno, H. W. Gundel, S. Seifert. Preparation of antiferroelectric $Pb(ZrTi)O_3$ thin films on $LaSrMnO_3$-coated steel substrates [J]. Appl Phys Lett. 2001, 79 (25): 4204-4206.

[41] B. Xu, Y. Ye, Q.-M. Wang, L. E. Cross. Dependence of electrical properties on film thickness in lanthanum-doped lead zirconate titanate stannate antiferroelectric thin films [J]. J Appl Phys. 1999, 85 (7): 3753-3758.

[42] S. Tong, B. Ma, M. Narayanan, S. Liu, R. Koritala, U. Balachandran, D. Shi. Lead Lanthanum Zirconate Titanate Ceramic Thin Films for Energy Storage [J]. ACS Applied Materials & Interfaces. 2013, 5 (4): 1474-1480.

[43] L. Zhang, X. Hao, J. Yang, S. An, B. Song. Large enhancement of energy-storage properties of compositional graded $(Pb_{1-x}La_x)(Zr_{0.65}Ti_{0.35})O_3$ relaxor ferroelectric thick films [J]. Appl Phys Lett. 2013, 103 (11): 113902-113903.

[44] M. S. Mirshekarloo, K. Yao, T. Sritharan. Large strain and high energy storage density in orthorhombic perovskite, $(Pb_{0.97}La_{0.02})(Zr_{1-x-y}Sn_xTi_y)O_3$ antiferroelectric thin films [J]. Appl Phys Lett. 2010, 97 (14): 112913-142915.

[45] P. Banerjee, I. Perez, L. Henn-Lecordier, S. B. Lee, G. W. Rubloff. Nanotubular metal-insulator-metal capacitor arrays for energy storage [J]. Nat Nano. 2009, 4 (5): 292-296.

[46] M. H. Park, H. J. Kim, Y. J. Kim, T. Moon, K. D. Kim, C. S. Hwang. Thin $Hf_xZr_{1-x}O_2$ Films: A New Lead-Free System for Electrostatic Supercapacitors

with Large Energy Storage Density and Robust Thermal Stability [J]. Advanced Energy Materials. 2014, n/a-n/a.

[47] E. Sawaguchi, H. Maniwa, S. Hoshino. Antiferroelectric Structure of Lead Zirconate [J]. Physical Review. 1951, 83 (5): 1078-1078.

[48] J. Ge, X. Dong, Y. Chen, F. Cao, G. Wang. Enhanced polarization switching and energy storage properties of $Pb_{0.97}La_{0.02}(Zr_{0.95}Ti_{0.05})O_3$ antiferroelectric thin films with $LaNiO_3$ oxide top electrodes [J]. Appl Phys Lett. 2013, 102 (14): 142905-142907.

[49] X. H. Hao, Z. X. Yue, J. B. Xu, S. L. An, C. W. Nan. Energy-storage performance and electrocaloric effect in (100)-oriented $Pb_{0.97}La_{0.02}(Zr_{0.95}Ti_{0.05})O_3$ antiferroelectric thick films [J]. J Appl Phys. 2011, 110 (6): 3853-3858.

[50] X. Hao, J. Zhou, S. An. Effects of PbO Content on the Dielectric Properties and Energy Storage Performance of $(Pb_{0.97}La_{0.02})(Zr_{0.97}Ti_{0.03})O_3$ Antiferroelectric Thin Films [J]. J Am Ceram Soc. 2011, 94 (6): 1647-1650.

[51] I. Kanno, S. Hayashi, M. Kitagawa, R. Takayama, T. Hirao. ANTIFERROELECTRIC $PBZRO_3$ THIN-FILMS PREPARED BY MULTI-ION-BEAM SPUTTERING [J]. Appl Phys Lett. 1995, 66 (2): 145-147.

[52] K. Yamakawa, S. Troliermckinstry, J. P. Dougherty, S. B. Krupanidhi. REACTIVE MAGNETRON CO-SPUTTERED ANTIFERROELECTRIC LEAD ZIRCONATE THIN-FILMS [J]. Appl Phys Lett. 1995, 67 (14): 2014-2016.

[53] C. T. Blue, J. C. Hicks, S. E. Park, S. Yoshikawa, L. E. Cross. Insitu x‐ray diffraction study of the antiferroelectric–ferroelectric phase transition in PLSZT [J]. Appl Phys Lett. 1996, 68 (21): 2942-2944.

[54] S. S. Sengupta, D. Roberts, J. F. Li, M. C. Kim, D. A. Payne. Field-Induced Phase Switching and Electrically Driven Strains in Sol-Gel Derived Antiferroelectric (Pb,Nb)(Zr,Sn,Ti)O_3 Thin-Layers [J]. J Appl Phys. 1995, 78 (2): 1171-1177.

[55] X. Hao, J. Zhou, S. An. Effects of PbO Content on the Dielectric Properties and Energy Storage Performance of $(Pb_{0.97}La_{0.02})(Zr_{0.97}Ti_{0.03})O_3$ Antiferroelectric Thin Films [J]. J Am Ceram Soc. 2011, 94 (6): 1647-1650.

[56] B. M. Xu, X. H. Ye, Q. M. Wang, N. G. Pai, L. E. Cross. Effect of compositional variations on electrical properties in phase switching (Pb,La)(Zr,Ti,Sn)O_3 thin and thick films [J]. J Mater Sci. 2000, 35 (23): 6027-6033.

[57] M. Ye, Q. Sun, X. Chen, Z. Jiang, F. Wang. Effect of Eu Doping on the Electrical Properties and Energy Storage Performance of $PbZrO_3$ Antiferroelectric Thin Films [J]. J Am Ceram Soc. 2011, 94 (10): 3234-3236.

[58] J. Parui, S. B. Krupanidhi. Enhancement of charge and energy storage in sol-gel derived pure and La-modified $PbZrO_3$ thin films [J]. Appl Phys Lett. 2008, 92 (19): 142019-142021.

[59] B. H. Ma, M. Narayanan, S. Tong, U. Balachandran. Fabrication and characterization of ferroelectric PLZT film capacitors on metallic substrates [J]. J Mater Sci. 2010, 45 (1): 151-157.

[60] S. Patel, A. Chauhan, R. Vaish. A technique for giant mechanical energy harvesting using ferroelectric/antiferroelectric materials [J]. J Appl Phys. 2014, 115 (8): 5847-5850.

[61] X. Tan, J. Frederick, C. Ma, E. Aulbach, M. Marsilius, W. Hong, T. Granzow, W. Jo, J. Rödel. Electric-field-induced antiferroelectric to ferroelectric phase transition in mechanically confined $Pb_{0.99}Nb_{0.02}[(Zr_{0.57}Sn_{0.43})_{0.94}Ti_{0.06}]_{0.98}O_3$ [J]. Phys Rev B. 2010, 81 (1): 014103-014106.

[62] X. Tan, J. Frederick, C. Ma, W. Jo, J. Rodel. Can an Electric Field Induce an Antiferroelectric Phase Out of a Ferroelectric Phase? [J]. Phys Rev Lett. 2010, 105 (25): 014115-014118.

[63] S. E. Young, J. Y. Zhang, W. Hong, X. Tan. Mechanical self-confinement to enhance energy storage density of antiferroelectric capacitors [J]. J Appl Phys. 2013, 113 (5): 5847-5850.

[64] N. Yasuda, H. Shimizu, S. Fujimoto, Y. Inuishi, K. Yoshino. Effect of the uniaxial stress on the dielectric properties of antiferroelectric cupric formate tetrahydrate [J]. J Appl Phys. 1978, 49 (1): 383-389.

[65] A. Q. Jiang, D. W. Zhang, T. A. Tang. Nonlinear antiferroelectric-like capacitance-voltage curves in ferroelectric BiFeO3 thin films [J]. J Appl Phys. 2013, 114 (2): 5872-5878.

[66] Y. Xu, Y. Feng, N. Zhang, Y. Yan, L. Liao. Phenomenological theory of electric-field-induced phase transition behavior of antiferroelectric ceramic (Pb,Ba,La)(Zr,Sn,Ti)O3 under uniaxial compressive pre-stress [J]. J Appl Phys. 2012, 112 (3): -.

[67] I. J. Fritz. Stress effects in two modified lead zirconate titanate ferroelectric ceramics [J]. J Appl Phys. 1979, 50 (8): 5265-5271.

[68] I. J. Fritz. Uniaxial - stress effects in a 95/5 lead zirconate titanate ceramic [J]. J Appl Phys. 1978, 49 (9): 4922-4928.

[69] J. C. Valadez, R. Sahul, E. Alberta, W. Hackenberger, C. S. Lynch. The effect of a hydrostatic pressure induced phase transformation on the unipolar electrical response of Nb modified 95/5 lead zirconate titanate [J]. J Appl Phys. 2012, 111 (2): 5837-5840.

[70] B. M. Xu, Y. H. Ye, L. E. Cross. Dielectric properties and field-induced phase switching of lead zirconate titanate stannate antiferroelectric thick films on silicon substrates [J]. J Appl Phys. 2000, 87 (5): 2507-2515.

[71] B. M. Xu, L. E. Cross, D. Ravichandran. Synthesis of lead zirconate titanate stannate antiferroelectric thick films by sol-gel processing [J]. J Am Ceram Soc. 1999, 82 (2): 306-312.

[72] A. R. Chaudhuri, M. Arredondo, A. Hahnel, A. Morelli, M. Becker, M. Alexe, I. Vrejoiu. Epitaxial strain stabilization of a ferroelectric phase in $PbZrO_3$ thin films [J]. Phys Rev B. 2011, 84 (5): 014121-014123.

[73] M. S. Mirshekarloo, K. Yao, T. Sritharan. Ferroelastic Strain Induced Antiferroelectric-Ferroelectric Phase Transformation in Multilayer Thin Film Structures [J]. Adv Funct Mater. 2012, 22 (19): 4159-4164.

[74] X. F. Chen, F. Cao, H. L. Zhang, G. Yu, G. S. Wang, X. L. Dong, Y. Gu, H. L. He, Y. S. Liu. Dynamic Hysteresis and Scaling Behavior of Energy Density in $Pb_{0.99}Nb_{0.02}(Zr_{0.60}Sn_{0.40})(Zr_{0.95}Ti_{0.05})O_3$ Antiferroelectric Bulk Ceramics [J]. J Am Ceram Soc. 2012, 95 (4): 1163-1166.

[75] J. W. Zhai, M. H. Cheung, K. X. Zheng, L. Xin, H. D. Chen, E. V. Colla, T. B. Wu. Dielectric and ferroelectric properties of highly oriented $(Pb,Nb)(Zr,Sn,Ti)O_3$ thin films grown by a sol-gel process [J]. Appl Phys Lett. 2002, 81 (19): 3621-3623.

[76] E. A. Eliseev, M. D. Glinchuk. Size-induced appearance of ferroelectricity in thin antiferroelectric films [J]. Physica B: Condensed Matter. 2007, 400 (1–2): 106-113.

[77] P. Ayyub, S. Chattopadhyay, R. Pinto, M. S. Multani. Ferroelectric behavior in thin films of antiferroelectric materials [J]. Phys Rev B. 1998, 57 (10): R5559-R5562.

[78] X. Hao, J. Zhai, J. Yang, H. Ren, X. Song. Improved field-induced strains and fatigue endurance of PLZT antiferroelectric thick films by orientation control [J]. Physica Status Solidi-Rapid Research Letters. 2009, 3 (7-8): 248-250.

[79] X. Hao, J. Zhai, X. Yao. Improved Energy Storage Performance and Fatigue Endurance of Sr-Doped $PbZrO_3$ Antiferroelectric Thin Films [J]. J Am Ceram Soc. 2009, 92 (5): 1133-1135.

[80] J. W. Zhai, H. D. Chen. Electric fatigue in $Pb(Nb,Zr,Sn,Ti)O_3$ thin films grown by a sol-gel process [J]. Appl Phys Lett. 2003, 83 (5): 978-980.

[81] M. D. Glinchuk, B. Y. Zaulychny, V. A. Stephanovich. Depolarization field and properties of thin ferroelectric films with inclusion of the electrode effect [J]. Phys Solid State+. 2005, 47 (7): 1331-1339.

[82] M. D. Glinchuk, B. Y. Zaulychny, V. A. Stephanovich. Depolarization field in thin ferroelectric films with account of semiconductor electrodes [J]. Ferroelectrics. 2005, 316 1-6.

[83] F. Chen, Q. Z. Liu, H. F. Wang, F. H. Zhang, W. B. Wu. Polarization switching and fatigue in $Pb(Zr_{0.52}Ti_{0.48})O_3$ films sandwiched by oxide electrodes with different carrier types [J]. Appl Phys Lett. 2007, 90 (19): 961-963.

[84] A. Wold, B. Post, E. Banks. RARE EARTH NICKEL OXIDES [J]. J Am Chem Soc. 1957, 79 (18): 4911-4913.

[85] K. P. Rajeev, G. V. Shivashankar, A. K. Raychaudhuri. LOW-TEMPERATURE ELECTRONIC-PROPERTIES OF A NORMAL CONDUCTING PEROVSKITE OXIDE (LANIO3) [J]. Solid State Commun. 1991, 79 (7): 591-595.

[86] Y. Watanabe. Electrical transport through $Pb(Zr,Ti)O_3$ p-n and p-p heterostructures modulated by bound charges at a ferroelectric surface: Ferroelectric p-n diode [J]. Phys Rev B. 1999, 59 (17): 11257-11266.

[87] S. Jin, T. H. Tiefel, M. Mccormack, R. A. Fastnacht, R. Ramesh, L. H. Chen. Thousandfold Change in Resistivity in Magnetoresistive La-Ca-Mn-O Films [J]. Science. 1994, 264 (5157): 413-415.

[88] C. A. F. Vaz, Y. Segal, J. Hoffman, R. D. Grober, F. J. Walker, C. H. Ahn. Temperature dependence of the magnetoelectric effect in $Pb(Zr_{0.2}Ti_{0.8})O_3/La_{0.8}Sr_{0.2}MnO_3$ multiferroic heterostructures [J]. Appl Phys Lett. 2010, 97 (4): 142019-142021.

[89] C. Zou, Y. F. Chen, P. J. Li, R. Fan, B. Peng, W. X. Zhang, Z. G. Wang, X. Hao, J. B. Liu, W. L. Zhang, Y. R. Li, R. W. Li. Structure and properties of epitaxial perovskite $Pb(Zr_{0.52}Ti_{0.48})O_3/La_{0.7}Sr_{0.3}MnO_3$ heterostructures [J]. J Appl Phys. 2012, 111 (7): 847-852.

[90] A. K. Tagantsev, M. Landivar, E. Colla, and N. Setter. Identification of passive layer in ferroelectric thin films from their switching parameters [J]. J Appl Phys. 1995, 78 (4): 2623-2630.

[91] J. Karthik, A. R. Damodaran, and L. W. Martin. Epitaxial Ferroelectric Heterostructures Fabricated by Selective Area Epitaxy of SrRuO3 Using an MgO Mask [J]. Adv Mater. 2012, 24 (12): 1610-1615.

[92] Y. S. Kim, J. Y. Jo, D. J. Kim, Y. J. Chang, J. H. Lee, T. W. Noh, T. K. Song, J.G. Yoon, J.S. Chung, S. I. Baik, Y. W. Kim, C. U. Jung. Ferroelectric

properties of $SrRuO_3/BaTiO_3/SrRuO_3$ ultrathin film capacitors free from passive layers [J]. Appl Phys Lett. 2006, 88 (7): 072909-072911.

[93] S. Dussan, A. Kumar, J. F. Scott, S. Priya, R. S. Katiyar. Room temperature multiferroic effects in superlattice nanocapacitors [J]. Appl Phys Lett. 2010, 97 (25): 142905-142907.

[94] J. Wang, J. B. Neaton, H. Zheng, V. Nagarajan, S. B. Ogale, B. Liu, D. Viehland, V. Vaithyanathan, D. G. Schlom, U. V. Waghmare, N. A. Spaldin, K. M. Rabe, M. Wuttig, R. Ramesh. Epitaxial $BiFeO_3$ Multiferroic Thin Film Heterostructures [J]. Science. 2003, 299 (5613): 1719-1722.

[95] F. Xu, S. Trolier-McKinstry, W. Ren, B. M. Xu, Z. L. Xie, K. J. Hemker. Domain wall motion and its contribution to the dielectric and piezoelectric properties of lead zirconate titanate films [J]. J Appl Phys. 2001, 89 (2): 1336-1348.

[96] D. Damjanovic. A morphotropic phase boundary system based on polarization rotation and polarization extension [J]. Appl Phys Lett. 2010, 97 (6): 062906-062903.

[97] Z. Xu, W. H. Chan. Preparation and electrical properties of highly oriented antiferroelectric PLZST films by radio frequency magnetron sputtering [J]. Acta Mater. 2007, 55 (11): 3923-3928.

[98] T. Kopp, J. Mannhart. Calculation of the capacitances of conductors: Perspectives for the optimization of electronic devices [J]. J Appl Phys. 2009, 106 (6): 5472-5475.

[99] J. Mannhart, D. G. Schlom. Oxide Interfaces—An Opportunity for Electronics [J]. Science. 2010, 327 (5973): 1607-1611.

[100] A. Tagantsev, I. Stolichnov, E. Colla, N. Setter. Polarization fatigue in ferroelectric films: Basic experimental findings, phenomenological scenarios, and microscopic features [J]. J Appl Phys. 2001, 90 (3): 1387-1402.

[101] M. Dawber, J. Scott. A model for fatigue in ferroelectric perovskite thin films [J]. Appl Phys Lett. 2000, 76 (8): 1060-1062.

[102] A. V. Pogrebnyakov, X. X. Xi, J. M. Redwing, V. Vaithyanathan, D. G. Schlom, A. Soukiassian, S. B. Mi, C. L. Jia, J. E. Giencke, C. B. Eom, J. Chen, Y. F. Hu, Y. Cui, and Q. Li. Properties of MgB_2 thin films with carbon doping [J]. Appl Phys Lett. 2004, 85 (11): 2017-2019.

[103] G. Gerra, A. K. Tagantsev, N. Setter, and K. Parlinski. Ionic Polarizability of Conductive Metal Oxides and Critical Thickness for Ferroelectricity $BaTiO_3$ [J]. Phys Rev Lett. 2006, 96 (10): 107603.

[104] M. Stengel, D. Vanderbilt, N. A. Spaldin. Enhancement of ferroelectricity at metal-oxide interfaces [J]. Nat Mater. 2009, 8 (5): 392-397.

[105] L. Pintilie, C. Dragoi, Y. H. Chu, L. W. Martin, R. Ramesh, M. Alexe. Orientation-dependent potential barriers in case of epitaxial Pt-$BiFeO_3$-$SrRuO_3$ capacitors [J]. Appl Phys Lett. 2009, 94 (23).

[106] N. A. Pertsev, J. Rodríguez Contreras, V. G. Kukhar, B. Hermanns, H. Kohlstedt, R. Waser. Coercive field of ultrathin $Pb(Zr_{0.52}Ti_{0.48})O_3$ epitaxial films [J]. Appl Phys Lett. 2003, 83 (16): 3356-3358.

[107] J. Junquera and P. Ghosez. Critical thickness for ferroelectricity in perovskite ultrathin films [J]. Nature. 2003, 422 (6931): 506-509.

[108] D. D. Fong, G. B. Stephenson, S. K. Streiffer, J. A. Eastman, O. Auciello, P. H. Fuoss, C. Thompson. Ferroelectricity in Ultrathin Perovskite Films [J]. Science. 2004, 304 (5677): 1650-1653.

[109] W. Chen, Z. H. Wang, C. Ke, W. Zhu, O. K. Tan. Preparation and characterization of $Pb(Zr_{0.53}Ti_{0.47})O_3/CoFe_2O_4$ composite thick films by hybrid sol-gel processing [J]. Materials Science and Engineering B-Advanced Functional Solid-State Materials. 2009, 162 (1): 47-52.

[110] W. Chen, W. Zhu, X. Chen, Z. Wang. Enhanced Ferroelectric and Dielectric Properties of $CoFe_2O_4$-$Pb(Zr_{0.53}Ti_{0.47})O_3$ Multiferroic Composite Thick Films [J]. J Am Ceram Soc. 2010, 93 (3): 796-799.

[111] M. Toyota, H. Osamu, Y. Kouji, A. Osamu, K. Hiroyuki, I. Tsuyoshi, K. Yoshinori, K. Iwao, and T. Shin-ichi. Ferroelectric Properties of $Pb(Zi,Ti)O_3$ Capacitor with Thin $SrRuO_3$ Films within Both Electrodes [J]. Jpn J Appl Phys. 2000, 39 (4S): 2110.

[112] L. Pintilie, I. Vrejoiu, D. Hesse, G. LeRhun, M. Alexe. Ferroelectric polarization-leakage current relation in high quality epitaxial films [J]. Phys Rev B. 2007, 75 (10): 104103.

[113] D. Faccio, P. D. Trapani, S. Minardi, A. Bramati, F. Bragheri, C. Liberale, V. Degiorgio, A. Dubietis, A. Matijosius. Far-field spectral characterization

of conical emission and filamentation in Kerr media [J]. Journal of the Optical Society of America B. 2005, 22 (4): 862-869.

[114] K. J. Choi, M. Biegalski, Y. L. Li, A. Sharan, J. Schubert, R. Uecker, P. Reiche, Y. B. Chen, X. Q. Pan, V. Gopalan, L.-Q. Chen, D. G. Schlom, C. B. Eom. Enhancement of Ferroelectricity in Strained $BaTiO_3$ Thin Films [J]. Science. 2004, 306 (5698): 1005-1009.

[115] C. J. Gaskey, K. R. Udayakumar, H. D. Chen, L. E. Cross. Square Hysteresis Loops in Phase-Switching Nb-Doped Lead Zirconate Stannate Titanate Thin-Films [J]. J Mater Res. 1995, 10 (11): 2764-2769.

[116] C. Kittel. THEORY OF ANTIFERROELECTRIC CRYSTALS [J]. Physical Review. 1951, 82 (5): 729-732.

[117] B. M. Xu, N. G. Pai, L. E. Cross. Lanthanum doped lead zirconate titanate stannate antiferroelectric thin films from acetic acid-based sol-gel method [J]. Mater Lett. 1998, 34 (3-6): 157-160.

[118] I. W. Kim, D. S. Lee, S. H. Kang, C. W. Ahn. Antiferroelectric characteristics and low frequency dielectric dispersion of $Pb_{1.075}La_{0.025}(Zr_{0.95}Ti_{0.05})O_3$ thin films [J]. Thin Solid Films. 2003, 441 (1-2): 115-120.

[119] N. Ortega, A. Kumar, J. F. Scott, D. B. Chrisey, M. Tomazawa, S. Kumari, D. G. B. Diestra, R. S. Katiyar. Relaxor-ferroelectric superlattices: high energy density capacitors [J]. Journal of Physics: Condensed Matter. 2012, 24 (44): 445901.

[120] O. Y. Gorbenko, S. V. Samoilenkov, I. E. Graboy, A. R. Kaul. Epitaxial stabilization of oxides in thin films [J]. Chem Mater. 2002, 14 (10): 4026-4043.

[121] A. F. M. dos Santos, A. K. Cheetham, W. Tian, X. Q. Pan, Y. F. Jia, N. J. Murphy, J. Lettieri, D. G. Schlom. Epitaxial growth and properties of metastable $BiMnO_3$ thin films [J]. Appl Phys Lett. 2004, 84 (1): 91-93.

[122] D. Lee, A. Yoon, S. Y. Jang, J. G. Yoon, J. S. Chung, M. Kim, J. F. Scott, T. W. Noh. Giant Flexoelectric Effect in Ferroelectric Epitaxial Thin Films [J]. Phys Rev Lett. 2011, 107 (5): 647-649.

[123] S. Gariglio, N. Stucki, J. M. Triscone, G. Triscone. Strain relaxation and critical temperature in epitaxial ferroelectric $Pb(Zr_{0.20}Ti_{0.80})O_3$ thin films [J]. Appl Phys Lett. 2007, 90 (20): 202905-202903.

[124] B. Ma, S. Liu, S. Tong, M. Narayanan, and U. Balachandran. Enhanced dielectric properties of $Pb_{0.92}La_{0.08}Zr_{0.52}Ti_{0.48}O_3$ films with compressive stress [J]. J Appl Phys. 2012, 112 (11): 142015-142019.

[125] J. Ge, D. Remiens, J. Costecalde, Y. Chen, X. Dong, and G. Wang. Effect of residual stress on energy storage property in $PbZrO_3$ antiferroelectric thin films with different orientations [J]. Appl Phys Lett. 2013, 103 (16): 162903-162906.

[126] L. Pintilie, K. Boldyreva, M. Alexe, D. Hesse. Coexistence of ferroelectricity and antiferroelectricity in epitaxial $PbZrO_3$ films with different orientations [J]. J Appl Phys. 2008, 103 (2): 475-480.

[127] S. Gariglio, N. Stucki, J.-M. Triscone, G. Triscone. Strain relaxation and critical temperature in epitaxial ferroelectric $Pb(Zr_{0.20}Ti_{0.80})O_3$ thin films [J]. Appl Phys Lett. 2007, 90 (20): 152904-152907.

[128] C. Beekman, W. Siemons, T. Z. Ward, M. Chi, J. Howe, M. D. Biegalski, N. Balke, P. Maksymovych, A. K. Farrar, J. B. Romero, P. Gao, X. Q. Pan, D. A. Tenne, H. M. Christen. Phase Transitions, Phase Coexistence, and Piezoelectric Switching Behavior in Highly Strained $BiFeO_3$ Films [J]. Adv Mater. 2013, 25 (39): 5561-5567.

[129] A. K. Tagantsev, K. Vaideeswaran, S. B. Vakhrushev, A. V. Filimonov, R. G. Burkovsky, A. Shaganov, D. Andronikova, A. I. Rudskoy, A. Q. R. Baron, H. Uchiyama, D. Chernyshov, A. Bosak, Z. Ujma, K. Roleder, A. Majchrowski, J. H. Ko, N. Setter. The origin of antiferroelectricity in $PbZrO_3$ [J]. Nat Commun. 2013, 4: 145-150.

[130] X. H. Hao, J. W. Zhai, X. W. Song, J. C. Yang, and H. P. Ren. Fabrication and Characterization of Sol-Gel Derived (100)-Textured $(Pb_{0.97}La_{0.02})(Zr_{0.95}Ti_{0.05})O_3$ Thin Films [J]. J Am Ceram Soc. 2009, 92 (12): 3081-3083.

[131] M. McMillen, A. M. Douglas, T. M. Correia, P. M. Weaver, M. G. Cain, J. M. Gregg. Increasing recoverable energy storage in electroceramic capacitors using ``dead-layer'' engineering [J]. Appl Phys Lett. 2012, 101 (24): 242909-242904.

[132] W. Yao, D. Yuan. Progress on the Studies of Perovskite Pb-Based Antiferroelectric Energy Storage Materials [J]. Materials China. 2011, 30 (9): 51-55.

[133] I. B. Misirlioglu, L. Pintilie, M. Alexe, D. Hesse. Influence of long-range dipolar interactions on the phase stability and hysteresis shapes of ferroelectric and antiferroelectric multilayers [J]. J Mater Sci. 2009, 44 (19): 5354-5363.

[134] B. M. Xu, P. Moses, N. G. Pal, L. E. Cross. Charge release of lanthanum-doped lead zirconate titanate stannate antiferroelectric thin films [J]. Appl Phys Lett. 1998, 72 (5): 593-595.

[135] X. Hao, Y. Wang, L. Zhang, L. Zhang, S. An. Composition-dependent dielectric and energy-storage properties of (Pb,La)(Zr,Sn,Ti)O_3 antiferroelectric thick films [J]. Appl Phys Lett. 2013, 102 (16): 163903-163904.

[136] X. Chou, M. Guo, Y. Zhang, J. Liu, W. Zhang. Preparation and dielectric properties of highly preferred-(100) orientation (Pb, La)(Zr, Ti)O_3 antiferroelectric thick films by sol-gel processing [J]. J Sol-gel Sci Techn. 2012, 61 (1): 62-68.

[137] J. G. Wu, J. L. Zhu, D. Q. Xiao, J. G. Zhu. Double hysteresis loop in $(Pb_{0.90}La_{0.10})Ti_{0.975}O_3/Pb(Zr_{0.20}Ti_{0.80})O_3$ bilayer thin films [J]. Appl Phys Lett. 2007, 91 (21): 122905-122908.

[138] J. Ge, G. Pan, D. Remiens, Y. Chen, F. Cao, X. Dong, G. Wang. Effect of electrode materials on the scaling behavior of energy density in

$Pb(Zr_{0.96}Ti_{0.03})Nb_{0.01}O_3$ antiferroelectric films [J]. Appl Phys Lett. 2012, 101 (11): 112905-112908.

[139] V. R. Palkar, S. Chattopadhyay, S. C. Purandare, S. G. Lokhre, R. Pinto, M. S. Multani. Oriented single phase $PbZrO_3$ thin films on Si(100) substrate using aqueous sol with rapid thermal annealing [J]. Mater Lett. 1997, 33 (1-2): 1-5.

[140] Y. H. Kim, J. J. Kim. Scaling behavior of an antiferroelectric hysteresis loop [J]. Phys Rev B. 1997, 55 (18): 11933-11936.

[141] J. M. Liu, H. P. Li, C. K. Ong, L. C. Lim. Frequency response and scaling of hysteresis for ferroelectric $Pr(Zr_{0.52}Ti_{0.48})O_3$ thin films deposited by laser ablation [J]. J Appl Phys. 1999, 86 (9): 5198-5202.

[142] M. H. Lente, A. Picinin, J. P. Rino, J. A. Eiras. 90 degrees domain wall relaxation and frequency dependence of the coercive field in the ferroelectric switching process [J]. J Appl Phys. 2004, 95 (5): 2646-2653.

[143] Y. W. So, D. J. Kim, T. W. Noh, J. G. Yoon, T. K. Song. Polarization switching kinetics of epitaxial $Pb(Zr_{0.4}Ti_{0.6})O_3$ thin films [J]. Appl Phys Lett. 2005, 86 (9): 142908-142911.

[144] R. Yimnirun, Y. Laosiritaworn, S. Wongsaenmai, S. Ananta. Scaling behavior of dynamic hysteresis in soft lead zirconate titanate bulk ceramics [J]. Appl Phys Lett. 2006, 89 (16): 132904-132906.

[145] X. F. Chen, X. L. Dong, Z. Y. Zhou, J. X. Wang, F. Cao, G. S. Wang, H. L. Zhang. Dynamic hysteresis and scaling behavior for $Pb(Zr,Ti)O_3$ ceramics [J]. J Appl Phys. 2014, 115 (12): 541-546

List of Publication

1. **Jun Ge**, Gang Pan, Denis Remiens, Ying Chen, Fei Cao, Xianlin Dong, Genshui Wang. Effect of electrode materials on the scaling behavior of energy density in $Pb(Zr_{0.96}Ti_{0.03})Nb_{0.01}O_3$ antiferroelectric films. **Appl. Phys. Lett.**, 2012, 101, 112905

2. **Jun Ge**, Xianlin Dong, Ying Chen, Fei Cao, and Genshui Wang. Enhanced polarization switching and energy storage properties of $Pb_{0.97}La_{0.02}(Zr_{0.95}Ti_{0.05})O_3$ antiferroelectric thin films with $LaNiO_3$ oxide top electrodes. **Appl. Phys. Lett.**, 2013, 102, 142905

3. **Jun Ge**, Denis Remiens, Jean Costecalde, Ying Chen, Xianlin Dong, Genshui Wang. Effect of residual stress on energy storage property in $PbZrO_3$ antiferroelectric thin films with different orientations. **Appl. Phys. Lett.**, 2013, 103, 162903

4. **Jun Ge**, Denis Remiens, Xianlin Dong, Ying Chen, Jean Costecalde, Feng Gao, Fei Cao, Genshui Wang. Enhancement of energy storage in epitaxial $PbZrO_3$ antiferroelectric films using strain engineering. **Appl. Phys. Lett.**, 2014, 105, 112908

5. **Jun Ge**, Ying Chen, Xianlin Dong, Denis Remiens, Xin Guo, Fei Cao, Genshui Wang, Dynamic hysteresis and scaling behavior in epitaxial antiferroelectric film. **Thin Solid Films**, 2015, 584, 108-111

6. Lirong Song, Ying Chen, Genshui Wang, Lihui Yang, **Jun Ge**, Xianlin Dong, Pinghua Xiang, Yuanyuan Zhang, and Xiaodong Tang, Fabrication and dielectric properties of $Ba_{0.63}Sr_{0.37}TiO_3$ thin films on SiC substrates. **J. Am. Ceram. Soc.**, 2014, 97(10): 3048-3051

List of Conference

1. The 7th International Conference on Technological Advances of Thin films and Surface Coatings, Chongqing, 15-18 July, 2014, Oral presentation.

2. The 2015 E-MRS Spring Meeting, Lille, 11-15 May, 2015, Oral presentation.